Charge and Spin Transport in Parallel-Coupled Quantum Dots in Nanowires

Nilsson, Malin

2018

Document Version:
Publisher's PDF, also known as Version of record

Charge and Spin Transport in Parallel-Coupled Quantum Dots in Nanowires

MALIN NILSSON
DIVISION OF SOLID STATE PHYSICS | DEPARTMENT OF PHYSICS | LUND UNIVERSITY

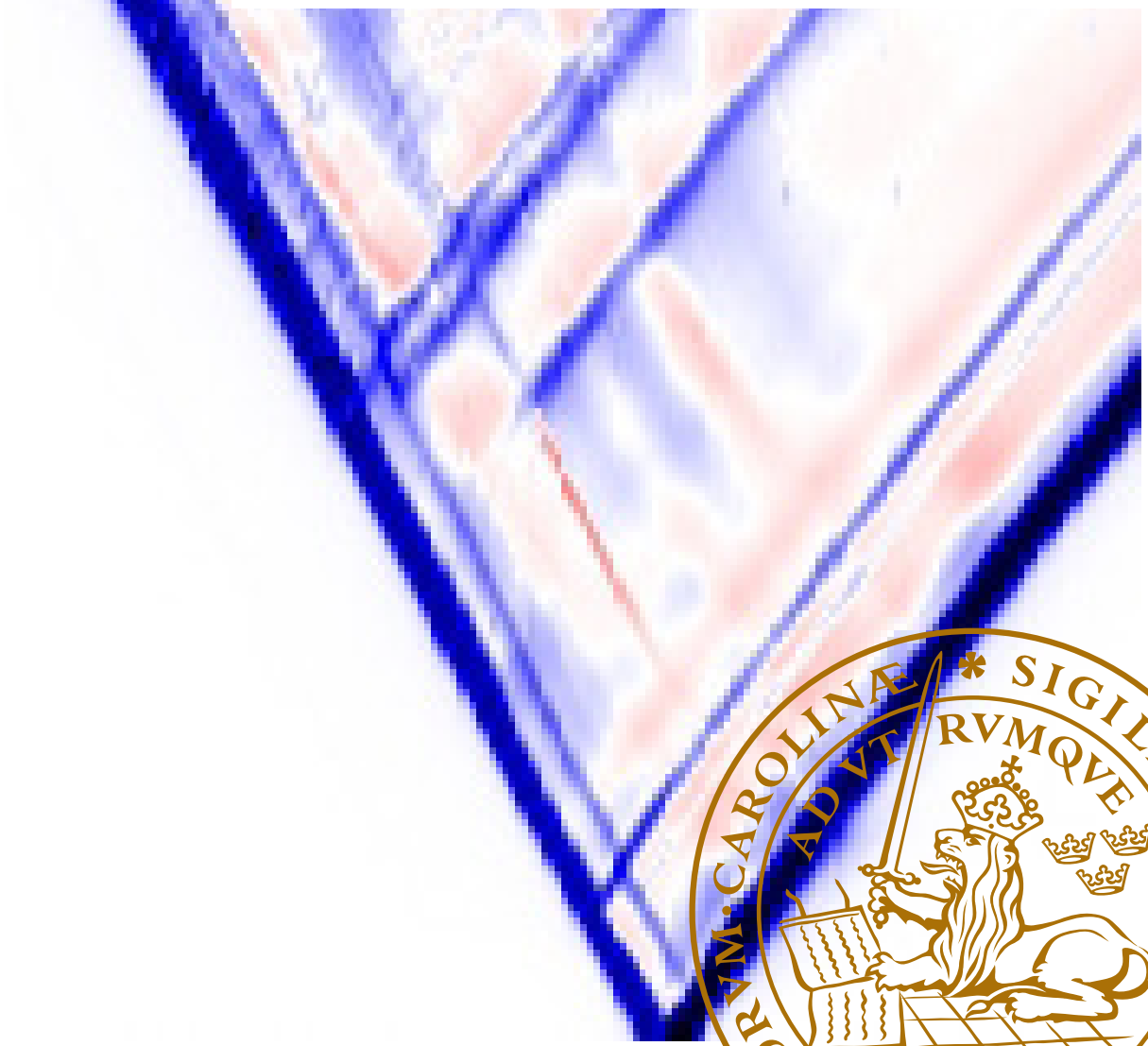

Charge and Spin Transport in Parallel-Coupled Quantum Dots in Nanowires

Malin Nilsson

LUND
UNIVERSITY

Division of Solid State Physics
Department of Physics
Lund University

DOCTORAL DISSERTATION
by due permission of the Faculty of Engineering at Lund University, Sweden.
To be publicly defended on Friday, the 8th of June, 2018, at 09:15 in the
Rydberg Lecture Hall at the Department of Physics, Sölvegatan 14, Lund.

Faculty opponent
Assoc. Prof. Stefano Roddaro
University of Pisa, Italy

Organization:	Document name:
LUND UNIVERSITY Division of Solid State Physics Department of Physics P.O. Box 118, SE-221 00 Lund, Sweden	DOCTORAL DISSERTATION
	Date of issue:
Author: Malin Nilsson	Sponsoring organization:

Title: Charge and Spin Transport in Parallel-Coupled Quantum Dots in Nanowires

Abstract:

This thesis explores crystal-phase engineering of nanowires to fabricate advanced quantum structures for charge and spin transport studies. Quantum dots formed by crystal-phase tuning during epitaxial growth of InAs nanowires were used as a starting point to realize and electrically characterize two different types of parallel-coupled quantum dots; electron-hole quantum dots and electron-electron quantum dots. In the InAs nanowire, two thin segments of wurtzite in an otherwise zinc blende crystal structure acted as tunnel barriers for electron transport and defined the quantum dot in the axial dimension. We estimated the offset in the conduction-band alignment at the wurtzite-zinc blende interface to be ~100 meV. The axial extension of the quantum dot could be tuned to less than 10 nm, which led to a strong quantum confinement and enabled the quantum dot to become fully depleted of electrons.

In few-electron InAs quantum dots, pairs of local side gates and a global back gate were used to reproducibly tune the system from one quantum dot into parallel double quantum dots, for which we can control the populations down to the last electrons. Here, the interdot tunnel coupling of the two first orbitals could be tuned by one order of magnitude, owing to the combination of hard-wall barriers to the source and drain, shallow interdot tunnel barriers, and very high single-particle excitation energies (up to ~30 meV). In addition, the large $|g^*|$-factors (~10) facilitated detailed studies of the magnetic-field dependency of the one- and two-electron states. In particular, we investigated the magnetic field-induced transition between singlet and triplet two-electron ground states. Here, the strong spin-orbit coupling in the system hybridized the single and triplet states. By controlling the interdot tunneling coupling we demonstrated a widely tunable anticrossing of the ground and excited states.

Parallel electron-hole core-shell quantum dots were realized by using the InAs nanowire quantum dot as a template for selective radial growth of GaSb on the zinc blende crystal phase. As a heterostructure in bulk, InAs and GaSb form a broken band-gap alignment with spatially separated electrons and holes. In quantum dots, the overlap of the InAs conduction band and GaSb valence band can be tuned, which is of interest in studies of electron-hole interactions and transport via hybridized states. The electrical measurements of devices in the many-electron/hole regime showed clear evidence of transport via parallel quantum dots in the form of a beating pattern of small and much larger diamonds. We attributed the small-diamond pattern to electron transport in the core and the larger-diamond pattern to hole transport via the shell. From shifts in the conduction lines at the degeneracy point, we extracted an upper estimation of the electron-hole interaction strength of 4.5 meV.

The work presented in this thesis demonstrate the great potential of using atomically precise crystal-phase design of nanowires to access and probe fundamental quantum physics.

Key words: InAs, GaSb, nanowire, quantum dots, artificial molecules, spin-orbit interaction, spintronics, crystal-phase engineering

Classification system and/or index terms (if any):

Supplementary bibliographical information:	Language: English
ISSN and key title:	ISBN: 978-91-7753-701-4
Recipient's notes:	Number of pages: 172 / Price: / Security classification:

Charge and Spin Transport in Parallel-Coupled Quantum Dots in Nanowires

Doctoral thesis

Malin Nilsson

LUND
UNIVERSITY

Division of Solid State Physics
Department of Physics
Lund University

Front cover: Coulomb charge stability diagram recorded along the gate-vector connecting the first two triple points of a parallel-coupled double quantum dot, zoomed-in on the region between the one- and two-electron blockade diamonds. An external magnetic field was applied, aligning the unperturbed S and T_+ states.

Back cover: Coulomb charge stability diagram recorded for a single quantum dot in the many-electron regime over a gate potential interval of 1 V.

Division of Solid State Physics
Department of Physics
Lund University
P.O. Box 118
SE-221 00 Lund
Sweden

ISBN 978-91-7753-701-4 (print)
ISBN 978-91-7753-702-1 (electronic)

Printed in Lund, Sweden, by Media-Tryck, Lund University
May 2018

Contents

Abstract

This thesis explores crystal-phase engineering of nanowires to fabricate advanced quantum structures for charge and spin transport studies. Quantum dots formed by crystal-phase tuning during epitaxial growth of InAs nanowires were used as a starting point to realize and electrically characterize two different types of parallel-coupled quantum dots; electron-hole quantum dots and electron-electron quantum dots. In the InAs nanowire, two thin segments of wurtzite in an otherwise zinc blende crystal structure acted as tunnel barriers for electron transport and defined the quantum dot in the axial dimension. We estimated the offset in the conduction-band alignment at the wurtzite-zinc blende interface to be $\sim$100 meV. The axial extension of the quantum dot could be tuned to less than 10 nm, which led to a strong quantum confinement and enabled the quantum dot to become fully depleted of electrons.

In few-electron InAs quantum dots, pairs of local side gates and a global back gate were used to reproducibly tune the system from one quantum dot into parallel double quantum dots, for which we can control the populations down to the last electrons. Here, the interdot tunnel coupling of the two first orbitals could be tuned by one order of magnitude, owing to the combination of hard-wall barriers to the source and drain, shallow interdot tunnel barriers, and very high single-particle excitation energies (up to $\sim$ 30 meV). In addition, the large $|g^*|$-factors ($\sim$10) facilitated detailed studies of the magnetic-field dependency of the one- and two-electron states. In particular, we investigated the magnetic field-induced transition between singlet and triplet two-electron ground states. Here, the strong spin-orbit coupling in the system hybridized the single and triplet states. By controlling the interdot tunneling coupling we demonstrated a widely tunable anticrossing of the ground and excited states.

Parallel electron-hole core-shell quantum dots were realized by using the

InAs nanowire quantum dot as a template for selective radial growth of GaSb on the zinc blende crystal phase. As a heterostructure in bulk, InAs and GaSb form a broken band-gap alignment with spatially separated electrons and holes. In quantum dots, the overlap of the InAs conduction band and GaSb valence band can be tuned, which is of interest in studies of electron-hole interactions and transport via hybridized states. The electrical measurements of devices in the many-electron/hole regime showed clear evidence of transport via parallel quantum dots in the form of a beating pattern of small and much larger diamonds. We attributed the small-diamond pattern to electron transport in the core and the larger-diamond pattern to hole transport via the shell. From shifts in the conduction lines at the degeneracy point, we extracted an upper estimation of the electron-hole interaction strength of 4.5 meV.

The work presented in this thesis demonstrate the great potential of using atomically precise crystal-phase design of nanowires to access and probe fundamental quantum physics.

Populärvetenskaplig sammanfattning

Vi är just nu inne i den Andra kvantrevolutionen! Ett av målen är snabbare datorer, så kallade kvantdatorer, som kan lösa vissa typer av problem som vanliga "klassiska" datorer inte kan. Det som har möjliggjort denna revolution är en djupare förståelse av kvantmekaniska fenomen som superposition av kvanttillstånd, växelverkan mellan elektroner och ljus, supraledande material och exotiska materialfaser.

Den Första kvantrevolutionen startade runt förra sekelskiftet och innebar en fundamentalt ny idé om att små partiklar, som elektroner, kan bete sig som både vågor och som partiklar. Även ljus, som klassiskt setts som vågor, har dessa dubbla egenskaper. Fenomenet kallas våg-partikel-dualiteten och är en av grundpelarna i den kraftfulla kvantmekaniska teorin som används för att beskriva egenskaper hos materia och som ligger bakom att vi förstår det Periodiska systemet, kemiska bindningar och hur elektroner rör sig i så kallade halvledarmaterial. Den teoretiska förståelsen för fundamentala fysikaliska koncept startade en explosionsartad utveckling av elektriska komponenter, som till exempel transistorn. Transistorn är en förutsättning för dagens informationssamhälle och mycket av den elektronik omkring oss såsom datorer och smarta telefoner. Den första transistorn var stor som en näve och uppfanns i slutet på 40-talet, idag innehåller en mobiltelefon miljarder transistorer! Också teknologi som vi idag tar för givet, såsom solceller och lasern, föddes ur den första kvantrevolutionen.

Det är uppenbart att förutsättningen för vidare kvantteknologisk utveckling är ökad förståelse för kvantfenomen på ett fundamentalt plan. På så sätt kan komponenter designas för att utnyttja kvantmekaniska effekter och nå nya teknologiska tillämpningar. Även om fysiken som kvantmekanikens lagar beskriver kan få makroskopiska uttryck, såsom ledningsförmågan i olika material, till exempel supraledning, är det i princip på nära-atomnivå vi måste designa material för att de ska få önskade kvantmekaniska egenskaper.

Denna avhandling utforskar hur vi kan designa och bygga komponenter på atomnivå för att kontrollera och studera fundamentala kvantmekaniska egenskaper. Här nedan följer beskrivningar av några koncept som är speciellt viktiga i detta arbete.

Halvledare. Fasta material delas in i tre olika grupper (metaller, halvledare, isolatorer) baserat på deras förmåga att leda elektrisk ström (flöde av elektroner). Till skillnad från metaller, som leder ström mycket bra och isolatorer, som inte leder alls, kan ledningsförmågan hos halvledare styras. Detta utnyttjas i transistorn där strömmen snabbt kan slås av och på. Elektroner i halvledare har även tydligare och ibland unika kvantmekaniska beteenden. I avhandlingen används halvledarmaterial för att kunna styra strömmar så små som enskilda elektroner!

Artificiella atomer & molekyler. Ett av de mest grundläggande fenomenen som avhandlingen bygger på är kvantisering av elektroners energi. I arbetet studeras mycket små, så kallade nolldimensionella (0D), strukturer av halvledarmaterial (1-100 nm). Dessa små strukturer kallas för kvantprickar eller artificiella atomer eftersom elektronerna i dessa strukturer inte kan röra sig fritt som i tredimensionella strukturer, utan bara kan ha vissa specifika energier, liknade energinivåer för elektroner i atomer. Detta kallas kvantisering av energi och är en kvantmekanisk effekt som blir dominant i halvledarstrukturer som är mindre än 10-tals nm. Kopplas två artificiella atomer på rad, skapas en artificiell molekyl, som även den har egenskaper liknade de för riktiga molekyler. Artificiella atomer och molekyler kan användas som grund för att bygga *qubits*, som är komponenterna som utför beräkningar i kvantdatorer istället för transistorn i den klassiska datorn. I avhandlingen utvecklas en ny metod för att skapa artificiella atomer och molekyler, och förutspådda kvantmekaniska effekter studeras i experiment med en aldrig

tidigare skådad upplösning.

Nanotrådar. För att kunna se kvanteffekter måste vi studera strukturer som har dimensioner motsvarande ett hundratal atomer. För att skapa och designa så små strukturer måste vi ha en mycket hög precision, vi måste i princip ha kontroll över varje enskild atom.

Det finns metoder för att skapa strukturer med hög precision, atomlager för atomlager. Nanotrådar är, som namnet antyder, nanometertunna endimensionella (1D) trådar, som kan ”växas” genom att placera en skiva med små guldpartiklar i en särskild reaktor och tillföra det ämne som nanotråden ska bestå av i form av gasmolekyler. Under rätt temperatur och koncentration av tillfört ämne kommer en nanotråd ta form under guldpartikeln, atomlager för atomlager. Nanotrådar bestående av olika ämnen kan skapas genom att byta det tillförda ämnet. Även skal kan ”växas” på nanotråden genom att ändra bland annat temperaturen i reaktorn.

I avhandlingen används två olika kristallstrukturer av samma halvledarmaterial för att med hög precision forma kvantprickar. Kristallstrukturen talar om hur atomerna sitter i förhållande till varandra, vilket påverkar hur elektroner rör sig i materialet. Det är endast i nanotrådar som olika kristallstrukturer kan kombineras. Eftersom nanotrådar är så tunna upplever elektroner dem som en endimensionell struktur, och med det menas att elektronerna bara kan röra sig i en riktning. Genom att kombinera två olika kristallstrukturer kan elektronernas rörelse begränsas och en nolldimensionell kvantprick kan skapas.

Nanokomponenter. För att kunna kontrollera och studera elektronernas beteende i kvantprickarna måste nanotrådarna kopplas till elektrisk utrustning. Genom en rad högteknologiska processteg skapas små metallkontakter till nanotrådarna, och dessa kontakter kopplas till mätutrustningen.

Mätningar vid låga temperaturer. Elektriska och magnetiska fält används för att styra elektronerna i nanokomponenterna. Effekterna vi vill mäta är väldigt små och därför måste mätningarna ske vid mycket låga temperaturer, ungefär 0.1 grader ifrån absoluta nollpunkten. Det finns en energi som all materia har och som är förknippad med den omgivande temperaturen; denna kallas termisk energi. Om den termiska energin inte är mycket mindre än energiskillnaden på de kvantmekaniska effekterna som vi vill mäta suddas effekterna ut.

List of papers

This thesis is based on the work presented in the following papers, referred to as Papers I–IV in the text.

I. Single-electron transport in InAs nanowire quantum dots formed by crystal phase engineering

Malin Nilsson, Luna Namazi, Sebastian Lehmann, Martin Leijnse, Kimberly A. Dick, and Claes Thelander

Physical Review B, **93**, 195422 (2016)

I fabricated the devices from as-grown nanowires, performed the electrical measurements, data analysis and analytical calculations. I took part in the SEM imaging and extracted QD dimensions. I was actively involved in writing the paper and compiled the figures, except for Figure 4.

II. Electron-hole transport in InAs-GaSb core-shell quantum dots with self-assembled tunnel contacts

Malin Nilsson, Luna Namazi, Sebastian Lehmann, Martin Leijnse, Kimberly A. Dick, and Claes Thelander

Physical Review B, **94**, 115313 (2016)

I provided input to the design of the QD structures. I fabricated devices from as-grown nanowires, performed most of the electrical measurements and data analysis. I took part in the SEM imaging and I extracted QD

dimensions. I was actively involved in writing the paper and compiled the figures, except for Figure 2.

III. Parallel-Coupled Quantum Dots in InAs Nanowires

Malin Nilsson, I-Ju Chen, Sebastian Lehmann, Vendula Maulerova, Kimberly A. Dick, and Claes Thelander

Nano Letters, **17**, 7847–7852 (2017)

I was responsible for the development of the QD structures; I designed and fabricated the pre-growth substrate. I fabricated devices from as-grown nanowires, operated the dilution fridge setup and took part in the electrical measurements and data analysis. I contributed to the writing of the paper, compiled the figures and coordinated the final steps of the paper preparation.

IV. Tuning the two-electron hybridization and spin states in parallel-coupled InAs quantum dots

Malin Nilsson, Florinda Viñas Boström, Sebastian Lehmann, Kimberly A. Dick, Martin Leijnse, and Claes Thelander

Submitted, arXiv:1803.00326 (2018)

I led the project and was responsible for the development of the QD structures; designed and fabricated the pre-growth substrate. I fabricated devices from as-grown nanowires, operated the dilution fridge setup, performed most of the electrical measurements and the data analysis. I contributed to the development of the modeling work, and had the main role in writing the paper.

The following papers are relevant, but are not included in the thesis.

V. Selective GaSb radial growth on crystal phase engineered InAs nanowires

Luna Namazi, Malin Nilsson, Sebastian Lehmann, Claes Thelander, and Kimberly A. Dick

Nanoscale, **7**, 10472-10481 (2015)

VI. Sn-Seeded GaAs Nanowires as Self-Assembled Radial p-n Junctions

Rong Sun, Daniel Jacobsson, I-Ju Chen, Malin Nilsson, Claes Thelander, Sebastian Lehmann, and Kimberly. A. Dick

Nano Letters, **15**, 3757-3762 (2015)

VII. Conduction Band Offset and Polarization Effects in InAs Nanowire Polytype Junctions

I-Ju Chen, Sebastian Lehmann, Malin Nilsson, Pyry Kivisaari, Heiner Linke, Kimberly A. Dick, and Claes Thelander

Nano Letters, **17**, 902-908 (2017)

VIII. Realization of wurtzite GaSb using InAs nanowire templates

Luna Namazi, Louise Gren, Malin Nilsson, Magnus Garbrecht, Claes Thelander, Reza R. Zamani, and Kimberly A. Dick

Advanced Functional Materials, *Accepted* (2018)

Abbreviations

ALD	Atomic layer deposition
AsH_3	Arsine
EBL	Electron beam lithography
ECCI	Electron channeling contrast imaging
ES	Excited state
DQD	Double quantum dot
GaSb	Gallium antimonide
GS	Ground state
InAs	Indium arsenide
MOVPE	Metal organic vapor phase epitaxy
PMMA	Polymethyl methacrylate
QD	Quantum dot
SEM	Scanning electron microscope
SOI	Spin-orbit interaction
TEM	Transmission electron microscope
TMGa	Trimethylgallium
TMIn	Trimethylindium
TMSb	Trimethylantimony
VLS	Vapor-liquid-solid

WZ	Wurtzite
ZB	Zinc blende

Symbols

AB	Antibonding state
B	Bonding state
B	External magnetic field
C_Σ	Sum of the capacitances to the quantum dot
C_D	Drain capacitance
C_G	Gate capacitance
C_S	Source capacitance
ΔE_z	Zeeman energy split
Δ^*_{ST}	Anticrossing-magnitude of $GS(1,1)$ and $ES(1,1)$ at zero detuning of the unperturbed states
$\frac{dI_{SD}}{dV_{SD}}$	Differential conductance
$GS(1,1)$	Two-electron ground state in the presence of SOI
e	Elementary charge (1.60219×10^{-19} C)
E_{Add}	Addition energy
E_C	Charging energy
E_{CB}	Energy of conduction-band edge
E_Δ	Single-particle energy
E_F	Fermi level
$ES(1,1)$	Two-electron first excited state in the presence of SOI

E_{VB}	Energy of valence-band edge
E_z	Zeeman energy
G	Conductance
g	g-factor
g^*	Effective g-factor
h	Planck's constant (6.62607×10^{-34} m^2kg/s)
I_{SD}, I_d	Drain current
J	Singlet/triplet energy separation
k	Boltzmann constant (1.38065×10^{-23} J/K)
$\lambda_{electron}$	Electron de Broglie wavelength
μ_B	Bohr magneton (9.27401×10^{-24} J/T)
R	Nanowire radius
σ	Conductivity
S	Spin singlet state
T (T_+, T_0, T_-)	Spin triplet states
T	Temperature
t	Interdot tunnel coupling
V_G, V_g, V_{BG}	Back-gate voltage
V_L, V_R	Side-gate voltage
V_{SD}, V_d	Drain voltage

Chapter 1

Introduction

The quantum era started with the development of the quantum theory around the beginning of the 20th century. The quantum theory gave insights into the interaction of atoms and the motion of electrons in solid materials such as semiconductors, and resulted in the birth of technologies such as the LASER and the transistor. These technologies are building blocks in the information technology-based society we are living in today. In a similar manner, further understanding of entangled states and the possibility to manipulate individual quantum systems are today driving the development of quantum information technology [1]. Here, the information is carried by quantum states as opposed to the classical 1 and 0. One of the most mature technologies when it comes to quantum computing is using superconducting devices to realize the information-carrying units, the so-called qubits [2, 3]. However, electron-spin based qubits have also been extensively studied [4–8]. And recently, topological systems, which are intrinsically immune to local noise, have been explored as candidates for quantum computation platforms [9].

So-called quantum dots are an example of a quantum system that has been of strong interest for quantum information technologies for many years. A key feature of quantum dots is their quasi-zero dimensional structure, where the electrons are spatially confined in all directions, resulting in a quantization of the energy spectrum [10]. This means that the electrons cannot move freely, but are bound to specific discrete energy states. Furthermore, the electrical and optical properties can be tailored by tuning the size and material of the system. Quantum dots are widely studied and are today already employed

in for example opto-electronics to improve light sources such as LEDs and LASERs [11] and to realize true RGB pixels in displays [12]. In electronics, single electron transistors [13], realized using quantum dots, have been studied for decades. And in medicine, quantum dots are utilized to obtain tunable dye [14]. In addition, since single spins can be isolated and manipulated [15] in quantum dots, they are also a platform for studies of fundamental quantum physics [16]. Due to the control of the spin dynamics, single quantum dots, or multiple coupled quantum dots, are employed to realize spin-based qubits for quantum computing [4, 6, 8, 17].

Let us take a step back and address the origin of the quantization of the energy states in quantum dots. In bulk crystalline structures, such as metals or semiconductors, the so-called valence electrons (the electrons that are more weakly bound to the nucleus), can in the effective mass approximation be treated as freely moving electrons, similar to electrons in vacuum. However, interactions with the periodic potential of the atomic lattice are in this approximation parametrized by the "effective" electron mass, which is used instead of the free electron mass. This "free" electron model results in a continuum of states in the electron-energy spectrum. If the spatial extent of the structure is decreased in one direction, to the order of the (de Broglie) wavelength ($\lambda_{electron}$) associated with the electrons in the material (typically $\sim$ nm in semiconductors), the electrons will be confined in that particular dimension, see Figure 1.1. This confinement quantizes the electron motion, which leads to a modification of the energy spectrum. If the electrons are

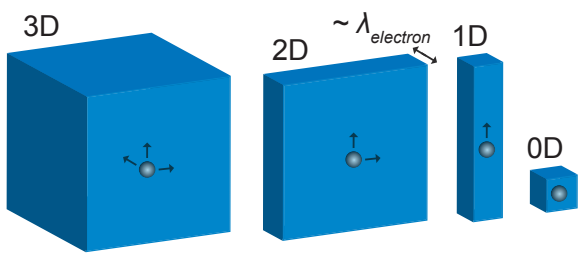

Figure 1.1: The motion of the valence electrons (indicated by the arrows) in a semiconductor or a metal is limited if the dimension of the material is on the order of the electron wavelength ($\lambda_{electron}$). In a zero-dimensional structure, the electrons are confined in all spatial directions, resulting in quantized energy states.

confined in all three dimensions, the energy spectrum will be quantized and electrons are only allowed to occupy discrete energy levels. The quantized states of quantum dots resemble those of atoms, where valence electrons are electrostatically confined by the positive nucleus charge. Therefore, quantum dots are sometimes referred to as artificial atoms. However, since the distance between the discrete energy levels scales as one over the length square of the system, this spacing is on the order of meV in quantum dots as opposed to eV in atoms.

The quantum-dot material can be used as a design parameter. For instance, the quantum confinement effects are more pronounced in semiconductors than in metals, owing to the longer electron wavelength in semiconductors. Furthermore, electrons in semiconductor compounds composed of heavier atoms, such as InAs and InSb, have lower effective masses and therefore exhibit stronger quantum confinement effects than for instance GaAs. In addition, these heavier-atom compounds exhibit a pronounced spin-orbit interaction (SOI), which means that the orbital motion of electrons is coupled to the electron spin. This enables manipulations of spin states by electric fields, which is used for manipulation spin-qubits. A strong SOI is also a key ingredient in the pursuit of realizing Majorana-based quantum computing [9].

The quasi-zero-dimensionality of quantum dots can be obtained by either the intrinsic dimensions of the material or by electrostatic gating. Typically, a combination of the two is used to achieve the confinement. A more extensive description of different approaches to form quantum dots is presented in Section 2.1. Nanowires, which are the focus of this thesis, are excellent structures in which to form quantum dots. In a nanowire, which is a quasi-one dimensional structure (diameters of 10-100 nm), the electrons are confined in the radial direction and are only free to move in the longitudinal direction. Here, quantum dots can be formed by local electrostatic gating or by imposing two

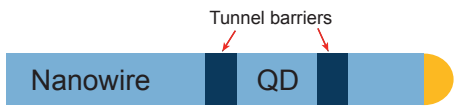

Figure 1.2: A quantum dot in a nanowire defined by two thin segments (dark blue) of a different semiconductor compound (heterostructure) or crystal phase (homostructure).

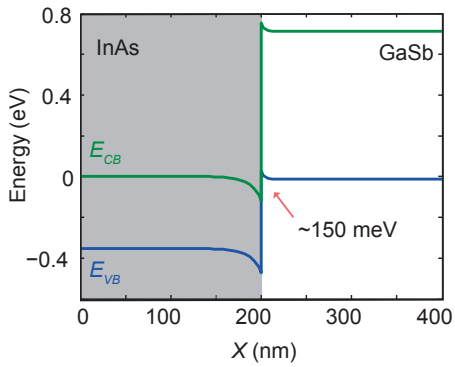

Figure 1.3: Energy band diagram of the InAs-GaSb bulk heterostructure. Here, the InAs conduction band overlaps with the GaSb valence band by approximately 150 meV. E_{CB} and E_{VB} are the conduction band and valence band edge, respectively.

closely spaced segments of a larger bandgap material [18]. The small diameter of the nanowire relaxes the constraint of lattice matching, allowing for a large variety of material combinations, many of which are not possible in two or three dimensions. In addition, a unique feature of nanowires is that many of the III-V semiconductor compounds, that only exist in the zinc blende crystal phase in bulk, can be tuned to exhibit both zinc blende and wurtzite crystal phases depending on the growth conditions [19, 20]. In InAs nanowires, a quantum dot can be formed between two thin segments of wurtzite in an otherwise zinc blende nanowire, as demonstrated in Paper I.

As mentioned above, tunnel-coupled quantum dots, which is the foundation of spin-based qubits, but also charge-qubits [21], can be realized in such systems. Furthermore, two tunnel-coupled quantum dots exhibit molecular properties, such as bonding and anti-bonding orbitals, and are therefore called artificial molecules. Such artificial molecules are model systems for studying spin-spin interactions and dynamics. In Paper III, we demonstrate a novel approach to form parallel-coupled quantum dots using crystal phase-engineered InAs nanowires. These parallel-coupled quantum dots exhibit strongly tunable and extremely well-resolved transport properties of the first electron spin states (Paper IV). We predicted this system to be ideal for fundamental studies of many-body correlated transport, such as spin- Kondo effect [22] and Cooper-pair splitting [23, 24].

Due to significant advances within the field of material science it is now

possible to define parallel-coupled electron and hole quantum dots by epitaxial growth of two different materials such as InAs and GaSb in a core-shell configuration. As a heterostructure, InAs and GaSb form the exotic type-II broken gap band alignment, where the conduction band in InAs and valence band in GaSb overlap, see Figure 1.3. This overlap results in spatially separated electrons and holes, which opens possibilities for studies of electron-hole interactions in quantum dot systems [25]. However, the electrical properties of the parallel-coupled electron and hole quantum dots are highly sensitive to the geometrical parameters such as radius and shell thickness. Employing crystal phase-defined quantum dots in InAs nanowires as a template for selective radial growth of GaSb [26, 27] leads to a highly tunable system. The demonstration of the InAs/GaSb core-shell quantum dot in Paper II is a first step towards the realization of more complex three-dimensional core-shell nanowire designs with close-to-atomic precision.

This thesis is organized as follows:

Chapter 2 covers the design and fabrication of the different nanowire devices. In particular, the crystal phase engineering in InAs nanowires and its role in the quantum dot design are discussed. This chapter partly serves as an introduction and extension to Paper I.

Chapter 3 provides an introduction to the transport physics of the single quantum dot. Examples from both the many- and few-electron regimes in the crystal phase-defined quantum dots are given. Also, both first- and higher-order transport processes are addressed as well as magnetic field-dependent transport. This chapter serves as an introduction to Paper I with an extended discussion.

Chapter 4 introduces the transport of double quantum dots, with focus on the parallel-coupled case and the implication of coherent tunnel coupling of the two dots. The focus is on the zero-one-two electron transitions and the magnetic field evolution of these states. Also, the formation and tuning of the parallel-coupled quantum dots in the crystal phase-defined single quantum dots are explored. This chapter is an introduction to and an expansion of the discussion in Paper III and IV.

Chapter 5 begins with an introduction of the special features of the InAs-GaSb heterostructure, covering the two- one- and zero-dimensional devices. Furthermore, a more detailed description of the development and electrical

characterization of the parallel-coupled electron and hole quantum dots in InAs/GaSb core-shell nanowires is presented. This chapter serves as a complement to Paper II.

Chapter 2

The nanowire device - design and fabrication

This chapter gives a brief introduction to different methods for forming quantum dots for transport measurements, and particularly discusses crystal phase-defined nanowire quantum dots; the structure that constitutes the corner stone of this thesis. In addition to addressing the nanowire material, the growth process and the device design, the processing involved in sample preparation prior to nanowire growth and for metal contacting of nanowires is discussed.

2.1 Forming quantum dots for transport measurements - An overview

Single quantum dots can be fabricated by different means. One of the most widely employed methods to obtain the zero-dimensionality is to start from a two-dimensional electron gas and create the additional confinement by electrostatic top-gating [28, 29]. Here, the two-dimensional gas can be formed by epitaxially grown semiconductor heretostructures, typically AlGaAs/GaAs [30] or graphene [31]. A great advantage of this method is that the growth process of the semiconductor layers and the lithography processing of metal contacts are mature and highly controlled technologies favorable for parallel and automatized device processing. In addition, a combination of gating and top-down etching can be used to obtain a hybrid quantum dot device similar

to the type studied in this thesis [32].

A second method is to use a one-dimensional structure as a starting point, such as a carbon nanotube or a semiconductor nanowire, and impose additional confinement by Schottky barriers at the source and drain contacts, electrostatic gating, or in the case of nanowires, by switching the semiconductor compound during the epitaxial growth. One advantage of starting from a one-dimensional material is the built-in leads to the quantum dot; however, fabricating metal contacts to lateral carbon nanotubes or nanowires is a semi-automatic process with limited reproducibility due to the sensitive electronic properties of the one-dimensional structure. Quantum dots formed in nanowires are discussed in more detail in Section 2.1.1.

A third method is to directly obtain the confinement in all three dimensions by reducing the physical extension of the system using colloidal particles [33], epitaxially grown pyramid-shaped semiconductor crystals by means of the so-called Stranski–Krastanow growth mode [34, 35], or even single atoms [36]. One advantage with colloidal particles and pyramids is that they are created by self-assembly, and do not necessitate advanced processing. However, to explore electrical properties the quantum dots need to be connected to electrodes, and the contact alignment process can be challenging in this case.

2.1.1 Forming quantum dots in nanowires

Nanowires have a quasi-one-dimensional geometry where electron transport is limited to the axial direction. This built-in radial confinement makes nanowires excellent starting points for fabricating quantum dots. Here, quantum dots can be realized by imposing two closely spaced tunnel barriers in the axial direction. The electronic properties of such devices have been extensively studied for more than one decade [18].

There are different methods for forming quantum dots in nanowires. The first reported quantum dots in nanowires were defined by the tunnel barriers formed at the source and drain contacts on InP wires [37]. A second approach to define quantum dots in nanowires, using InAs-InP heterostructures, was reported shortly after [38]. Tunnel barriers can also be induced by electrostatic gating of nanowires [39], or by modulation doping [40, 41].

The concept behind heterostructure-defined electron quantum dots is to insert two closely spaced, narrow segments of a second material to form an

offset in the conduction-band edge (E_{CB}) alignment at the heterostructure interface, as illustrated in Figure 2.1. These segments will act as tunnel barriers; the electrical properties of the quantum dot depend on the geometry of the barriers and their separation. The barrier-energy height (offset) is a material property, dependent on the material combination used, whereas the barrier length is determined during the nanowire growth. One unique feature of the nanowire is that the small diameter relaxes the constraint of lattice matching at the interface of the heterostructure [42, 43], which reduces the limitation on possible material combinations compared with two- and three dimensional structures. Furthermore, utilizing heterostructures to form quantum dots offers more control over the quantum dot dimensions as opposed to relying on the barriers formed at the contact interfaces, since the heterostructure barriers can be designed with close to atomic precision. One additional advantage of the heterostructure barriers, with an approximately hard-wall potential profile in the axial direction of the nanowire, is that the system is less sensitive to electrostatic fluctuations compared with the (harmonic) potential profile obtained by electrostatic gating.

Similar to heterostructure-defined quantum dots, different crystal phases of a single semiconductor compound can be used to form quantum dots in nanowires [27, 44–46]. Such structures are sometimes referred to as homostructures and are unique to nanowires. Crystal phase-defined quantum dots in InAs nanowires represent the foundation of the work presented in this thesis, and will be discussed in more detail in Section 2.2.

2.2 Crystal phase-defined quantum dots in InAs nanowires

The small nanowire diameter allows for epitaxial growth of both wurtzite and zinc blende crystal phases [19, 20, 47], whereas most two- and three-dimensional materials exist in the zinc blende crystal phase only. However, typical nanowires exhibit a mixture of wurtzite and zinc blende. Since the crystal phase has a large impact on transport properties [48, 49], great efforts have been made to obtain single crystal phase nanowires. Due to considerable advances in the science of nanowire growth, it is possible to controllably switch between zinc blende and wurtzite with close-to-atomic precision during the

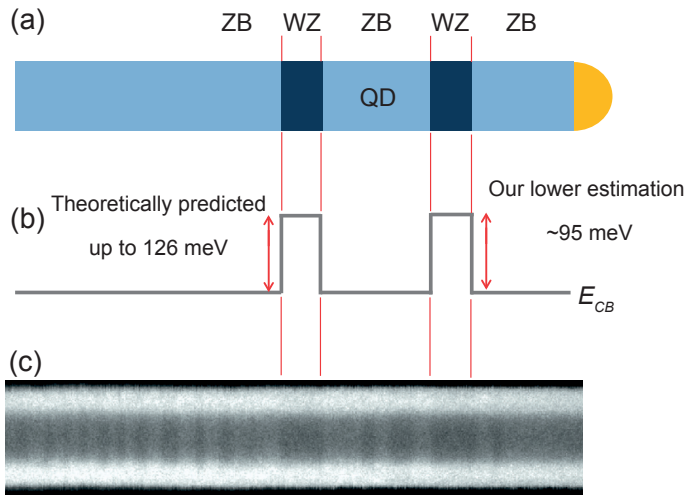

Figure 2.1: (a) Schematic illustration of a quantum dot defined by wurtzite segments in an otherwise zinc blende InAs nanowire. (b) Sketched conduction-band (E_{CB}) alignment of the corresponding system, where the wurtzite segments are assumed to form square potential barriers in the conduction band. (c) SEM image of a crystal phase-defined quantum dot; using information from TEM images on the structural composition of typical nanowires from the same growth substrate, the wurtzite segments can be distinguished in the contrast profile, see Section 2.6.

growth process [20, 47, 50]. More details on the zinc blende and wurtzite crystal phases are given in Section 2.4.

In the case of InAs, it has been theoretically predicted that wurtzite has a larger bandgap than zinc blende [51], with a positive conduction-band edge offset of up to 126 meV [52] at the crystal phase interface. Figure 2.1(a) shows an illustration of a quantum dot defined by wurtzite segments in a zinc blende InAs nanowire. Here, a simplified picture is used where the wurtzite segments were assumed to form square potential barriers in the conduction-band edge alignment, see Figure 2.1(b). In the SEM image in panel (c), the wurtzite segments as well as twinned segments in the zinc blende crystal phase are visible using electron channeling contrast imaging (ECCI) [53, 54]. This technique is discussed in more detail in Section 2.6. Signatures of single-electron transport in crystal phase-defined quantum dots in InAs was first experimentally demonstrated by Dick *et al.* [44].

From transport measurements in Paper I, a lower boundary estimate of the effective barrier height of ∼95 meV was obtained, and it was in line with the estimated value of ∼135 meV obtained from thermionic emission measurements on longer wurtzite segments in zinc blende InAs nanowires performed by Chen *et al.* [55]. Both these estimates were from measurements on nanowires with native oxide. In contrast, results from scanning tunneling spectroscopy of hydrogen-cleaned InAs nanowires revealed no detectable offset in the conduction band, however, the lack of offset was attributed to the intrinsic *n*-type characteristic of InAs masking the fundamental offset [56, 57].

2.3 Nanowire growth process

The nanowires studied in this work were grown by a vapor-liquid-solid (VLS) process using metal organic vapor phase epitaxy (MOVPE). The growth process was catalyzed either by aerosol [Paper I and II], or electron beam lithography (EBL) defined arrays [Paper III and IV] of Au seed particles deposited on $(\bar{1}\bar{1}\bar{1})$-oriented InAs substrates. For growth of InAs, trimethylindium (TMIn) and arsine (AsH_3) were used as group-III and group-V precursors, and for GaSb trimethylgallium (TMGa) and trimethylantimony (TMSb) were employed.

Now follows a brief description of the III-V semiconductor nanowire growth process, for details, see [58]. Once the substrate with the gold catalyst particles was placed in the growth chamber, the sample was annealed during a couple of minutes under an elevated temperature of 550 °C to desorb native oxides and other contaminants from the surface of the substrate. Since the group-V material has a higher vapor pressure, an over-pressure of a mixture of H_2 and the group-V precursor was maintained during the annealing to prevent decomposition of the substrate due to degassing of the group-V material. As a consequence of the elevated temperature, the gold particles melted and formed liquid droplets that alloyed with the substrate. After annealing, the temperature was set to a constant value used throughout the growth. In this work, a higher growth temperature (∼460 °C) was used compared to [44] (380 °C), which resulted in a reduction of carbon incorporation during growth. In Ref. [44], carbon acted as an *n*-type dopant and made the system difficult to deplete of electrons. The next step was to introduce the group-III precursor.

The vapor-phase precursors decomposed when they came into contact with the substrate, which resulted in physisorbed atomic-species of group-III and V on the substrate. The atomic-species diffused on the substrate (and the nanowire surface), and dissolved in the gold droplet. Once the droplet reached so-called supersaturation of the group III-material, local nucleation of the semiconductor III-V crystal appeared at the substrate-droplet interface. The epitaxial growth of the nanowire continues as long as new precursor material is provided. The growth rate depends mainly on the size and the areal density of the droplets, the precursor flow rate and the temperature. However, other factors such as the surface of the substrate and crystal phase of the nanowire also affect the growth rate.

Heterostructures are obtained by changing the precursor materials. The nucleation at the nanowire/particle interface is an axial growth process, but radial growth can be promoted (or suppressed) by tuning the growth parameters. It is also possible to use the crystal phase as a template for radial growth [26], to obtain advanced three-dimensional core-shell structures. This is discussed further in Chapter 5.

The electrical properties of a quantum dot are to a great extent governed by the geometry of the structure. The axial length and diameter of the quantum dot set the quantization energy of the bound states and the axial length of the tunnel barrier segments affects the tunnel rate, and thus also the extent of the localization of the states in the quantum dot. It is of utmost importance to, during growth, tune parameters such as the diameter, the lengths of different segments and the thickness of the radial shell with high precision. For instance, substantial efforts have been made to decrease the radial dimension of the InAs nanowire in order to study the effects anticipated in highly quantum-confined core-shell systems, such as tuning the overlap of the core and shell states, see Chapter 5. However, decreasing the diameter without losing the pure crystal phase is challenging, since the crystal phase depends strongly on the diameter [59]. Defects in the crystal phase can result in unwanted electrical properties of the nanowire [48], such as random quantum dot formation [60]. One way to increase the control during growth is to use well-defined arrays of seed particles, as was employed in Paper III and IV. Arrays of seed particles are addressed in Section 2.8.

2.4 Crystal phases - zinc blende and wurtzite

Zinc blende and wurtzite are the two most important crystal phases in III-V semiconductor compounds [61]. The crystal phase describes the stacking sequence of the atomic layers in the axial direction in the nanowire. In the case of wurtzite, also called a hexagonal close-packed (hcp) structure, the bilayers are repeated in an ABAB-type order. In zinc blende, on the other hand, also called a cubic close packed (ccp) structure, the order of the bilayers is ABCABC, as illustrated in Figure 2.2(a).

There are different means to control the crystal phase of a nanowire. For instance, the diameter of the seed particle affects the crystal phase; typically, smaller diameters are prone to form a wurtzite crystal phase, while larger diameters form zinc blende [59]. Controlled crystal phase-tuning during growth was first reported by tuning the temperature [InAs] [47], and the dopant incorporation [InP] [62].

In the work presented in this thesis, the different crystal phases were obtained by modulating the III/V precursor ratio, either by changing the molar

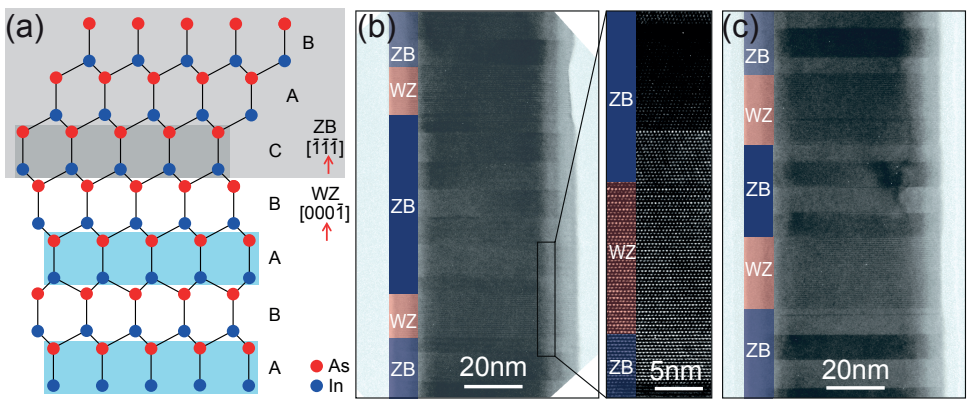

Figure 2.2: (a) Sketched projection of the atomic structure of the wurtzite and zinc blende crystal phases. The bilayer sequence ABAB for wurtzite (ABCABC for zinc blend) is indicated. (b) and (c) Transmission electron microscope (TEM) images of crystal phase-defined quantum dots in InAs nanowires, where the growth time for the quantum dot zinc blende segment was 20 s (b) and 40 s (c), and 5 s for the wurtzite barriers in both cases. The dimensions were (b): wurtzite segment lengths 16 nm/20 nm, and zinc blende quantum dot length 66 nm, (c): wurtzite segment lengths 25 nm, and zinc blende quantum dot length 32 nm.

fraction of the two growth species or only group V. Zinc blende was grown at a higher III/V precursor ratio. Increasing the group V flow to obtain zinc blende has been reported as a general scheme in III-V nanowire growth [20]. Figures 2.2(b) and (c) show transmission electron microscope (TEM) images of nanowires with crystal phase defined-quantum dots, where the axial extension of the quantum dot was modulated by tuning the growth time of the zinc blend quantum dot segment. The striped contrast profile of the zinc blende segments was due to rotational twining which corresponds to a 60° rotation of the atomic layer around the growth axis [61].

2.5 Nanowire device design

Now follows an overview of the nanowire device designs based on two different types on nanowire structures that are explored in this thesis. The first type of nanowire was InAs nanowires where electron quantum dots were defined by wurtzite segments in an otherwise zinc blende crystal phase, see Figures 2.3(a-c). Here, the quantum confinement was tuned by controlling the distance between the wurtzite barriers during epitaxial growth. Paper I goes beyond proof of concept and presents an in-depth study of the effect of wurtzite barriers on single-electron transport in the many-electron regime, where the precise control of the crystal phase during nanowire growth allows tuning of the electrical properties of the quantum-dot devices.

When the quantum-dot size was reduced as illustrated in Figure 2.3(b), the system could be tuned into the few-electron regime and further into full depletion of electrons. In quantum transport measurements, knowing the orbital number of the studied state is highly desirable, which is possible in this regime.

In Paper III and IV, additional local side-gates [Figure 2.3(c)] were fabricated to controllably tune the single, strongly confined quantum dot, into two parallel quantum dots.

The second type of nanowire structure was the InAs/GaSb core-shell quantum dot [Figure 2.3(d)], where the electron and hole interaction were investigated [27]. As a vital step in realizing this type of structure, Namazi *et al.* [26] demonstrated that the relatively lower surface energy of wurtzite InAs compared to zinc blende could be used to suppress radial growth of GaSb. This

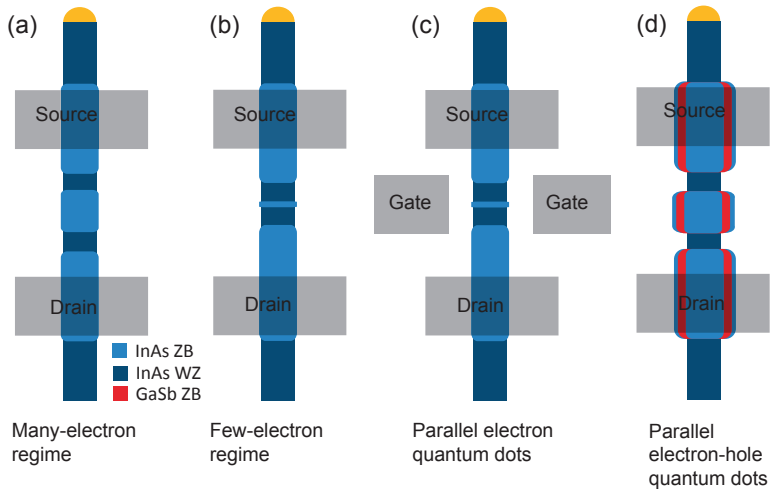

Figure 2.3: Nanowire device designs developed and studied in this thesis work. All devices consisted of Ohmic source and drain contacts and the oxide covered substrate acted as a capacitively coupled global back-gate. Devices (a)-(c) employed crystal phase-defined quantum dots with (a) weaker and (b,c) stronger quantum confinement. Device type (c) had additional local side gates. (d) InAs/GaSb core-shell quantum dot.

enabled the tailoring of zinc blende InAs/GaSb core-shell segments separated with wurtzite InAs-only segments.

2.6 Extracting geometrical dimensions of quantum dots

To investigate the role of the nanowire geometry on the electrical properties, and conclude that it is indeed the wurtzite segments that define the quantum dot, it is important to extract the barrier and quantum dot axial extensions of electrically characterized nanowire devices. As seen in Figure 2.2(b,c), the axial configuration of wurtzite and zinc blende can be extracted from TEM images. However, to perform TEM, the nanowires need to be deposited on a transparent substrate, such as a copper grid-supported lacey carbon film, which is not a suitable substrate for contact processing. Although it is possible, transferring contacted wires to TEM grids is tedious work. Thus,

it is highly desirable to extract the geometry parameters from SEM imaging after electrical characterization. Figure 2.4 shows an SEM image of a typical quantum dot device. By aligning the electron beam with the crystal planes in the nanowire the different crystal phases could be distinguished using electron channeling contrast imaging (ECCI), a method typically used to detect defects in crystalline materials [53, 54].

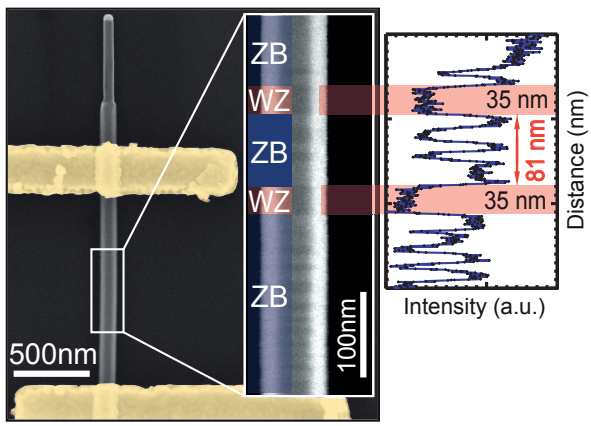

Figure 2.4: Scanning electron microscope (SEM) image of a nanowire device, with source and drain contacts (yellow); the inset shows a high-resolution image of the quantum dot area where the contrast profile is obtained by tilting the sample holder to exploit the electron channeling effect. Here, the wurtzite (red) and zinc blende (blue) segments have been indicated. The axial extension of the quantum dot and barriers segments were extracted from the intensity profile of the SEM image; the wurtzite segments were discriminated from the twinned segments in zinc blende using information on the structural composition from TEM analysis of nanowires from the same growth sample.

ECCI is based on the interaction of the wave nature of the electrons constituting the electron beam in the SEM and the crystal lattice of the sample. When the primary electron beam enters the crystalline sample, a lattice-coherent standing electron-density wave forms in the crystal. The amount of backscattering of electrons depends on the alignment of the electron beam and the lattice. More precisely, if the maxima of the electron-probability density coincide the with atomic sites in the crystal there occurs an increase in the backscattered signal. In the opposite case, if the maxima of the electron probability density are located between the atomic sites, the backscattering

becomes suppressed. When minimum backscattering is obtained, the process is called electron channeling.

Due to the different atomic orientations in zinc blende and wurtzite, the dimensions of both the wurtzite barriers and zinc blende quantum dot can be extracted from the intensity profile obtained in SEM images when the sample holder angle is optimized.

2.7 Estimation of tunnel barrier height

The tunnel current through a barrier is exponentially dependent on the height and width of the barrier. In the case of barriers defining a quantum dot, the height determines the number of possible bound states in the dot. As described in Paper I, we estimated the height of the barriers that the wurtzite segments imposed on the electron transport to ~ 95 meV. The electron concentration in the quantum dot was extracted by counting the number of Coulomb oscillations and dividing by the volume extracted from SEM images of the device. Figure 2.5 shows conductance as a function of gate voltage, starting from the region where we began to detect Coulomb oscillations ($V_g \approx -7$ V) to a point where the regular oscillations ceased ($V_g \approx 0$ V). Here, it is important to note that the quantum dot was not necessarily depleted at $V_g \approx -7$ V; and that the Fermi level at $V_g \approx 0$ V was not necessarily aligned with the conduction-band edge in wurtzite, see the illustration in Figure 2.5. When the Fermi level approached the top of the barriers, additional transport processes, such as higher order tunneling and thermionic emission, was dominating the transport. However, by counting the oscillations between these points in gate voltage, a lower limit of the electron concentration in the quantum dot can be extracted. For details on the estimation, see Paper I.

2.8 EBL-defined seed particles for nanowire growth

2.8.1 Limitations in nanowire growth using aerosol particles

When developing advanced quantum dot-structures it is important to be able to tune the geometry with high control during epitaxial growth. For the

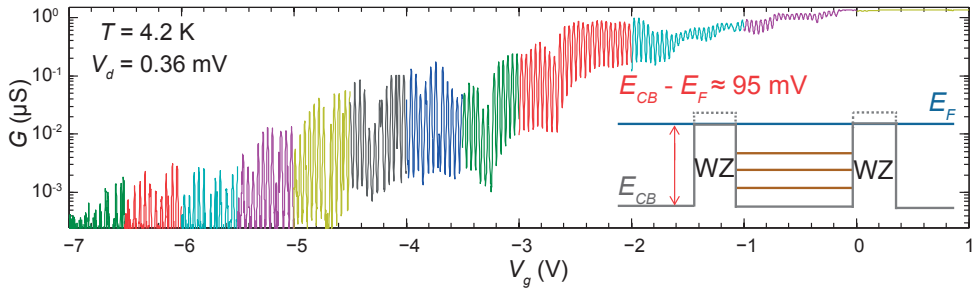

Figure 2.5: Conductance (G) as a function of gate voltage (V_g). The color coding indicates that this graph consists of several individual measurements merged together. The inset illustrates alignment of the conduction-band edge (E_{CB}) with the Fermi level (E_F) at the point where the Coulomb oscillations cease at approximately $V_g = 0$ V.

nanowire devices studied in this work, two different sets of Au aerosol particles, with approximate diameters of 40 nm and 30 nm, respectively, were used as seed particles to enable growth. These particles were randomly distributed on the growth substrate with an approximate areal density of 1 μm^{-2}, see Figure 2.6(a). In terms of seed particles, there are two important factors contributing to a variation of the nanowire and quantum dot geometry. First, the nominal variation in diameter of the seed particles ($2 - 3$ nm) gives rise to a variation in diameter of the nanowires. In addition, the difference in diameter also affects the length of different segments in the nanowire since the growth rates are roughly inversely proportional to the diameter of the seed particle, resulting in shorter segments for larger particle diameters. One should also note that the diameter affects the growth window for the different crystal phases [59]. Second, the spread in the areal density of the seed particles gives a variation in the length of the nanowire segments due to competition for material during growth. Nanowires located where the areal density of the seed particle is nominally lower, experience a higher concentration of precursors, giving rise to a faster growth rate.

2.8.2 Arrays of seed particles

Using arrays of seed particles for nanowire growth increases control and reproducibility of the dimensions. The fabrication process of electron beam

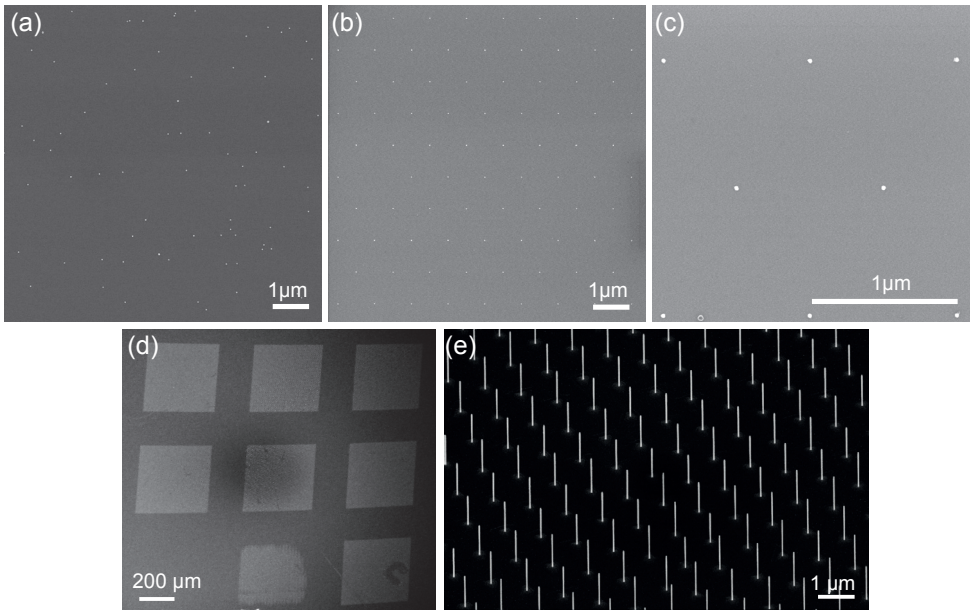

Figure 2.6: SEM images: (a) Au aerosol particles with a diameter of 39 (±5.5 nm and an areal density of 0.87 μm^{-2} (Image contribution: Robert Hallberg). (b) and (c) Low and high resolution images of EBL-defined Au particles with a 1 μm pitch and a diameter of approximately 25 nm. For exposure, VOYAGER High speed EBL from Raith with 50 kV acceleration voltage and 3 fC dose was used. (d) Overview image of a sample after nanowire growth with square fields with different particle sizes. (e) A zoomed-in view of nanowire arrays.

lithography (EBL)-defined seed particles follows roughly the same steps as the contact fabrication. $(\bar{1}\bar{1}\bar{1})$-oriented InAs substrates identical to the ones used for the aerosol particles were employed for EBL-defined particles. Here, a clean substrate was vital before starting the process of depositing resist (ARP 6200.09). After EBL exposure and development of resist, 20 nm Au was evaporated on the substrate. Figures 2.6(b) and (c) show SEM images of the resulting particles after the lift-off was complete.

In contrast to the random distribution of aerosol particles on the substrate, an exact pitch can be defined when designing the EBL pattern. Here, a hexagonal pattern with a pitch of 1 μm was used. Having equidistant particles resulted in a more equal precursor concentration at all particle sites within a certain distance from the edge of the pattern, and thus more uniform quantum

dot dimensions.

As mentioned above, the size of the particles is of utmost importance. A sample containing different particle sizes was designed in order to optimize the process of obtaining nanowires with suitable quantum dot geometries. Here, different electron doses in the point-exposure mode were used to vary the particle sizes. Figure 2.8(d) displays such a sample after nanowire growth. The lower left corner, with the lowest electron dose of 1 fC, did not result in high quality arrays and thus exhibited no nanowire growth. Figure 2.8(e) shows an image of one region with successful nanowire growth.

2.9 Nanowire device fabrication

This section will give a description of the processing involved in fabrication of single nanowire devices for transport measurements. First, the nanowires were mechanically transferred from the growth substrate to a measurement substrate. In the case of nanowires grown from aerosol particles, the tip of a cleanroom tissue paper was used in the transfer process. Whereas in the case of nanowires grown from arrays, a micro-manipulator tool was used for increased control during the transfer process [63]. The measurement substrate was a degenerately n-doped silicon chip covered with a 110-nm thick layer of thermally grown SiO_2, and had predefined Au pads, EBL-alignment markers and coordinate system, see Figures 2.7(a) and (b). The back of the substrate was covered with Au and functioned as a global back-gate during electrical measurements.

2.9.1 The measurement substrate

The measurement substrates were fabricated using standard EBL and UV-lithographic techniques, starting from a 2" silicon wafer. A photo of such a wafer after the completion of the fabrication process is shown in Figure 2.7(c). The wafer was subsequently cleaved into approximately 3 mm by 6 mm chips using a semi-automatic scriber.

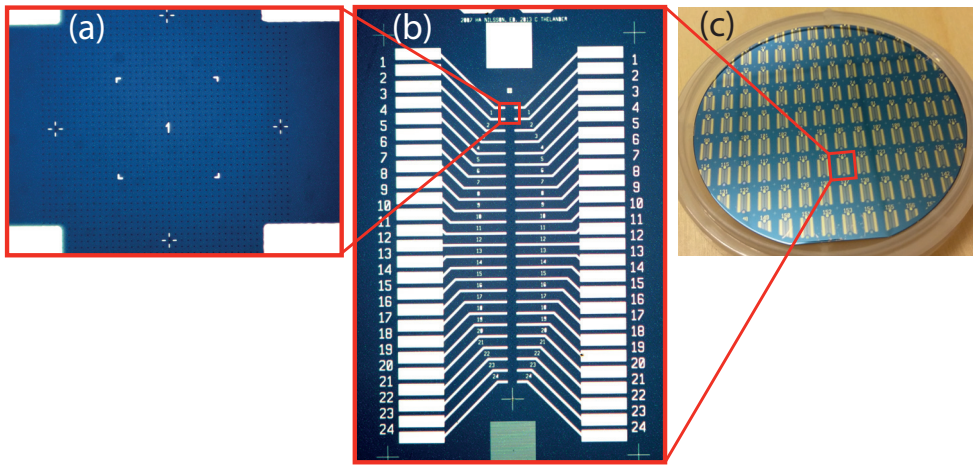

Figure 2.7: (a) Optical microscope image of a "gap" where the number *1* indicates the origin of the coordinate system. The four L-shaped markers were located 20 μm from the origin in both the y- and x-directions. The distance between the small dots was 2.5 μm. (b) Optical microscope image of a single measurement substrate containing 24 "gaps" with Au pads and leads. (c) Photo of a 2" Si wafer, containing several measurement substrates, after completing the processing.

2.9.2 Fabrication of source, drain and side-gate contacts

After deposition of nanowires on the measurement substrate, suitable device candidates were located using low-resolution SEM imaging, see Figure 2.8(a). There images were later imported into a LabVIEW program developed by Claes Thelander [64] to semi-automatically create design files used in the EBL exposure, see Figure 2.8(b). Figure 2.8(c) shows the original SEM images with a superimposed contact design.

Figure 2.9 shows the different processing steps involved in defining source and drain contacts on nanowires. After deposition of nanowires on the measurement substrate, see Figure 2.9(a), and the SEM imaging described above, the measurement substrate was spin-coated with EBL-resist (polymethyl methacrylate, PMMA 950 A5) and baked on a hotplate for 10 min, see Figure 2.9(b). Subsequently, the design files created in LabVIEW were used to define the contacts using EBL [Figure 2.9(c)]. PMMA is a positive resist at moderate exposure doses, meaning that during development the areas exposed to the electron beam will dissolve [Figure 2.9(d)]. Next, O_2-plasma ashing and

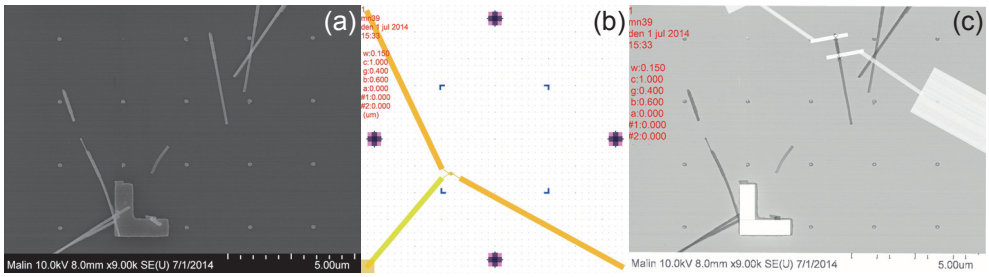

Figure 2.8: (a) Low-resolution SEM image of a nanowire selected for contact processing. (b) Visualization of the design file used in the EBL exposure. (c) The original SEM image with the design file superimposed. The L-shaped structure is a part of the coordinate system on the measurement substrates that enables alignment of the contacts.

chemical wet etching were performed to remove resist residue and native oxide, respectively, on the exposed nanowire areas. In the work presented here, HCl(37% bulk solution):H_2O (1:20) was used in the etching process for all samples to keep the processing identical, since it is suitable for both InAs and GaSb surfaces. It is worth noting that sulphur passivation (NH_4S_x at elevated temperature), which is commonly used for obtaining good ohmic contacts on wurtzite InAs nanowires, resulted in an increased electron concentration and undepletable devices when used on the InAs crystal phase quantum dot devices. In the next step, the sample was covered with a thin layer of metal (Ni/Au or Ti/Au) [Figure 2.9(e)] by physical vapor deposition prior to lift-off in hot acetone [Figure 2.9(e)]. Finally, the pre-fabricated gold pads and thus the nanowire devices were connected to macroscopic voltage sources and measurement equipment by means of metallic wire bonds that were mounted using a semi-automatic wire-bonding machine.

2.9.3 Fabrication of top-gate contacts

As a step in the development of the InAs/GaSb core-shell structures, local top-gates have been used to probe the interplay of electrons and holes in one-dimensional structures, such as reported by Namasi *et al.* [26]. Here, a stronger gate coupling to the nanowire was obtained by connecting the top-gate and the global back-gate. However, the additional non-native oxide covering the nanowire when the top-gate design was used, introduced additional

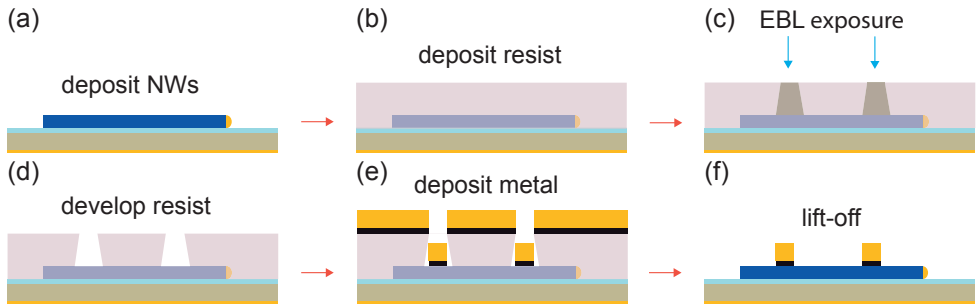

Figure 2.9: Schematic illustration of the processing steps involved when defining metal contacts on nanowires. (a) Nanowires were deposited on a measurement substrate. (b) The substrate was spin-coated with EBL-resist. (c) The contact design was projected onto the sample using electron-beam writing. (d) The exposed regions dissolved during resist development. (e) A thin layer of metal was evaporated on the substrate. Here, two metals were used, a very thin layer of Ni or Ti for better adhesion, followed by gold.

surface-charge states which could affect the electric properties of the system.

The top-gates were fabricated in a similar manner as the source and drain contacts. When the processing of source and drain contacts was complete, resist residues were removed in a second O_2-plasma etching step. Subsequently, an HfO_2 gate oxide layer (7 nm) was deposited using atomic layer deposition (ALD). Next, windows in the oxide layer were created using focused ion beam milling in order to connect the EBL defined gate-contacts to the predefined Au pads on the measurement substrate. Finally, the EBL and metallization processes described in Figure 2.9 were repeated to create the gate contacts.

Chapter 3

Single quantum dots

This chapter provides an introduction to charge and spin transport in single quantum dots. The commonly used characterization tool, the Coulomb charge stability diagram, is introduced, starting from the constant interaction model. Experimental data from transport in both the many-electron and the fully depletable few-electron regimes is presented. Furthermore, both first- and second-order tunnel processes are addressed as well as the effect of the quasi-one-dimensional properties of the semiconductor leads on the transport. Finally, spin-related phenomena such as the Zeeman effect and spin-orbit interaction are introduced.

3.1 Quantization effects

There are two aspects leading to the quantization of the electron transport via quantum dots. First, the quantized nature of the electron charge together with the electrostatic Coulomb interaction between the electrons in the quantum dot give rise to a quantization effect. The change in the electrochemical potential needed to overcome this quantization energy, and add an electron to the quantum dot, is called the charging energy (E_C). The charging energy increases for decreasing quantum dot sizes. Second, quantum confinement gives rise to a single-particle energy level separation (E_Δ), which is inversely proportional to the square of the length of the system in the direction where the system is largest and to the effective mass (m^*) of the charge carriers in the material. In the artificial atom picture, the single-particle energy levels are

sometimes referred to as orbitals, and these expressions are used interchangeably in this thesis. Typically, it is said that quantum confinement effects start to become important when the de Broglie wavelength ($\approx$ Fermi wavelength) $\lambda_F = h/\sqrt{(2m^*E_F)}$ of the electrons is comparable to the size of the system. Here, E_F is the electrochemical potential, or the so-called Fermi level of the system. Although the Fermi wavelength depends on the Fermi level, as an indication of the magnitude, Fermi wavelengths between 22-33 nm [65] and 17-22 nm [66] have been reported for non-intentionally doped InAs nanowires. However, it should be noted that the temperature (T) plays an important role; the quantization effect becomes detectable when $kT < E_\Delta, E_C$, where k is the Boltzmann constant.

3.2 Constant interaction model

A widely used simple model to describe the energetics of quantum dots is the constant interaction (CI) model [29]. In the CI model, two assumptions are made; first, the interactions of electrons in the quantum dot and the surrounding electrons are assumed to be parameterized by one constant capacitance, the self-capacitance. Second, the quantum dot orbitals are assumed not to depend on the number of electrons (N) in the quantum dot. These assumptions are crude approximations when the quantum dot is populated with only a few electrons. In the few-electron limit, the capacitance is no longer a geometrical property due to the poor screening in the quantum dot, and is instead strongly dependent on N and the specific potential landscape, such as charged surface states [29, 67]. However, the CI model is useful for estimating energy scales even in the few-electron regime. This section derives the change in electrochemical potential of the quantum dot required to add an electron, based on Refs. [68, 69].

Figure 3.1(a) shows a schematic illustration of the equivalent circuit for the quantum dot used in the CI model. Here, the quantum dot is tunnel-coupled to the source (C_s, R_s) and drain (C_d, R_d) contacts and capacitively coupled to the gate contact (C_g). In general, the charge on a conductor i (quantum dot) surrounded by m conductors (source, drain and gate contacts) is given by

$$Q_i = \sum_{j=0}^{m} C_{ij} V_j, \tag{3.1}$$

where C_{ij} is the capacitance between the quantum dot i and contact j, and V_j is the electrostatic potential of the contact j. If the quantum dot is defined as $i = 0$, the electrostatic potential of the quantum dot can be written as

$$V_0(Q_0) = \frac{1}{C_\Sigma}\left(Q_0 - \sum_{j=1}^{m} C_{0j}V_j,\right), \tag{3.2}$$

where the self-capacitance ($C_{00} \equiv C_\Sigma$) is equal to the negative sum of all capacitances to the quantum dot due to charge neutrality ($\sum_{j=0}^{m} C_{0j} = 0$). Here, the electrostatic potential from the charge in the quantum dot when source, drain and gate electrostatic potentials are zero have been omitted. The total electrostatic energy of a quantum dot charged with N electrons ($Q_0 = -eN$) at fixed V_j is

$$U(N) = \int_0^{-eN} V_0(Q_0)dQ_0 = \frac{e^2N^2}{2C_\Sigma} + eN\left(\sum_{j=1}^{m}\frac{C_{0j}}{C_\Sigma}V_j\right). \tag{3.3}$$

In order to obtain the total energy ($E(N)$) of the quantum dot, the discrete values of the single-particle energy (ϵ_i) due to quantum confinement must be considered. Since these energies are assumed to be constant, hence independent of N, they are simply added to the electrostatic energy (given that $\epsilon_i < \epsilon_{i+1}$)

$$E(N) = \sum_{i=1}^{N}\epsilon_i + U(N) = \sum_{i=1}^{N}\epsilon_i + \frac{e^2N^2}{2C_\Sigma} + eN\left(\sum_{j=1}^{m}\frac{C_{0j}}{C_\Sigma}V_j\right). \tag{3.4}$$

Next, the electrochemical potential (μ_N), defined as the change in the total energy of the quantum dot when adding the Nth electron to it, can be deduced according to

$$\mu_N = E(N) - E(N-1) = \epsilon_N + \frac{e^2}{C_\Sigma}\left(N - \frac{1}{2}\right) - e\left(\sum_{j=1}^{m}\alpha_j V_j\right), \tag{3.5}$$

where the lever arm $\alpha_j = -\frac{C_{0j}}{C_\Sigma}$ of contact j is introduced. Here, α_g is the gate-lever arm and can be used to translate the gate voltage to the energy scale of the induced shifts of electrochemical potential in the quantum dot. Finally,

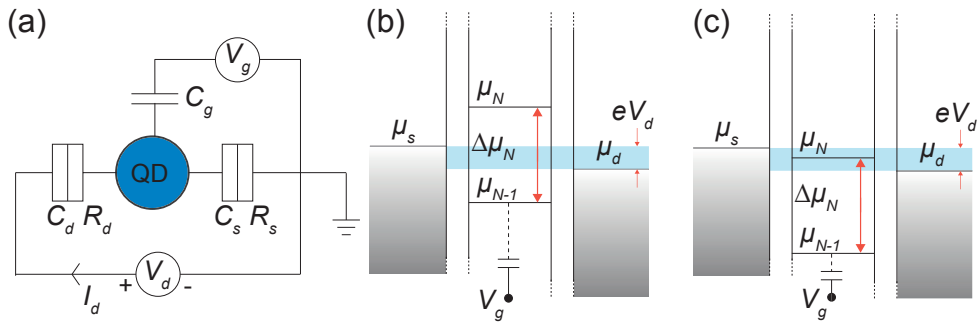

Figure 3.1: (a) Schematic illustration of the equivalent circuit used to describe a single quantum dot in the CI model where source and drain (gate) are tunnel (capacitively)-coupled to the quantum dot. (b) Schematic diagram of the electrochemical potential levels of a single quantum dot coupled to source and drain electrochemical potentials (μ_s and μ_d) in the Coulomb blockade regime. Here, the quantum dot has a constant occupation of $N-1$ electrons. A small bias (V_d) is applied as indicated by the blue shaded area. The electrochemical potential levels in the quantum dot can be shifted relative to μ_s and μ_d by tuning the gate voltage (V_g). (c) The Coulomb blockade is lifted when the electrochemical potential level μ_N enters the bias window and the electron occupancy in the quantum dot alternates between $N-1$ and N.

the addition energy ($E_{add}(N)$) is introduced as the change in electrochemical potential when adding the Nth electron to the quantum dot

$$E_{add}(N) \equiv \Delta\mu_N = \mu_N - \mu_{N-1} = \epsilon_N - \epsilon_{N-1} + \frac{e^2}{C_\Sigma}. \tag{3.6}$$

This can be written in a more condensed manner,

$$E_{add}(N) = E_\Delta(N) + E_C, \tag{3.7}$$

where the spacing of the single-particle energy levels ($E_\Delta(N)$) is the chemical contribution and the charging energy ($E_C = \frac{e^2}{C_\Sigma}$) is the electrostatic contribution.

Figures 3.1(b) and (c) show schematic illustrations of the electrochemical potential diagram of a quantum dot tunnel-coupled to source and drain electrodes. In (b), no electrochemical potential level in the quantum dot is aligned with the bias window (indicated as a blue shaded area) and the system is in

the so-called Coulomb blockade regime, where no single-electron tunneling processes are allowed. However, the electrochemical potential levels can be shifted electrostatically by means of the gate. In (c), an electrochemical potential level is aligned with the bias window, leading to a current through the quantum dot due to a sequential tunneling of electrons. This means that the current can be turned ON and OFF by tuning the potential on the gate, just like a transistor, and such a device is in fact called a single-electron transistor.

There are two conditions that need to be met in order to observe single-electron tunneling due to the quantized nature of the electron charge:

1. $R_t > \frac{h}{e^2} = 25.8$ kΩ, i.e., the tunnel resistance per barrier (R_t) must be smaller than the quantum resistance. This condition is necessary for the energy uncertainty to be smaller than E_C, leading to localized states in the quantum dot. A simple, intuitive motivation of the condition can be made using the Heisenberg uncertainty principle; the fluctuations of the electron population in the dot due to tunneling must occur on a smaller time scale than the measurements ($\sim$ *charge/current*), which gives a lower boundary for the time to charge/discharge the dot $\Delta t = R_t C_\Sigma$. From this, the given condition on R_t can be extracted from the Heisenberg uncertainty principle: $\Delta E \Delta t \gtrsim h$ $[(e^2/C_\Sigma)R_t C_\Sigma \gtrsim h]$ [29].

2. $\frac{e^2}{C_\Sigma} = E_C > kT$ to prohibit thermal smearing of the Coulomb blockade.

In addition, if $V_d < \frac{E_C}{e} = \frac{e}{C_\Sigma}$, only events where an electron tunneling into the dot, followed by an electron tunneling out of the dot prior to a second electron tunneling into the dot, are allowed. However, if $E_\Delta < E_C$, several single-particle energy levels can contribute to the electron transport, but if $V_d < \frac{E_C}{e}$, this merely affects the tunnel probability due to the extra tunnel channels, and not the number of electrons tunneling into the dot before an electron tunnels out.

The quantization of the electrochemical potential in the quantum dot results in an oscillating current level (I_d) through the system when sweeping the gate voltage (V_g) at small bias (V_d), referred to as Coulomb oscillations, see Figure 3.2. The frequency of the oscillations is dependent on the quantum dot size. In the case of the longer quantum dot in (a), the frequency is constant, indicating a dominant electrostatic contribution to the addition energy with no detectable quantum confinement effect, thus $E_{add} = E_C$. However, in

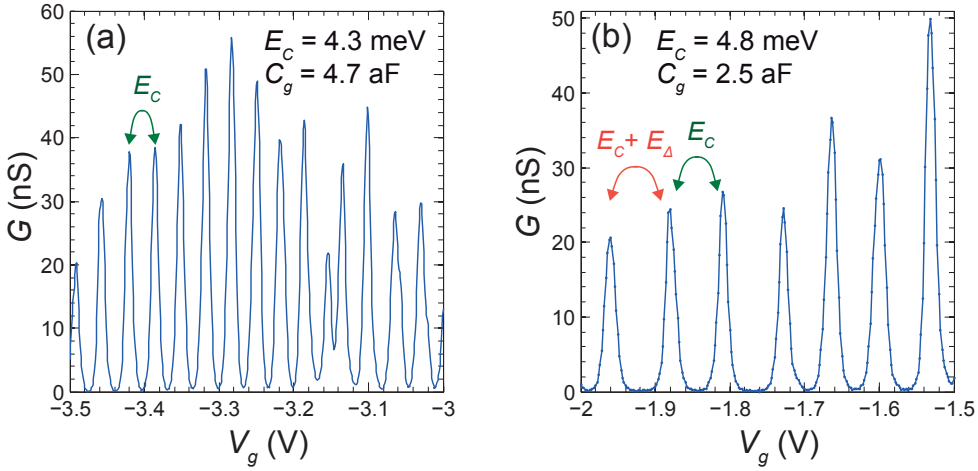

Figure 3.2: Conductance (G) as a function of gate voltage (V_g) recorded for InAs nanowire devices containing: (a) a longer quantum dot ($L_{QD} = 81$ nm, $D = 78$ nm) and (b) a shorter quantum dot ($L_{QD} = 27$ nm, $D = 71$ nm), where L_{QD} and D are the quantum dot length and diameter, respectively. The measurements were performed at $V_d = 0.36$ mV and $T = 4.2$ K.

the case of the smaller quantum dot in (b), where the radius ≈ 35 nm is the larger dimension, an odd-even pattern of the peak spacing is seen. This is typical for systems where the spin-degenerate quantized single-particle energy levels are resolved. Here, $E_{add} = E_\Delta + E_C$ for populating a single-particle energy level with the first electron (odd N) and $E_{add} = E_C$ for populating the same single-particle energy level with a second electron of opposite spin (even N). In addition, Figure 3.2 shows that E_C increased when the geometrical dimensions of the quantum dot decreased (increase in confinement). This quantum dot-size reduction was also reflected in a decrease of C_g. Furthermore, gate-voltage dependence in the amplitude of the Coulomb peaks was seen. This dependence was due to both the energy-dependent density of states in the quasi-one-dimensional semiconductor leads and a variation in the tunnel-coupling between different states in the quantum dot and conducting subbands in the leads.

3.3 Coulomb charge stability diagram

In order to characterize the electron transport through a quantum dot in detail and extract parameters such as E_C, E_Δ and C_g, a so-called Coulomb charge stability diagram can be recorded. Figure 3.3 shows an illustration of such a two-dimensional intensity diagram where the differential conductance (dI_d/dV_d) is typically plotted as a function of source-drain bias (V_d) and gate potential (V_g). In Figure 3.3, each transition via a state in the quantum dot is associated with a "V"-shaped black line, which corresponds to a change in conductance. Here, a negative slope means that the electrochemical potential of the particular state in the quantum dot is aligned with μ_s and a positive slope indicates that the electrochemical potential of the state is aligned with μ_d. "V"-shapes associated with different transitions (via subsequent ground states) define the borders of the so-called Coulomb diamonds (white regions), which correspond to regions where no single-electron tunnel processes are allowed and where the electron occupation (N) in the quantum dot is fixed. This situation is referred to as Coulomb blockade. Here, transport via excited states and second-order tunneling have been neglected in the discussion, and are instead addressed in Section 3.6.

Now follows a detailed discussion of electrochemical-potential alignment at different points in the stability diagram. Starting from the bottom, the large, non-closing Coulomb diamond indicates a quantum dot fully depleted of electrons ($N = 0$). By increasing V_g, the electrochemical potential level of the first state in the quantum dot aligns with the electrochemical potentials of the source and drain at point (A) ($V_d = 0$ V) and the black lines originating from this point (defining the adjacent diamonds) are associated with permission of transport via the first orbital in the quantum dot. In the light blue areas, only one electrochemical potential level is situated in the bias window and the transport is of the single-electron type. Here, the electron occupation in the quantum dot fluctuates between N and $N + 1$. The lines defining the dark blue areas are associated with an onset (offset) of two-electron transport. Here, two electrochemical potential levels are in the bias window allowing two electrons to tunnel into the dot before one electron tunnels out.

Moving towards more positive V_g, in point (F), the second electrochemical potential level in the quantum dot is aligned with the electrochemical potentials of the source and drain. As for point (A), the black lines originating

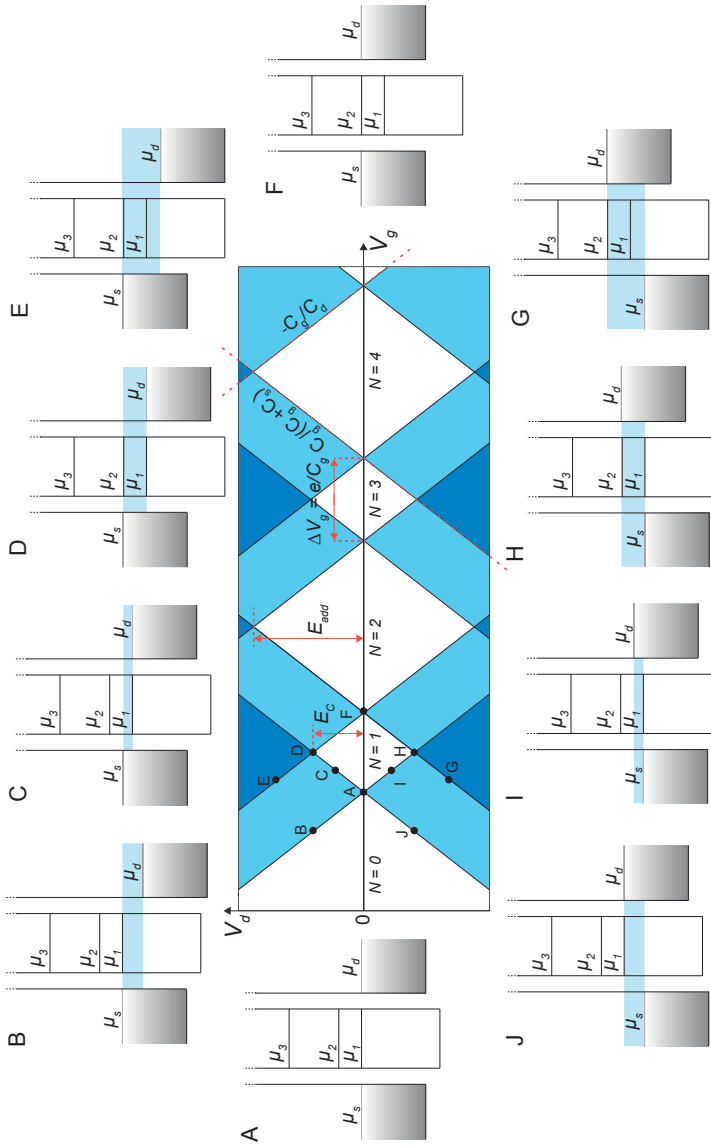

Figure 3.3: Schematic illustration of a charge stability diagram (spin-degenerate system) where the black lines indicate a change in the conductance (I_d/V_d) as a function bias (V_d) of gate voltage (V_g). Here, the source is grounded and the drain is voltage biased. Within the white areas, the so-called Coulomb diamonds, the system is in Coulomb blockade, hence, the electron population in the quantum dot is fixed. In the light (dark) blue areas, one (two) energy level(s) in the quantum dot is (are) located in the bias window. Electrochemical-potential diagrams at different points (A - J) in the transport process are illustrated.

from point (F) (defining the adjacent diamonds) are associated with the onset (offset) of transport of a second electron in the quantum dot. However, this transport involves the same single-particle energy level as in (A) but with opposite spin. This odd-even pattern of small and large Coulomb diamonds is typical for a spin-degenerate system with $E_C \sim E_\Delta > kT$. If $E_C >> E_\Delta$, the charge diagram would consist exclusively of smaller diamonds.

From the height of the diamonds, measured from $V_d = 0$ V, values for E_{add} can be extracted, see Figure 3.3. In the case of the smaller diamonds $E_{add} = E_C$ and, assuming constant E_C within an orbital, E_Δ can be estimated from the height of the larger diamonds using $E_{add} = E_C + E_\Delta$ (Eq. 3.7). In addition, E_Δ can also be directly extracted from the diamond-intersection points of conduction lines associated with transport involving excited sates; this is discussed further in Sections 3.5 and 4.5. Furthermore, $C_g = \frac{e}{\Delta V_g}$ can be determined from the width (ΔV_g) of the smaller diamonds.

Symmetric diamonds shown here are typical for systems where the source and drain capacitances are similar in magnitude, and dominating the system ($C_s \approx C_d > C_g$), which is often the case for back-gated quantum dots in nanowires. The expressions for the slopes of the diamond edges noted in Figure 3.3 can be derived from Eq. 3.5, in a similar manner as in Ref. [69]. However, here, asymmetric biasing has been assumed where V_s is grounded, see Figure 3.1(a). Assuming $C_s \approx C_d > C_g$, the gate lever arm can be extracted from the height and width of a diamond:

$$e\Delta V_g = \frac{E_C}{\alpha_g}, \tag{3.8}$$

where ΔV_g is the width of one diamond at $V_d = 0$ V and

$$\alpha_g = \frac{\Delta V_d}{\Delta V_g}. \tag{3.9}$$

3.4 Transport in many-electron quantum dots

By tuning the geometrical dimensions of the quantum dot and electrostatic potential via gate electrodes, the electron population of the quantum dot can be controlled. A system is considered to be in the many-electron regime when the electron population is in the limit where electron screening results in an orbital-independent charging energy (E_C). Paper I, describes the investigation

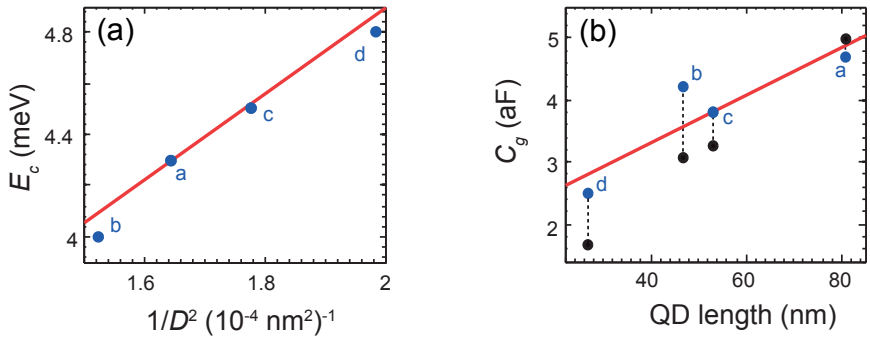

Figure 3.4: (a) Charging energy (E_C) as a function of $\frac{1}{D^2}$, where D is the quantum dot diameter. (b) Gate capacitance (C_g) as a function of length of the quantum dot segment: experimental (blue) and analytical (black) data. The red lines are linear fits to the experimental data.

of the relation between parameters such as the charging energy (E_C) and gate capacitance (C_g), and the dimensions of the quantum dot in the many-electron regime, see Figure 3.4. The motivation for this was to verify that it was indeed the wurtzite barriers that defined the quantum dot. In Figure 3.4(a), E_C increases linearly with respect to $\frac{1}{D^2}$, where D is the quantum dot diameter. This is typical for disc-shaped quantum dots where the source and drain capacitances dominate ($E_C = \frac{e^2}{C_\Sigma}$). In a simple picture one would also expect a linear trend of extracted C_g in Figure 3.4(b). However, Device B has a somewhat higher value of C_g than the linear trend, which can be explained by the larger diameter of the nanowire leading to a higher capacitance to the gate. The analytical result for C_g, obtained using an infinite-cylinder-on-a-plane type of model [45], agreed rather well with the experimentally extracted values, particularly in the case of Device A which was the longest quantum dot. However, a discrepancy was seen in the case of the three shorter devices, which can be explained by non-neglectable fringe capacitances at the tunnel barriers. For details on the analytical method, see Paper I and Ref. [70].

Signatures of almost orbital independent charging energy ($E_c \approx 4$ meV) over a large back-gate region is visible in the Coulomb charge stability diagram [Figure 3.5] recoded in the many-electron regime for a quantum dot of similar axial length as device D in Figure 3.4. The single-orbital energy separation was estimated to be $\sim 1-2$ meV from $E_\Delta = E_{add} - E_c$. In addition to the Coulomb blockade patterns, positive conductance lines running perpendicular

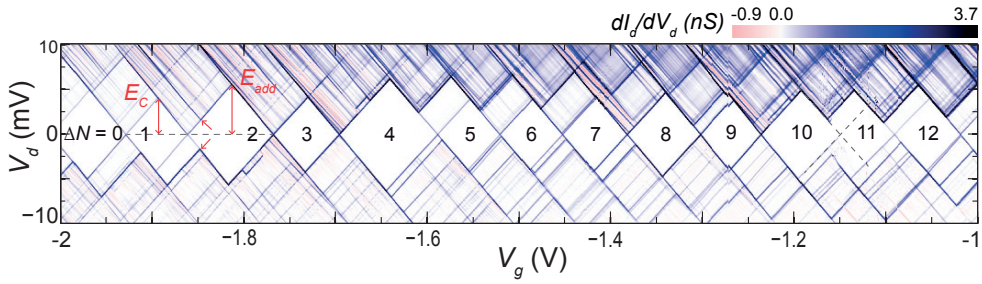

Figure 3.5: Coulomb change stability diagram in the many-electron regime showing the differential conductance (dI_d/dV_d) as a function of source-drain bias (I_d) and back-gate (V_g) recorded at an approximate electron temperature of 150 mK. The quantum dot diameter was $\sim$ 100 nm and the axial length was $\sim 20 - 30$ nm. ΔN indicates the change in the number of electrons (N) populating the dot. The charging energy (E_C) and the addition (E_{add}) were extracted from the height of the diamonds with odd and even ΔN, respectively. Two conductance lines originating from transitions via excited states are indicated with arrows. Dashed lines have been added to guide the eye at the $\Delta N = 10 - 11$ transition.

to the diamond edges, corresponding to the onset of tunnel transport via excited states, are visible in Figure 3.5, and indicated with arrows. Here, the transport was still sequential, however the tunneling could occur either via the ground state or the excited state, resulting in an increase in tunnel probability and hence in conductance. Transport via excited states is addressed in more detail in Section 3.6. Furthermore, both positive and negative differential conductance lines appeared due to fluctuations in tunnel-coupling between lead- and quantum-dot states, which is further discussed in Section 3.4.1.

3.4.1 Lead states

In the Coulomb stability diagrams in Figures 3.5 and 3.6(d), peaks in differential conductance not involving modulation of the quantum dot states are clearly visible as lines/stripes running outside of the blockade regions. These variations arose from gate modulation of the one-dimensional energy subbands in the semiconductor leads. When tuning the gate potential, the coupling strength between different lead states and the quantum dot states became modulated. This modulation is reflected as an increase (blue) or decrease (red) of the conductance in the system. Such signatures are commonly

observed in quantum dot systems with semiconductor leads. However, in quantum dot systems with metal leads, these effects are not visible due to the absence of gate modulation of the lead-density of states.

3.5 Transport in few-electron quantum dots

When the quantum confinement of the quantum dot is increased further, the electron population can be controlled down to a completely depleted quantum dot. In this limit, typically referred to as the few-electron region, the charging energy is highly orbital-dependent. Few-electron quantum dots are desirable for studies on few-electron Coulomb interaction, spin- and correlation effects.

One major issue when approaching depletion of quantum dots with nanowire leads by electrostatic gating is that also the electron concentration in the quasi-one-dimensional leads becomes reduced, and formation of unwanted serial quantum dots may appear [67]. This is especially prominent in nanowires of the wurtzite crystal phase where the electron concentration is lower than for zinc blende. Multi-dot formation can be avoided by a strong axial confinement which results in the energy states of the quantum dot shifting up as compared to the lead states.

Experimental data from a strongly confined quantum dot is shown in Figure 3.6(a), where full depletion is confirmed by the abrupt drop in conductance as the back-gate voltage decreases. In the few-electron regime, sweeping the gate potential towards more negative values did not only affect the electron population in the quantum dot, but also substantially modulated the confining potential and shifted the spatial extension of the quantum dot towards the top part of the nanowire cross section, as illustrated in Figure 3.6(b). The Coulomb charge stability diagram [Figure 3.6(d)] also shows the signature of a depleted quantum dot in the non-closing of the $N = 0$ blockade region. When populating the quantum dot, by increasing the back-gate voltage, the typical odd-even pattern of the Coulomb diamonds appears, characteristic of spin-degenerate orbitals. Here, the height of the small diamonds directly give the charging energy for the states with odd N, whereas for the states with even N the diamond height together with the energy extracted from the excited-state lines (indicated by arrows) are used to obtain the charging energy. Furthermore, cotunneling involving the excited state is seen in the

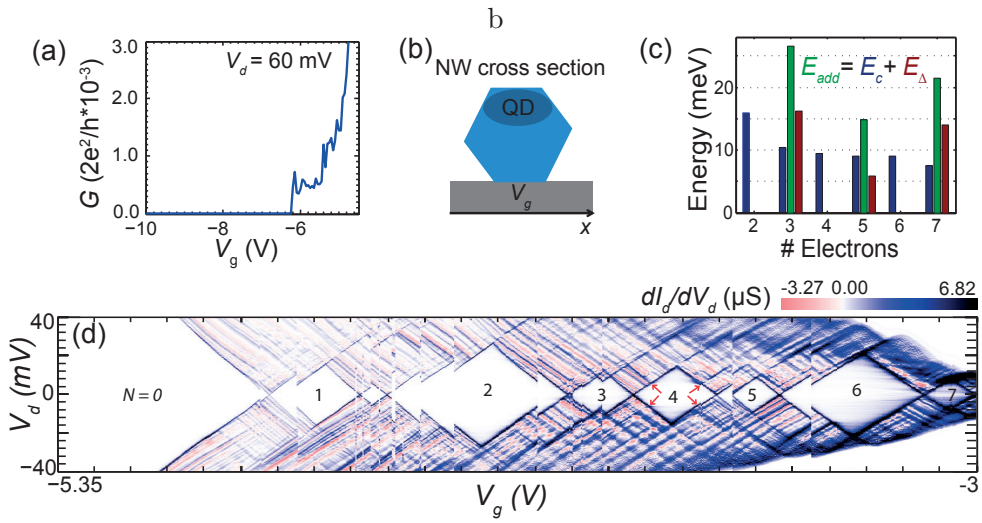

Figure 3.6: (a) Conductance (G) as a function of back-gate (V_g) for a strongly confined quantum dot with axial extension of ($\sim$ 5 nm.) and a diameter of $\sim$ 80 nm. (b) Illustration of the spatial extension of the quantum dot (QD, dark blue) in the nanowire cross section when a negative gate potential is applied. (c) Extracted addition energy (E_{add}), charging energy (E_C) and single orbital energy spacing (E_Δ). (d) Coulomb charge stability diagram in the few-electron regime showing differential conductance (dI_d/dV_d) as a function of source-drain bias (I_d) and back-gate (V_g) recorded at an approximate electron temperature of 150 mK. The red arrows indicate the conductance lines associated with transport involving the excited state.

even-N Coulomb-blockade diamonds. The cotunneling process is discussed further in Section 3.6. As seen in Figure 3.6(c), the quantum dot exhibited strong quantum confinement, and both the orbital spacing and charging energy varied between states. A maximum single-orbital spacing of the first and second orbitals of close to 30 meV was measured for this type of nanowire quantum dot device.

3.6 Transport via excited states and cotunneling

In addition to sequential tunneling via ground states, also sequential tunneling via excited states and higher-order (in tunnel coupling) tunneling can contribute to transport in quantum dot devices. The latter, also called cotun-

neling, involves coherent tunneling events of several electrons [71, 72]. Figure 3.7 shows a sketch of a Coulomb blockade diamond where the different tunnel processes are indicated.

First, the sequential tunneling via excited states is addressed. This process occurs outside of the blockade regions (diamonds) when an excited state enters the bias window, as illustrated by marker A in Figure 3.7. Here, the bias window is not large enough to allow sequential addition of two electrons into the dot, however, the addition of an extra transport channel gives rise to a peak in the differential conductance, and thus a line in the stability diagram.

In contrast to the previous case, cotunneling can occur in the blockade regions. Here, the "blockade" refers to a blockade of single-electron tunneling. Cotunneling involves correlated tunneling events of several electrons, with an intermediate, energetically forbidden state, or virtual state. The virtual state is allowed if the tunneling time scale is shorter than the time scale in the Heisenberg uncertainty principle. Thus, the prevalence of cotunneling is strongly dependent of the quantum dot-to-source/drain coupling strength. Cotunneling is divided into elastic and inelastic processes. Elastic cotunneling involves the ground state, and can occur at any source/drain bias. This process is indicated by the B-marker in Figure 3.7. When increasing the source/drain bias corresponding to the energy separation of the ground and excited states, an onset of inelastic cotunneling occurs, see Figure 3.7 panel (C) and (D). Although the total energy of the system is conserved, the quantum dot starts in the ground state and ends up in an excited state, hence the name inelastic. If the excited state is located in the bias window, as in panel (C) in Figure 3.7, the cotunneling event ends with the possibility of a sequential tunneling event. This is called cotunneling-assisted sequential tunneling [73, 74]. However, if the excited state is located below the bias widow, as in panel (D), sequential tunneling is not allowed.

In the cotunneling process described above, the spin does not play a crucial role. However, if a spin-degenerate state in the quantum dot is populated with one spin and the coupling between the dot and the leads are strong, a many-body singlet state of the spin on the dot and delocalized spins in the leads can form. The tunneling process of this state gives rise to a zero-bias conductance peak in the diamond and a spin-flip of the quantum-dot state. This phenomena is referred to as the Kondo effect [75–78].

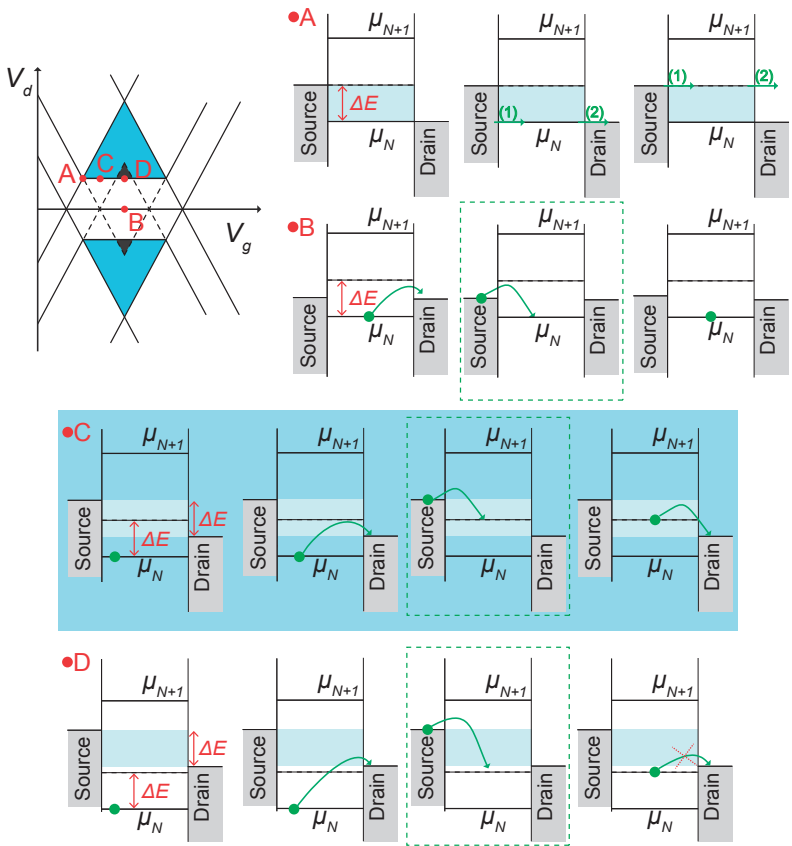

Figure 3.7: Sketch of a Coulomb-blockade diamond with an electron population of N. Four different tunneling processes are indicated in the stability diagram and illustrated by schematic electrochemical-potential diagrams (A)-(D), where ΔE is the energy difference between the levels; (A) Sequential tunneling via the ground or excited state. (B) Elastic cotunneling, allowed inside the whole Coulomb diamond. In (B)-(D) the energetically forbidden, virtual states are indicated with green dashed boxes. (C) Inelastic cotunneling with cotunneling-assisted sequential tunneling allowed in the regions with blue shading in the Coulomb diamond. (D) Inelastic cotunneling without cotunneling-assisted sequential tunneling, allowed in the gray regions in the Coulomb diamond.

3.7 Zeeman effect in few-electron quantum dots

In an external magnetic field (B), the spin-degenerate orbital states split into two separate energy states. At moderate B-fields, the energy separation can be described by the difference in the linear Zeeman energy $\Delta E_z = (s_\uparrow - s_\downarrow)|g^*|\mu_B B$, where $s_\uparrow = \frac{1}{2}$ and $s_\downarrow = -\frac{1}{2}$ are the spin states of the electrons, g^* is the effective g-factor (which can be orbital dependent) and μ_B is the Bohr magneton [32, 79].

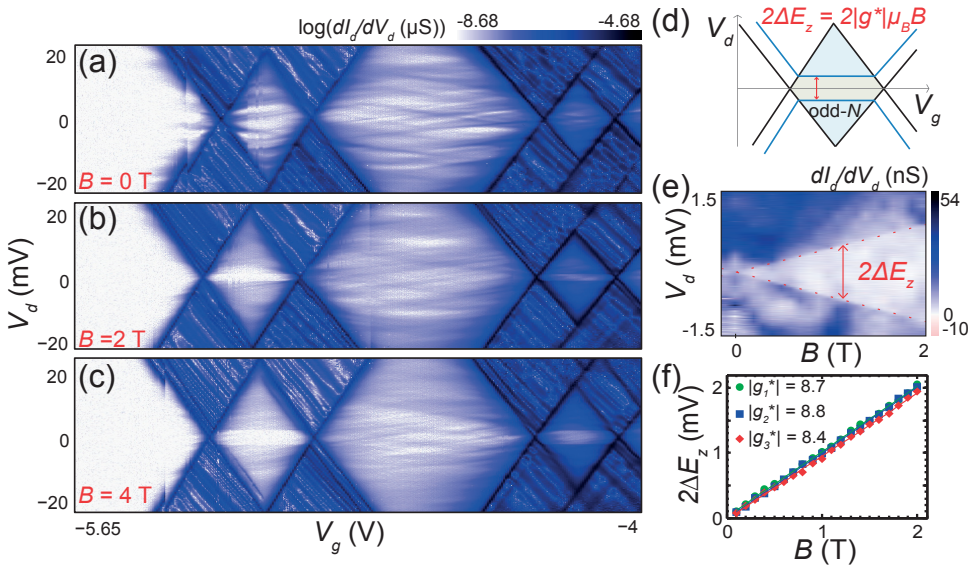

Figure 3.8: (a)-(c) Coulomb charge stability diagrams showing differential conductance (dI_d/dV_d) in log-scale for the first four electrons (N = 1-4) as a function of source-drain bias (I_d) and back-gate (V_g) recorded at different external magnetic fields (B) perpendicular to the substrate. Sloped conductance lines inside the Coulomb diamonds were attributed to elastic cotunneling, where the slope of the lines was due to the gate-induced modulation of the coupling between the quantum dot and the lead states. (d) Sketch of an odd-N Coulomb diamond where the $|g^*|$-factor was extracted from the onset of inelastic cotunneling using the Zeeman energy (E_z). (e) The B-field evolution of the onset of inelastic cotunneling. (f) The $|g^*|$-factor for the three first orbitals were extracted from the slope of the extracted separation of the inelastic cotunneling onset ($2\Delta E_z$) as a function of B.

In bulk semiconductor structures, the g^*-factors typically differ from the value of the free electron (+2), and are in many cases negative [g^* = -14.8 (InAs), -7.8 (GaSb)] [80, 81]. This renormalization is due to the spin-orbit interaction (SOI) coupling the spin and orbital-angular momentum, leading to a momentum-dependent Zeeman energy [82]. The resulting g^*-factor varies greatly for different crystal-phase orientations [83, 84], degrees of quantum confinement [85–89] and orbitals [90–93]. The SOI and anisotropy of the g^*-factor are discussed further in Section 3.8.

$|g^*|$-factors are commonly extracted from the magnetic field evolution of the quantum dot states as a function of gate potential or source/drain bias [91]. However, another method is to use the B-field dependent onset of inelastic cotunneling in the odd populated diamond [94], see Figure 3.8. Here, the ground and excited states involved in the cotunneling are the Zeeman split spin-up and spin-down states. This method is used to extract the $|g^*|$-factors for the three first orbitals [Figure 3.8] in the strongly confined quantum dot discussed in Figure 3.6. In contrast to other reports [90, 91], we saw no apparent orbital dependence of the $|g^*|$-factors.

3.8 Spin-orbit interaction and anisotropic $|g^*|$-factor

An electron moving in an electric field will experience an effective magnetic field which will act on the magnetic moment (spin) of the electron. This results in an effective coupling between the orbital motion and spin, referred to as the spin-orbit interaction (SOI). The SOI can be introduced in the Schrödinger equation as a relativistic correction: $H_{SO} = -(\hbar/4m^2c^2)(\sigma \cdot \mathbf{p} \times \nabla V)$, where m and c are the electron mass and the speed of light, σ is the Pauli operator, $\mathbf{p}$ is the momentum operator and V is the potential [95]. In atoms, the SOI appears as a consequence of the electrons moving in the Coulomb potential from the nucleus, and the effect increases for heavier atoms with stronger nuclear fields.

In semiconductors there are two distinguishable sources of SOI: one intrinsic contribution due to bulk inversion asymmetry (BIA) of the zinc blende crystal phase, called the Dresselhaus term. The second one, called the Rashba term, is an extrinsic contribution due to structural inversion asymmetry (SIA)

Table 3.1: The effective $|g|$-factors ($|g^*|$) of the three lowest orbitals (n) for the magnetic field aligned with the three principal axes of the nanowire.

Orbital (n)	$\|g^*\|$ ($\phi = 0$)	$\|g^*\|$ ($\theta + \theta_0 = 0, \phi = 90$)	$\|g^*\|$ ($\theta + \theta_0 = 90, \phi = 90$)
1	8.7	8.2	6.6
2	8.8	8.0	6.1
3	8.4	7.7	6.1

arising from asymmetry in the confining potential. This confining potential asymmetry can be due to heterostructures, external gating and electric fields at the surface of the system. In quantum dots, the SOI hybridizes states with different spin and orbitals, such as singlet and triplet states, and assists non-spin conserving transitions [16]. This is addressed further in Chapter 4.

Furthermore, both BIA and SIA contribute to the renormalization of the g-factor, and the anisotropic nature of the SOI results in an anisotropic $|g^*|$-factor [35, 94, 96–99]. In general, the three-dimensional anisotropy of the $|g^*|$-factor can be expressed by a diagonal tensor [92, 94, 96, 97, 100]

$$|g^*|(B) = \frac{1}{|B|}\sqrt{(g_1 B_1)^2 + (g_2 B_2)^2 + (g_3 B_3)^2)} \tag{3.10}$$

where $g_{1(2,3)}$ and $B_{1(2,3)}$ are the effective g-factor and magnetic field component in the principal axes.

In Figure 3.9, experimental values of the $|g^*|$-factors (extracted as previously discussed) as a function of the in-substrate plane angle (θ) for the three first orbitals (n) are fitted with the phenomenological expression

$$|g^*|(\theta) = \sqrt{(|g_1|cos(\theta + \theta_0))^2 + ((|g_2|sin(\theta + \theta_0))^2}. \tag{3.11}$$

Here, $\theta_0 = 33^\circ$ is the offset angle of the nanowire relative to the principal axis of the B-field. From this analysis, the maximum and minimum $|g^*|$-factors coincide with the B-field being respectively aligned with and perpendicular to the axial direction of the nanowire. Table 3.1 summarize the $|g^*|$-factors of the three lowest orbitals for the principal axes of the nanowire.

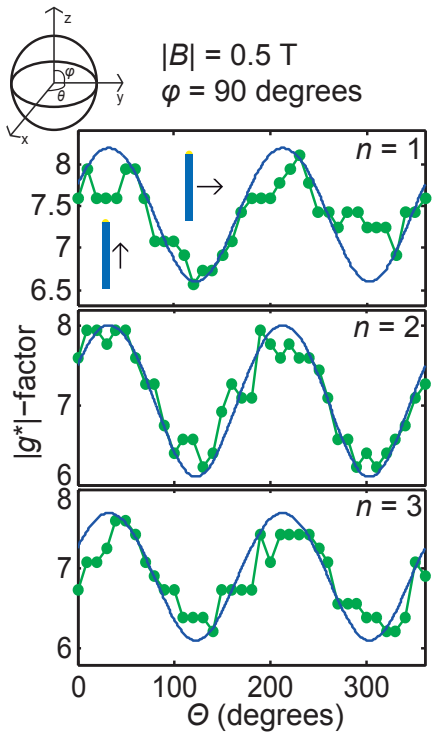

Figure 3.9: The effective $|g|$-factors ($|g^*|$) of the three first orbitals ($n = 1 - 3$) as a function of the in-substrate plane angle (θ). The alignment of the B-field with respect to the nanowire is illustrated in the insets.

Chapter 4

Parallel-coupled double quantum dots

This chapter provides an introduction to charge and spin transport in parallel-coupled double quantum dots. The focus is on the few-electron regime, including the transitions from a fully depleted system to one- and two-electron population of the first orbitals in the system. Also, the implication of hybridized states on the transport is addressed. Furthermore, the parallel-coupled double quantum dot system discussed in Papers III and IV is introduced together with experimental data. Finally, the tuning of the spin transport is broken down in more detail.

4.1 Forming double quantum dots - parallel and serial coupling

Similar to the single quantum dots discussed in Section 2.1, double quantum dots can be realized in various material systems such as by gating planar GaAs/AlGaAs 2DEGs [101], in carbon nanotubes [102–105] or in self-assembled quasi-one-dimensional structurers [23]. Here, I highlight two comprehensive review papers on the transport physics in serial-coupled double quantum dots by Hanson *et al.* and van der Wiel *et al.* [16, 106].

Double quantum dots are categorized by their tunnel-coupling (Γ) geometry to the source and drain being either *parallel-* or *serial*-coupled, as de-

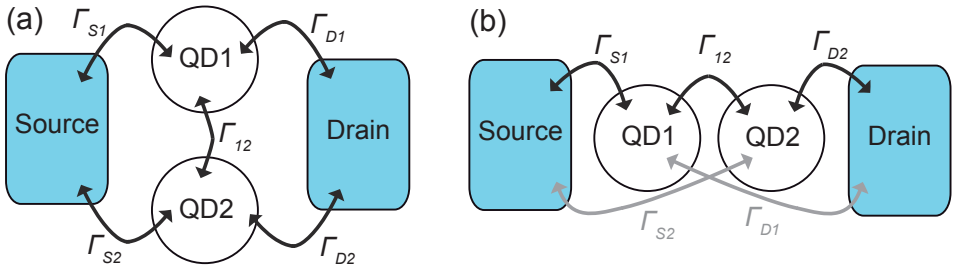

Figure 4.1: Sketch of (a) parallel and (b) serial tunnel coupling (Γ) of the double dots (1 and 2) to the source (S) and drain (D). In (b), the grey arrows $\Gamma_{D(S)1(2)}$ denote the cotunneling rate, a tunnel process allowed even when the electrochemical potentials on the two dots are not aligned.

picted in Figure 4.1. There also exist additional coupling geometries that fall in between these categories [107]. Serial-coupled quantum dots are employed as building blocks to realize qubits [4] using the possibility of spin filtering via the Pauli-spin blockade, and is the most studied coupling-type. For low-biased serial-coupled quantum dots, only the regime where the electrochemical potential of dot 1 and 2 are aligned can be probed by first-order tunneling spectroscopy. Higher-order tunneling processes can be probed when only the electrochemical potential of one of the dots is in the bias window. This type of process is indicated by grey arrows in Figure 4.1. In order to obtain a full charge stability diagram of the system, charge sensors located in the vicinity of the double dots are routinely used to detect all types of charge transitions, including transitions between the two dots.

The parallel-coupling configuration opens the door to full probing of the first-order tunneling charge transitions with DC-measurements of the current through the double dot system. Since the work included in this thesis concerns parallel-coupled quantum dots, the focus will from now on be on this type of coupling.

Parallel-coupled quantum dots have been extensively studied in the GaAs system by Hatano *et al.* [108–111]. However, the low bulk $|g^*|$-factor (~ 0.44) and weak spin-orbit coupling in GaAs limits the possibility to manipulate and study the evolution of spin states in this system. The same group also studied parallel-coupled quantum dots in the InAs material system [23, 24]. In addition to a stronger quantization effect, the InAs material system offered

a larger bulk $|g^*|$-factor ($\sim$ -14.8) and a stronger spin-orbit coupling.

A similar system as the one described in Paper III and IV was studied in Refs. [112, 113]. Their devices consisted of side-gated InAs wurtzite nanowires with quantum dots formed by InP barriers. However, the authors did not address the formation of parallel-coupled double dots in this system.

4.2 The constant interaction model

In a manner similar to the single quantum dot discussed in Section 3.2, the electrostatics of the double quantum dot can be described in a purely classical regime by capacitors using the constant interaction model. An equivalent circuit of the double dot system is displayed in Figure 4.2(a). The resistances have been obmitted in the sketch. Both the left (l) and right (r) dots were capacitively coupled to the global back-gate ($C_{BG_{l(r)}}$) and the local side-gates ($C_{L(R)_l(r)}$, $C_{L(R)_r(l)}$). The couplings to the source and drain are represented by a parallel-coupled capacitance $C_{D,l(r)}$, $C_{S,l(r)}$. The additional interdot coupling was parametrized by the capacitance C_m. $N_{l(r)}$ denotes the electron population for the left (right) dot. The model presented here is a modified version based on the physical concepts derived by van der Wiel *et al.* in [106]. Next, we considered the linear transport regime ($V_{SD} \sim 0$), and for the sake of simplicity the cross capacitances, such as between left (right) dot and right (left) side-gate or other stray capacitances were assumed to be negligible. The electrostatic energy of the double dot system can be derived as

$$\begin{aligned} U(N_l, N_r) &= \tfrac{1}{2}N_l^2 E_{Cl} + \tfrac{1}{2}N_r^2 E_{Cr} + N_l N_r V_{inter} \\ &\quad + f(V_L, V_R), \\ f(V_L, V_R) &= \tfrac{1}{-|e|}[C_{L,l}V_{L,l}\left(N_l E_{Cl} + N_r V_{inter}\right) \\ &\quad + C_{R,r}V_{R,r}\left(N_l V_{inter} + N_r E_{Cr}\right)] \\ &\quad \tfrac{1}{e^2}[\tfrac{1}{2}C_{L,l}^2 V_{L,l}^2 E_{Cl} + \tfrac{1}{2}C_{R,r}^2 V_{R,r}^2 E_{Cr} \\ &\quad + C_{L,l}V_{L,l}C_{R,r}V_{R,r}V_{inter}], \end{aligned} \tag{4.1}$$

where $E_{Cl(r)}$ and e are the charging energies of the left (right) dot and the elementary charge, respectively, and V_{inter} is the electrostatic coupling energy,

thus the change in energy of one dot when an electron is added to the other dot. These energies can be expressed as

$$E_{Cl} = \frac{e^2}{C_l}\left(\frac{1}{1-\frac{C_m^2}{C_l C_r}}\right), \tag{4.2}$$

$$E_{Cr} = \frac{e^2}{C_r}\left(\frac{1}{1-\frac{C_m^2}{C_l C_r}}\right), \tag{4.3}$$

$$V_{inter} = \frac{e^2}{C_m}\left(\frac{1}{\frac{C_l C_r}{C_m^2}-1}\right), \tag{4.4}$$

where $C_{l(r)} = C_{L(R),l(r)} + C_{S,l(r)} + C_{D,l(r)} + C_m$ is the sum of the capacitances to the left (right) dot.

Using the expression for the electrostatic energy (Eq. 4.1), the following electrochemical potentials of the two dots can be derived

$$\begin{aligned}\mu_l(N_l,N_r) &\equiv U(N_l,N_r) - U(N_l-1,N_r)\\ &= \left(N_l - \tfrac{1}{2}\right)E_{Cl} + N_r V_{inter} - \tfrac{1}{|e|}\left(C_{L,l}V_L E_{Cl} + C_{R,r}V_R V_{inter}\right)\end{aligned} \tag{4.5}$$

$$\begin{aligned}\mu_r(N_l,N_r) &\equiv U(N_l,N_r) - U(N_l,N_r-1)\\ &= \left(N_r - \tfrac{1}{2}\right)E_{Cr} + N_l V_{inter} - \tfrac{1}{|e|}\left(C_{L,l}V_L V_{inter} + C_{R,r}V_R E_{Cr}\right).\end{aligned} \tag{4.6}$$

Let us first discuss two extreme cases when it comes to the interdot coupling. Negligible coupling $C_m = 0$ means two capacitively uncoupled quantum dots. The total energy of the system reduces to the sum of the energies of the two separate dots. In this case, adding an electron to one dot will not affect the electrostatics on the other dot. This is illustrated by the straight lines in Figure 4.2(b), which shows a schematic charge stability diagram of the equilibrium electron numbers (N_l, N_r) as a function of the side-gate voltages (V_L, V_R). Here, the electrochemical potential on the source and drain is defined as zero in the absence of an applied bias, and the lines indicate a change in the equilibrium charge numbers in the dots when $\mu_{l(r)} = 0$ aligned with μ_s and μ_d. In the other extreme case, where C_m is the dominant capacitance,

the system is effectively one single big dot with a total charge of $N_l + N_r$. A sketch of the charge stability diagram in the single dot regime is shown in Figure 4.2(c). Here, both side-gates affect the equilibrium electron numbers, reflected in the straight lines with identical slopes.

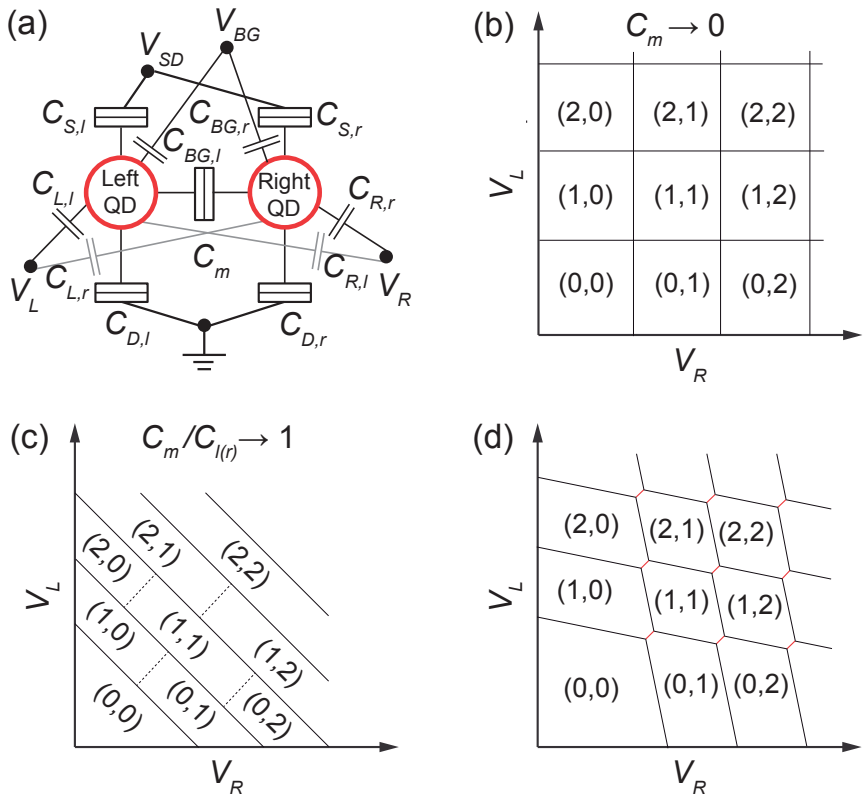

Figure 4.2: (a) Network of resistors and capacitors representing the two parallel-coupled quantum dots in the constant interaction model. Tunnel barriers connect both dots to the source and drain. The dots are capacitively coupled to three gates. (b)-(d) Charge stability diagrams showing the charge transition borders as a function of the two side gates for: (b) a decoupled double quantum dot, (c) a fully capacitively coupled double quantum dot (single dot) and (d) an intermediate capacitively coupled double quantum dot (honeycomb diagram). The equilibrium electron numbers (N_l, N_r) are indicated.

In the region of intermediate capacitive coupling, the lines indicating a change in the equilibrium charge numbers in the dots form a honeycomb pattern, see Figure 4.2(d). Adding the cross-capacitances ($C_{L(R),r(l)}$) modulated the slopes of the lines further away from the uncoupled case in Figure 4.2(b). The points connected by the red lines in Figure 4.2(d) are called triple points. At these points, and along the red lines, the electrochemical potential of the two dots are aligned. The distance between the triple points is determined by the interdot charging energy (V_{inter}). Crossing a red line corresponds to an electron tunneling from one dot to the other and does not change the total number of electrons on the double dot. Such a transition can be recorded in charge-sensing devices used when probing transport in serial-coupled quantum dots and the line will show in the measurements [16]. However, in parallel-coupled dots, where the full honeycomb stability diagram for first-order transport can be recorded directly by DC measurements, a charge transition between the dots will not be detected in the measurements, and thus no line connecting the triple points will appear.

4.3 Interdot tunnel coupling - hybridization of states

The previous section discussed the classical aspect of the interdot coupling. In addition to capacitive coupling, coherent tunneling between the two quantum dots couples the single-dot orbitals of the two dots. This tunnel coupling results in hybridization of single-dot orbitals, and the two new hybridized states, called the bonding and antibonding states, anticross when the energy of the uncoupled state is tuned into alignment. This is the same physical concept that gives rise to bonding and antibonding orbitals and molecular bonds, thus motivating the use of the term artificial molecules when addressing double dots.

A simple two-level model can be used to describe the coupling between single-dot orbitals [106]. The eigenstates $|\phi_1\rangle$ and $|\phi_2\rangle$ of the uncoupled system, with eigenvalues E_1 and E_2, become hybridized mediated by the tunnel-coupling (t), resulting in two new delocalized states: the bonding ($|\phi_B\rangle$) and antibonding ($|\phi_{AB}\rangle$) states. Maximum hybridization is reached at the crossing of the unperturbed states, and here the bonding and antibonding states can

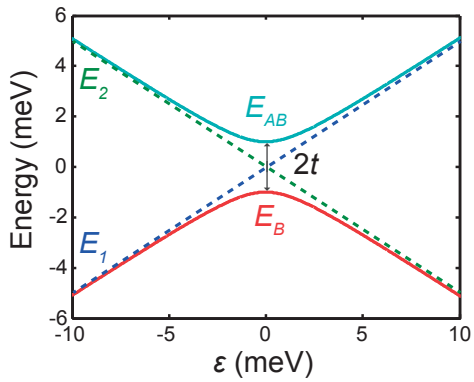

Figure 4.3: Energies for an uncoupled (E_1, E_2) and a coupled (E_B, E_{AB}) two-level system as a function of energy detuning (ε) of the uncoupled states. In the coupled case, the states anticross at $\varepsilon = 0$ with a magnitude of 2 $\times$ interdot tunnel coupling (t). In this calculation $t = 1$ meV.

be written as a superposition of the unperturbed states

$$|\phi_B\rangle = \frac{1}{\sqrt{2}}(|\phi_1\rangle - |\phi_2\rangle) \tag{4.7}$$

$$|\phi_{AB}\rangle = \frac{1}{\sqrt{2}}(|\phi_1\rangle + |\phi_2\rangle). \tag{4.8}$$

The hybridized states are separated in energy according to

$$\Delta E = E_{AB} - E_B = \sqrt{(2t)^2 + \varepsilon^2}, \tag{4.9}$$

where E_B and E_{AB} are the energies of the bonding and antiboning states, respectively, and $\varepsilon = E_2 - E_1$ is the energy detuning of the uncoupled states. Figure 4.3 shows the energies of the coupled and uncoupled states as a function of ε. The minimum energy separation is determined by the tunnel coupling $2t$. This energy decrease t of the ground state (bonding state) is reflected in the honeycomb stability diagram as a downwards shift and smoothing of the curvature of the transition line representing the addition of the first electron close to the triple points where $\varepsilon = 0$, see Figure 4.4. Note that this electron will populate a delocalized orbital, and in this regime the integers $N_{l(r)}$ are no longer well defined when the system is in an energy eigenstate. Since the bonding orbital is double spin degenerate one would expect the addition

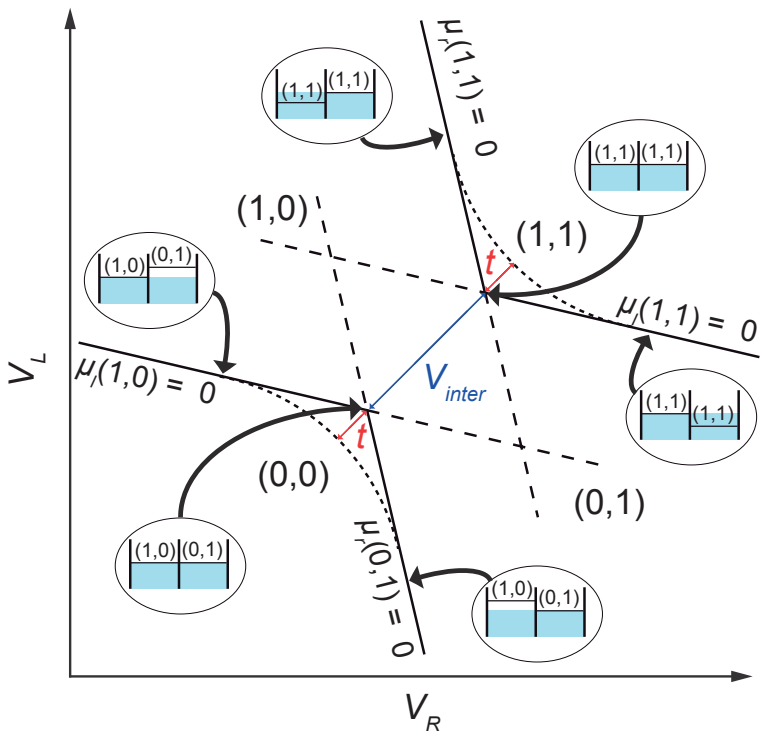

Figure 4.4: Sketch of a charge stability diagram zoomed-in on the first two triple points. The alignment of the electrochemical potentials ($\mu_{l(r)}$) of the two dots and source and drain at different gate configurations are indicated in the insets. Here, the top of the blue shaded area symbolizes the electrochemical potentials of the source and drain, which are both assumed to be zero (linear transport regime $V_{SD} \sim 0$). The interdot tunnel coupling shifts the ground state (bonding) down by an energy of t. V_{inter} is the interdot charging energy. Adapted from [16].

energy to be only the charging energy. However, in a simple picture where exchange interaction is omitted, when adding a second electron to the double dot system, the addition energy is the charging energy + $2t$. This discrepancy is explained by the strong Coulomb interaction between the two electrons, again localizing the states. The reduction with t when adding the first electron now has to be paid back. The orbital energy of the two-electron state is equal to $E_1 + E_2 = E_B + E_{AB}$ [16].

In conclusion, larger interdot tunnel coupling will give a softer curvature of the transition lines in the honeycomb stability diagram which can be clearly seen in the experimental results shown in Figure 4.5. Here, the tunnel coupling can be tuned continuously from a weak regime, where the two dots are localized and the capacitive coupling is dominant, to a strong regime, where the two dots effectively form a single quantum dot.

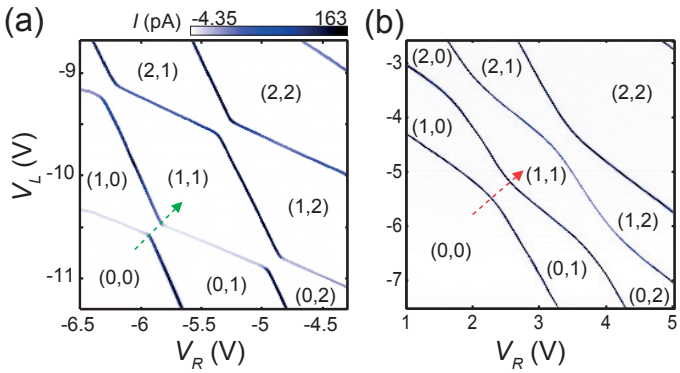

Figure 4.5: Honeycomb charge stability diagrams recorded in the weak (a) and strong (b) interdot tunnel coupling regimes. The equilibrium electron numbers (N_l, N_r) are noted. The arrows indicate the gate-vector connecting the two first triple points.

4.4 Exchange interaction - the singlet-triplet energy difference

The two-electron states with the electron population (1,1) can be either a spin singlet state (S(1,1)) or one of the spin triplet states (T_+(1,1), T_0(1,1),

$T_-(1,1)$). These states are defined as follows

$$S(1,1) = \left(|\uparrow_1\downarrow_2\rangle - |\downarrow_1\uparrow_2\rangle\right)/\sqrt{2} \tag{4.10}$$

$$T_+(1,1) = \left(|\uparrow_1\uparrow_2\rangle\right) \tag{4.11}$$

$$T_0(1,1) = \left(|\uparrow_1\downarrow_2\rangle + |\downarrow_1\uparrow_2\rangle\right)/\sqrt{2} \tag{4.12}$$

$$T_-(1,1) = \left(|\downarrow_1\downarrow_2\rangle\right) \tag{4.13}$$

where the subscript denotes in which dot the electrons reside. The triplet states ($T(1,1)$) are energetically degenerate in the absence of an external magnetic field. It is well known that the Coulomb energy for this two-electron system will be spin-dependent. This is understood since the total wave function of a pair of Fermions must be antisymmetric with respect to the interchange of electron coordinates. Thus, a singlet spin configuration which is antisymmetric must have a symmetric orbital wave function, and a triplet spin configuration (symmetric wave function) must have an antisymmetric orbital wave function. An antisymmetric orbital wave function means less spatial overlap between the electrons, and therefore a decreased Coulomb interaction compared with the case of a symmetric orbital wave function. This is called exchange interaction and it involves the same physical effect that is behind Hund's rule resulting in parallel spin-filling of orbitals in atomic subshells and ferromagnetism. This difference in Coulomb energy of symmetric and antisymmetric orbital wave functions is described by 2 times the exchange integral (V_x). Furthermore, the energy difference between single and triplet states (J) is often, somewhat confusingly, referred to as the exchange energy. However, J depends on both the interdot tunnel-coupling strength (t) and the exchange integral. In a simple version of the Hund-Muliken approximation [109, 114], where symmetric quantum dots and aligned single-dot orbitals are assumed, J can be expressed as

$$J = \frac{(2t)^2}{(U_{intra} - V_{inter})} - 2V_x. \tag{4.14}$$

Here, U_{intra} and V_{inter} are the single-dot and inter-dot charging energies. This simplified expression of J is only valid in the limit where $t << (U_{intra} - V_{inter})$. Intuitively, the expression can be understood as follows; since the spin triplet means one electron occupying each hybridized orbital, due to the Pauli exclusion principle, the larger the tunnel coupling between single-dot orbitals,

the larger the split of the hybridized orbitals, which leads to a larger J. In the case of a spin singlet, the two electrons can occupy the same hybridized orbital. The relation between the Coulomb interaction within one dot and between the dots modulates the tendency of single-dot and double-dot population. Thus, the exchange energy can be electrostatically tuned by the gates via the tunnel-coupling and the spatial distribution of the wave function [115].

In the double quantum dot system studied in Paper III and IV, the tunnel coupling can be tuned into a strong tunnel coupling regime where Eq. 4.14 is no longer valid. To reproduce the experimental results from the full range of tunnel couplings, a model including a single orbital in each dot is employed in Paper IV. This model was adapted from Stepanenko *et al.* [116]; for details on the model see the Supplementary information of Paper IV. Experimentally extracted values of the interdot tunnel coupling (t) and the intradot charging energies (U_{intra}) were used as input parameters for the simulations. Here, it is not possible to independently extract values for the interdot charging energy (V_{inter}) from the experimental data; the value that can be directly extracted includes the exchange integral. In contrast to Ref. [109], where V_x was assumed to be neglectable, we found that it was necessary to include V_x to obtain an agreement between experimental and modeled results. A value of $V_x \approx 50$ μeV was estimated by numerical fitting of the modeled J to the J extracted from the experimental data. This value could be compared with the value ($V_x \approx 15$ μeV) obtained in Ref. [109] by simply assuming that the discrepancy between J extracted from the experimental results and from Eq. 4.14 arose from the $2V_x$ term.

4.5 Extracting excited-state energies

Excited-state energies for both the one- and two electron states were extracted from the Coulomb charge stability diagrams recorded along the gate-vector running through the two triple points as indicated with arrows in Figure 4.5. Figure 4.6(c) shows such a stability diagram where the conductance lines associated with transitions involving the antibonding one-electron state are indicated with arrows. The possible energy transitions of the system going from one to two electrons are illustrated in Figure 4.6(a). These energy-transitions were transformed into electrochemical potentials in Figure 4.6(b) which are

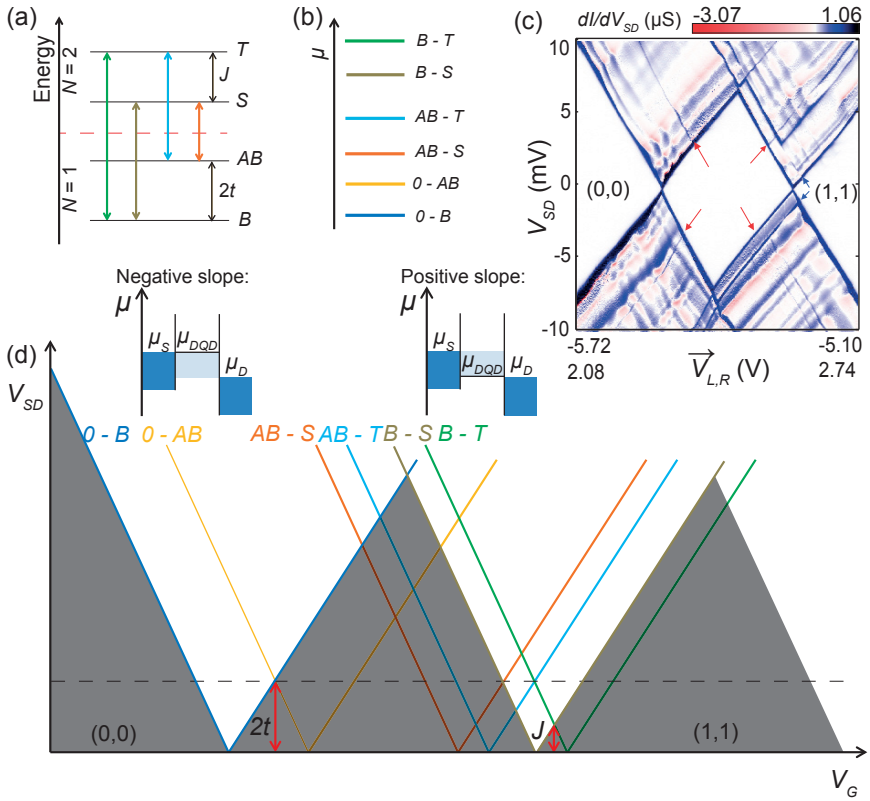

Figure 4.6: (a) Energy levels of the one- and two-electron states of the double dot system at zero external magnetic field. N denotes the total electron number in the system. The bonding (B) and antibonding (AB) states are separated by two times the interdot tunnel coupling (t) and the singlet (S) and triplet (T) are separated by the exchange energy (J). The colored arrows indicate possible energy transitions which are translated into a diagram of electrochemical potential in panel (b). The electrochemical potentials are probed in Coulomb charge stability measurements shown in panel (c). This diagram is recorded along the gate-vector connecting the first two triple points, as indicated by the arrows in Figure 4.5. The red arrows highlight conduction lines associated with transitions involving antibonding states, and these lines intersect with the diamond borders at $eV_{SD} = 2t$. In a similar manner, J can be extracted from the intersection of the triplet line and the diamond border. (d) Schematic Coulomb stability diagram showing the conduction lines associated with the electrochemical potentials in panel (b).

directly related to the conductance lines constituting the Coulomb stability diagram sketched in Figure 4.6(d). The one-electron excited state energy, i.e., the energy difference between the bonding (B) and antibonding (AB) states ($2t$), was extracted from the crossing point of the $0-B$ and $0-AB$ transitions. In a similar manner, the two-electron excited state energy (J) was extracted from the crossing point of $B-S$ and $B-T$ transitions.

Note that crossing a conductance line with negative slope from the left, for instance the yellow $0-AB$, means that the electrochemical potential for that particular transition enters the bias window from the top in the schematic electrochemical-potential diagram, allowing the transition from zero to one electron in the antibonding orbital. On the other hand, crossing the yellow conductance line with a positive slope from the right, is associated with the electrochemical potential entering the bias window from the bottom allowing the system to go from one electron in the antibonding state to zero electrons. With this in mind, going back to the experimental data in Figure 4.6(c), one sees that all conductance lines involving the transition starting from the one-electron ground state B as well as the two-electron ground and excited states S and T are visible. However, transitions starting from the excited one-electron state AB and going to zero electrons are not, which can be explained by a faster deexcitation rate to the B state than the tunneling rate in and out of the double dot.

4.6 Formation of parallel-coupled double quantum dots in nanowires

Papers III and IV address parallel-coupled quantum dots formed in a single crystal phase-defined quantum dot. Figure 4.7(a) shows an SEM image of a typical nanowire device coupled to a source-drain with bias (V_{SD}) and a set of three gates; a global back-gate (V_{BG}) and the two side-gates ($V_{L(R)}$). When an external magnetic field is applied, it is aligned perpendicularly to the substrate, as indicated in the image. The thin (< 10 nm) disk-shaped crystal phase-defined quantum dot can be seen in the high-resolution TEM image shown in Figure 4.7(b).

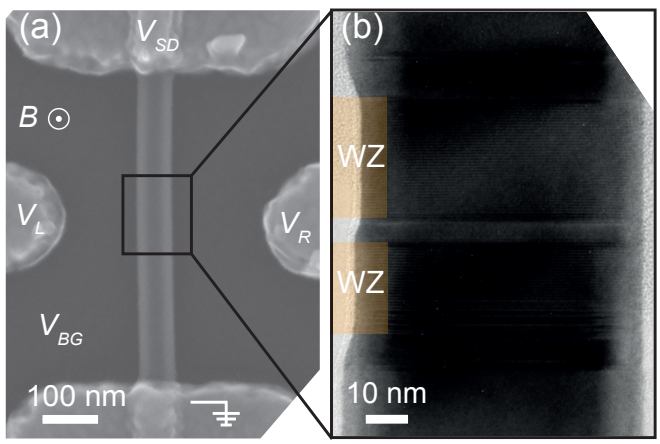

Figure 4.7: (a) Scanning electron microscope image of a typical side-gated ($V_{L(R)}$) quantum dot-nanowire device connected to a source-drain bias (V_{SD}) and a global back-gate (V_{BG}). When applied, the external magnetic field becomes perpendicularly aligned to the substrate. (b) High-resolution transmission electron microscope image viewed along a ⟨110⟩-direction of a typical crystal phase-defined single quantum dot. The axial extension of the zinc blende quantum dot was 4 nm, the wurtzite segments were 22 and 28 nm (highlighted) and the nanowire diameter of the single QD was 67 nm.

Figure 4.8(a) schematically shows a cross section of a nanowire with two potential pockets (quantum dots). These pockets can be formed by tuning the set of gates, or they can form spontaneously when the electron population approaches full depletion. We attribute the formation of parallel-coupled dots to an uneven distribution of surface charges on the circumferences of the disc-shaped quantum dot.

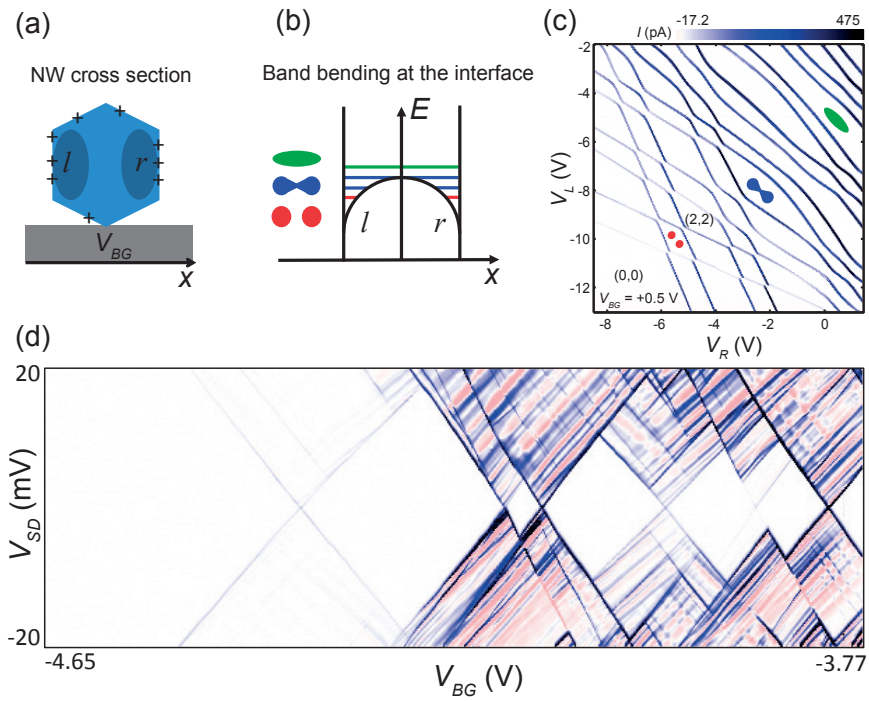

Figure 4.8: (a) Sketch of the nanowire cross-section indicating the uneven distribution of surface charges and the resulting formation of potential pockets (quantum dots) by darker regions. (b) Simplified diagram of the conduction-band bending at the nanowire surface creating a shallow tunnel barrier between the quantum dots. As the electron population of the double dots increase the two dots merge into one single dot. (c) Honeycomb charge stability diagram as a function of the left (right) side-gates ($V_{L(R)}$) at a fixed back-gate (V_{BG}) showing the transition from a double-dot to a single-dot system. (d) Coulomb charge stability diagram recorded for a similar disc-shaped quantum dot device as shown in Figure 4.7 but without side gates. An external magnetic field ($B = 8$ T) is applied at this particular recording but is not essential for the spontaneous formation of parallel quantum dots.

InAs is known to exhibit bending of the conduction-band edge at the surface due to surface states such as intrinsic adatoms [117, 118], native oxide [119, 120] or adsorption of hydrogen [118, 121, 122]. In nanowires, the transport characteristics due to this accumulation layer at the surface are highly contributing to the overall transport properties, and become increasingly important when the radius is decreased [123–125]. It is known that an uneven distribution of surface charges along the nanowire axis can create potential pockets at the surface resulting in serial quantum dots [67]. Here, an uneven distribution of surface charges along the circumference of the quantum dot causes a variation in the band bending giving rise to the formation of parallel-coupled quantum dots. Figure 4.8(b) shows a sketch of the conduction-band edge as a function of the length of the nanowire cross-section.

By sweeping the side-gates at a fixed back-gate, the formation of the double dot can be tuned and a honeycomb stability diagram can be recorded, see Figure 4.8(c). Here, the large open white area in the lower left corner serves as a solid indication that the system is fully depleted of electrons. The sharp edges at the first couple of triple points reveal a dominantly capacitively coupled system. Since the potential wells defining the dot were shallow, as indicated in Figure 4.8(b), filling the double dots with electrons would bring the system into a region of strong overlap between the spatial electron distributions of the two dots. This effectively created a single dot, resulting in the straight conduction line in the upper right corner.

While tuning the set of gates allows to split the single quantum dot in a controlled manner, we also observed the spontaneous formation of parallel-coupled double quantum dots without applying side-gate voltages. As previously discussed, this was believed to be related to an uneven distribution of surface charges along the circumference of the quantum dot illustrated in Figure 4.8(a). Figure 4.8(d) shows a Coulomb stability diagram recorded for a solely back-gated device, where a characteristic superposition of diamond patterns of different slopes appeared close to electron depletion, indicating such a spontaneous formation of parallel-coupled dots.

The spatial overlap of the electron distributions, and thus the interdot tunnel coupling was tuned by the gates, as shown in Figure 4.9(a). Typically, around $V_{BG} \sim 0$ V, minimum overlap was obtained, as indicated by the insets showing the real part of the electron wave function of the bonding state for the first electron. As the back-gate decreased (increased), the wave func-

tion was pushed (pulled) to the top (bottom) of the nanowire cross-section, effectively leading to an increase in overlap (see inset) and interdot tunnel coupling. Since the energy separation between the single and triplet (J) depends on t, J was also modulated with the back-gate, as seen in Figure 4.9(b). Figure 4.9(c) shows a close to linear correlation between J and $(2t)^2$, as predicted by equation 4.14.

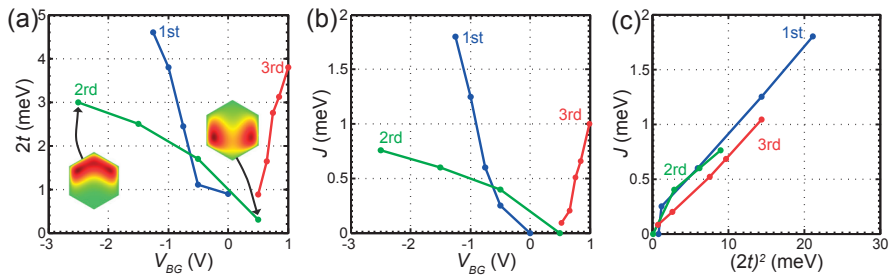

Figure 4.9: (a) interdot tunnel coupling (t) and (b) singlet/triplet energy separation (J) as a function of the back-gate (V_{BG}) recorded for three separate cooldowns. The insets in (a) show the real part of the electron wave function of the bonding states at corresponding gate configurations. The wave functions were calculated by solving the Poisson equation using finite element simulations. For more details, see Paper III. (c) Singlet/triplet energy separation (J) as a function of $(2t)^2$.

4.7 Spin transport in the one- and two-electron regimes

When an external B-field is applied, in addition to the Zeeman split of the one-electron states B and AB, the T states Zeeman splits into three separate states (T_+, T_0, T_-). T_+ decreases in energy by two times the Zeeman energy $2|E_z| = \Delta E_z = |g^*|\mu_B B$, where μ_B is the Bohr magneton, and aligns with S when $J_{B=0} = \Delta E_z$ (4.15), assuming a linear energy dependence on the B-field and orbital-independent g^*-factors.

Figure 4.10 shows the B-field dependences of the S and T energy states. These results come from the model employed in Paper IV, using input parameters from both the intermediate ($2t = 2.5$ meV) and strong ($2t = 4.6$ meV) tunnel-coupling regime. At the transition between the singlet and triplet ground state, the states anticross due to the SOI. So far, the S and T states

have been regarded as unperturbed states, although the SOI will mix these states, which is discussed further in Section 4.8. For now, the two-electron ground and excited states are treated as pure S and T states.

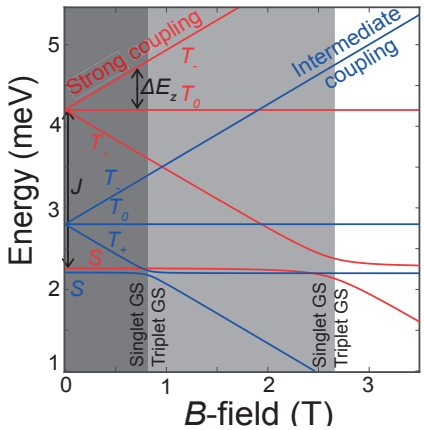

Figure 4.10: Modeled energy diagram of the singlet ($S(1,1)$) and triplet ($T_{0(+,-)}(1,1)$) states as a function of B-field for strong (red) and intermediate (blue) interdot tunnel coupling (t). The gray shaded areas indicate the singlet-ground state region in the two regimes. J is the energy separation of the singlet and triplet states at $B = 0$ T and the triplet states split with the Zeeman-energy splitting (ΔE_z) for finite magnetic fields.

When an external magnetic field is applied, additional conductance lines will show up in the Coulomb stability diagram due to the Zeeman splitting of the one- and two-electron states. All allowed energy transitions between one and two electrons, assuming no SOI or other non-spin conserving processes, are illustrated in Figure 4.11(a). Some of these transitions occur at the same energy difference indicated by same-color arrows in the figure. In a manner similar to that in Figure 4.6, the energies related to the 1-2 electron transitions are translated into electrochemical potentials in Figure 4.11(b). These electrochemical potentials are indicated in the sketched charge stability diagram in Figure 4.11(d). Let us now consider the experimental recorded stability diagram zoomed-in on the the conduction region between $N = 1$ and $N = 2$ blockade diamonds in Figure 4.11(c). The electrochemical potentials associated with the conductance lines are identified by the Roman numerals, where the red color indicates that

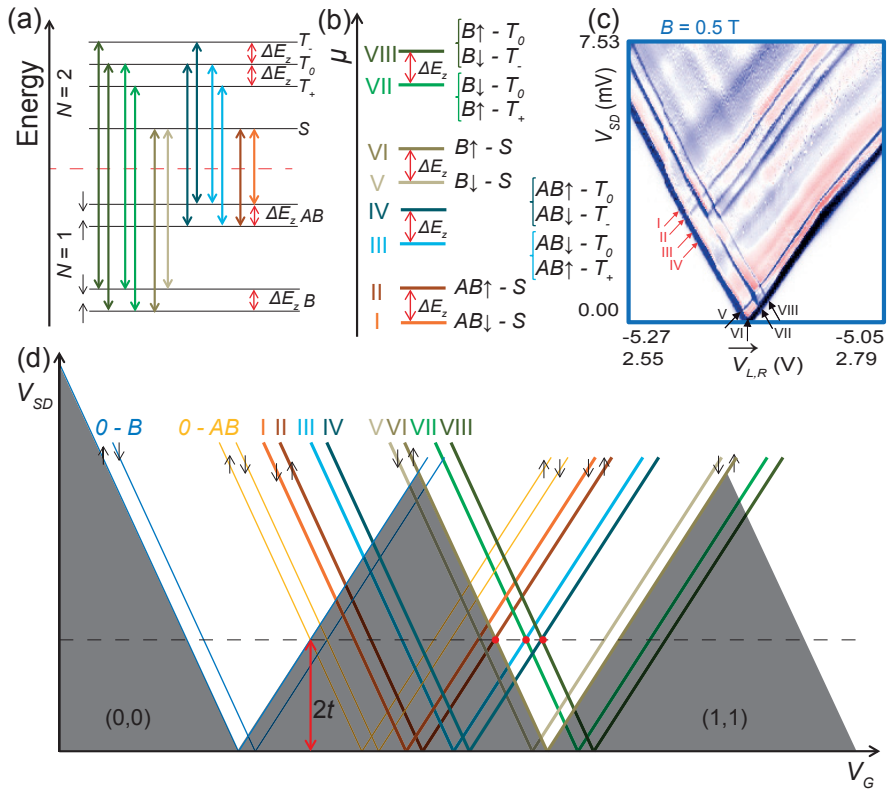

Figure 4.11: (a) Energy levels of one- and two-electron states of the double dot system at a finite external magnetic field. N denotes the total number of electrons in the system. The colored arrows indicate possible energy transitions which are translated into a diagram of electrochemical potential in panel (b). Some transitions are energetically degenerate. The electrochemical potentials are probed in Coulomb charge stability measurements shown in panel (c). This diagram is recorded along the gate-vector connecting the first two triple points, as indicated by the arrows in Figure 4.5. The red and black arrows and Roman numerals highlight conduction lines associated with transitions involving antibonding and bonding states. (d) Schematic Coulomb stability diagram showing the conduction lines associated with the electrochemical potentials in panel (b). Here, the black arrows indicate the spin configuration.

the one-electron state involved in the transition was the antibonding state, whereas the color black indicates that the bonding state was involved in the transition. Here, the Zeeman split is clearly visible and it should be noted that all transitions between one and two electrons predicted in Figure 4.11(b) are resolved. Once again, we note that the transitions starting from the antibondig states going to zero (yellow) are not visible, indicating a fast relaxation from the antibonding to the bonding state.

4.8 Spin-orbit interaction - mixing of singlet and triplet states

As was previously mentioned, when an external magnetic field tunes the S and T_+ states to become energetically aligned, the states anticross. This is due to a mixing of the pure S and T_+ states. Two effects that can couple the singlet and triplet states are the hyperfine interaction and the spin-orbit interaction. The hyperfine interaction arises from the electron spins interacting with the nuclear spins of the host material. The nuclear spins can be partially polarized and give rise to an effective (fluctuating) magnetic field, called the Overhauser field. In a double quantum dot in the two-electron state, the two orbital wave functions have different spatial distributions and interact with slightly different sets of nuclei. This results in a difference in the experienced nuclear field and this difference couples the singlet and triplet states. In the GaAs material system, the hyperfine interaction has been found to be an important contribution to the spin relaxation process [126–128]. In contrast, small hyperfine interaction effects have been reported for InAs serial doubled dots in the strong interdot tunnel-coupling regime [129, 130]. Nadj-Perge *et al.* estimated the characteristic energy scale over which the hyperfine interaction was effective to the order of ~ 0.1 μeV [130], which is considerably smaller than the anticrossing of the singlet and triplet according to the measurements in Paper IV (~ 100 μeV). As a consequence, the hyperfine interaction is from here on omitted in the discussion related to the mixing of singlet and triplet states.

In the case of one-electron states, the SOI only couples states with both different orbitals and spins [16]. In the two-electron case, the singlet and triplet spin states involve different orbital states and are thus directly cou-

pled by the SOI. The pure S and T states hybridize (S and T_0 do not couple to the lowest order due to spin selection rules), and the admixture weakens inversely with the energy difference between the two states [16]. At an intermediate t, where the unperturbed triplet states are well separated around the unperturbed singlet/triplet-transition point, it is reasonable to assume that S and T_+ are the dominating contributions to the new two-electron ground ($GS(1,1)$) and the first excited ($ES(1,1)$) states. In a two-level model the states can be written as

$$GS(1,1) \approx \beta(J)|S\rangle - \gamma(J)|T_+\rangle \tag{4.16}$$

and

$$ES(1,1) \approx \gamma(J)|S\rangle + \beta(J)|T_+\rangle. \tag{4.17}$$

Here, $\beta(J)$ and $\gamma(J)$ are $J(B)$ dependent weight functions. At the unperturbed singlet/triplet ground state transition point, the S and T_+ states reach maximum mixing, resulting in an anticrossing magnitude of Δ^*_{ST}.

Figures 4.12(a)-(c) show experimental results of the magnetic field evolution of the transitions involving the S and T states. The measurements are recorded at the constant gate configuration indicated by the dashed line in Figure 4.12(d). By tuning the gates and, thus the tunnel coupling, the magnitude of the anticrossing is tuned. Gate-tuning of the spin-orbit coupling has been reported for an unknown electron population in self-assembled single InAs quantum dots [98]. However, the results presentes in Paper IV demonstrate an almost twofold increase in tuning range (~ 200 μeV) of Δ^*_{ST}. Extracted values of Δ^*_{ST} as a function of the interdot tunnel coupling are shown in Figure 4.12(e). As indicated in Figure 4.12(f), the increase in t was here obtained by either making the back-gate more negative, effectively pushing the wave function up to the top part of the nanowire-cross section (blue trace), or making it more positive, pulling the wave functions downwards (red trace).

Now, let us consider the possible energy transitions between the one- to two-electron states at a magnetic field where the system is tuned to the crossing point of the unperturbed singlet/triplet. Figure 4.13(a) shows the energy diagram where the transitions previously involving the unperturbed S and T_+ states are now modified by the SOI coupling, forming the $GS(1,1)$ and $ES(1,1)$. This is a simple correction to Figure 4.11(a) where any other mixing

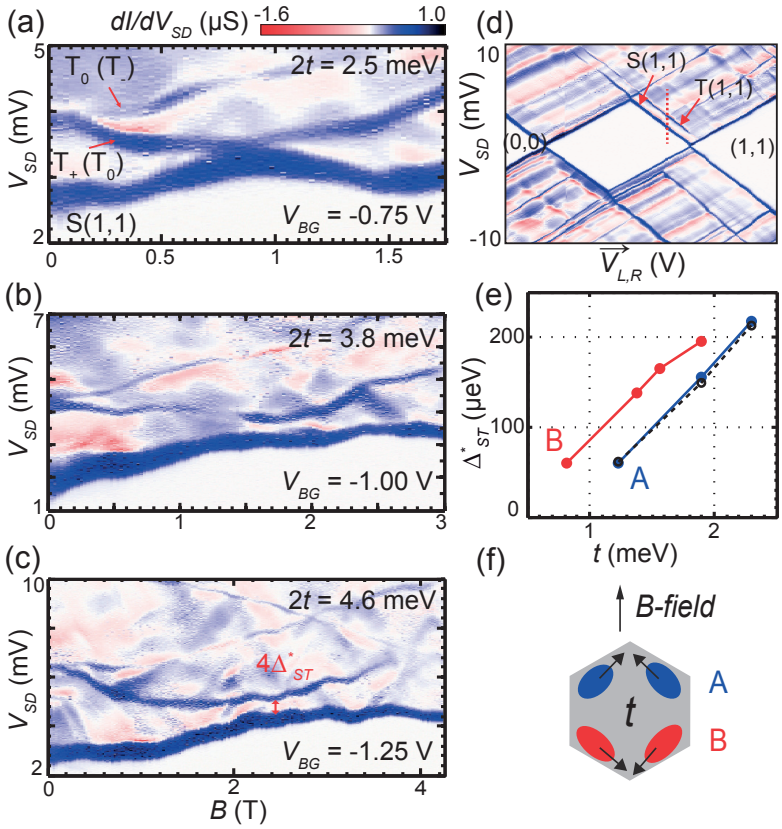

Figure 4.12: (a)-(c) Differential conductance (dI/DV_{SD}) as a function of source-drain bias (V_{SD}) and magnetic field (B), recorded at different constant gate settings indicated by the dashed line in the Coulomb stability diagram zoomed-in around the (0,0) to (1,1) electron population in panel (d). In (a), the two-electron states involved in the transitions corresponding to the different conductance lines are indicated. (e) Extracted singlet/triplet anticrossing (Δ^*_{ST}) as a function of interdot tunnel coupling (t). Trace A and B correspond to the tuning of t by either going to more negative or more positive back-gate potential, as illustrated in panel (f). The black trace is model values; for details see Paper IV.

of the states is neglected. As a consequence of including the effect of SOI to the energy diagram, the electrochemical potentials in Figure 4.13(b) also becomes modified. These modifications are translated into the sketched charge stability diagram in Figure 4.14. In the experimental data shown in Figure 4.13(c), we can discern a pairing of conductance lines, previously associated with transitions involving S and T_+ states, with an energy separation of $2\Delta^*_{ST}$. The conductance lines involving the $GS(1,1)$ and $ES(1,1)$ states are in Figure 4.13(c) marked by the one-electron state involved in the transition. All transitions predicted by the simple model in Figure 4.13(b) are visible in the experimental measurements in Figure 4.13(c), except for $B \downarrow -T_0$ and $AB \downarrow -T_0$. These excited-excited state transitions are however visible in the modeling, see Paper IV.

When continuing to increase the magnetic field, moving away from the maximum mixing point, the pairing of conductance lines involving the hybridized states persists in the experimental data shown in Figure 4.13(d). Here, some of the conductance lines are weak but nevertheless visible. In the case of the transitions involving $B \downarrow$, two strong conductance lines are visible affirming the presence of non-spin conservation and indicating that SOI still contributes to a significant hybridization of the S and T_+ states.

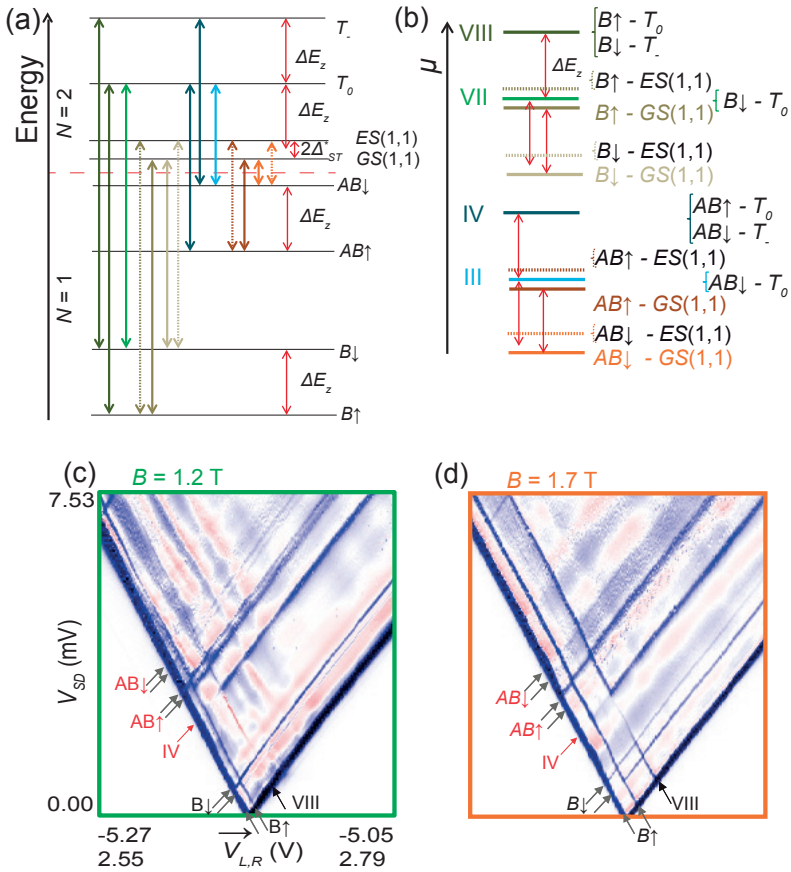

Figure 4.13: (a) Energy levels of one- and two-electron states of the double dot system at external magnetic field aligning the unperturbed S and T_+ states. N denotes the total electron number in the system. The bonding (B) and antibonding (AB), and the triplet (T) states are split by the Zeeman-energy splitting (ΔE_z). $GS(1,1)$ and $ES(1,1)$ are the ground and excited two-electron states, resulting from the spin-orbit coupling parametrized by Δ^*_{ST}. The color-coded arrows indicate possible energy transitions which are translated into a diagram of electrochemical potential in panel (b). (c) and (d) Coulomb charge stability diagrams recorded along the gate-vector connecting the first two triple points, as indicated by the arrows in Figure 4.5, zoomed-in on the region between the one- and two-electron blockade diamonds. Here, the conductance lines corresponding to transitions involving the $GS(1,1)$ and $ES(1,1)$ are indicated by the one-electron states involved in the transitions, and transitions involving unperturbed states are noted by the corresponding Roman numeral. (c) is recorded at a magnetic field where the unperturbed S and T_+ states are aligned and (d) is recoded at larger B-field.

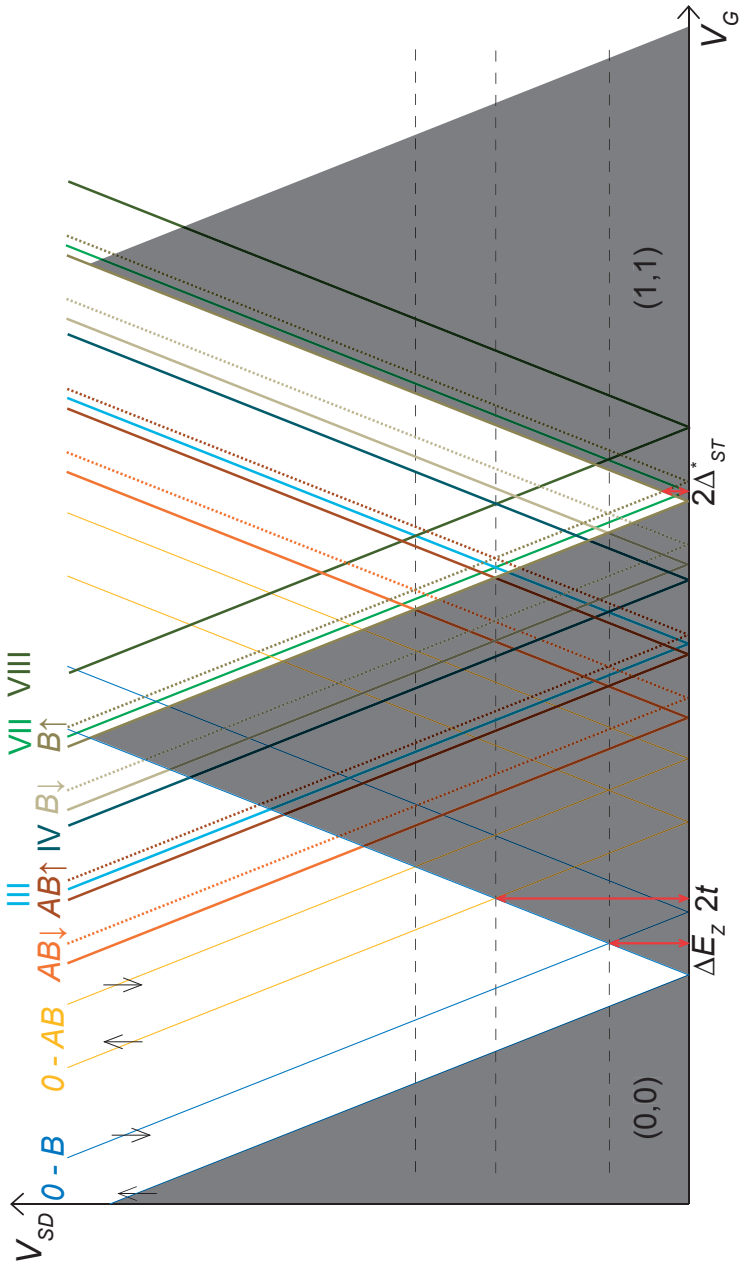

Figure 4.14: Schematic Coulomb stability diagram showing the conduction lines associated with the electrochemical potentials in Figure 4.13(b). The notation of states and energies, and the color-coding follows the one used in Figure 4.13; the black arrows indicate the spin configuration of the one-electron state.

Chapter 5

InAs/GaSb core-shell devices

This chapter serves to introduce Paper II and provides a short overview of the InAs/GaSb heterostructure, covering transport properties of two-, one- and zero-dimensional devices. Furthermore, the development of the InAs/GaSb core-shell quantum dot, starting from core-shell nanowires, is discussed.

5.1 InAs/GaSb heterostructures

InAs ($m_e^* = 0.023\ m_0$)* and GaSb ($m_h^* = 0.40\ m_0$) have some of the lowest electron and hole effective masses, respectively, among the III-V semiconductor compounds. This leads to high mobilities and large quantization effects, especially in InAs. Even more importantly, as a heterostructure in bulk, InAs/GaSb form the uncommon type-II broken-gap band alignment, where the conduction-band edge (E_{CB}) in InAs is located approximately 150 meV below the valence band-edge (E_{VB}) in GaSb [131], see Figure 5.1(a). In addition, the two materials are nearly lattice matched, with a lattice constant of approximately 6.1 Å, leading to negligible strain at the heterostructure interface. At equilibrium, charge transfer of electrons from the GaSb valence band to the InAs conduction band has taken place, and spatially separated electrons and holes coexist at the interface, see Figure 5.1(b). For a topical review on the material system, see [132].

*The values are given at 300 K.

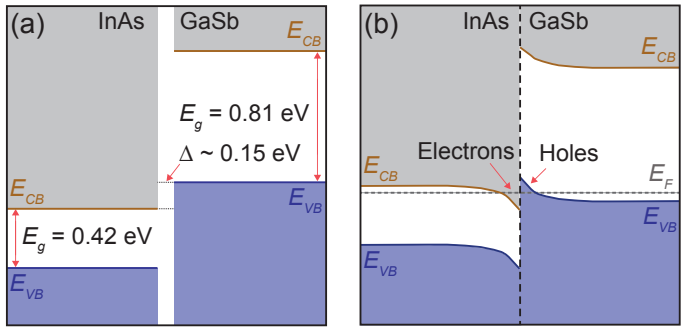

Figure 5.1: (a) Schematic band diagram of the InAs and GaSb heterostructure interface in bulk, where the band gap (E_g) and the overlap (Δ) of the GaSb valence band and the InAs conduction band are indicated [133]. (b) Band-edge alignment at equilibrium.

5.2 Low-dimensional InAs/GaSb heterostructures

The overlap between the InAs conduction band and the GaSb valence band can be tuned by decreasing the size of the heterostructure system, hence increasing quantum confinement. Figure 5.2(a) shows a schematic of the one-dimensional band dispersion of an InAs/GaSb heterostructure with small quantum confinement. Here, only a single electron 1D subband (E_1) in InAs and a single hole 1D subband (H_1) in GaSb are shown. In line with the previous discussion, the lowest conduction band state (E_1) in InAs lies below the highest valence band state (H_1) in GaSb. In bulk, the energy of E_1 and H_1 would correspond to E_{CB} in InAs and E_{VB} in GaSb, respectively. This results in an inverted band structure with a negative effective band gap (ΔE), and such systems are called semimetals. Depending on the strength of the coupling between the 1D states, hybridized states, consisting of conduction band states in InAs and valence band states in GaSb, will appear, see Figure 5.2(a). Due to the hybridization, a so-called "hybridization gap" emerges in the band dispersion. The magnitude (Δ) of this gap depends on the overlap and the relative contribution of conduction and valence band states. In the InAs/GaSb quantum well system, these parameters can partly be tuned by electrostatic gating. If the quantum confinement is increased, the states will shift and at some point a positive band gap will appear, see Figure 5.2(c).

Esaki *et al.* were pioneers in studying the electronic properties of super

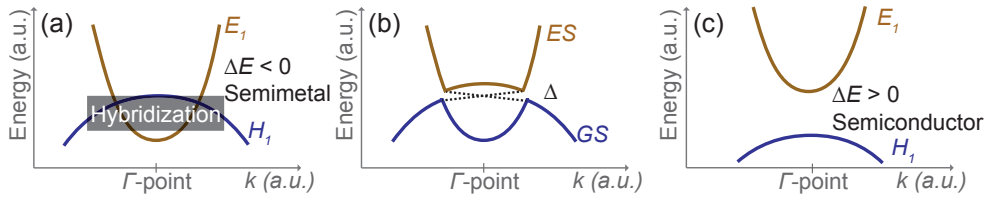

Figure 5.2: Schematic illustrations of band dispersion of an InAs/GaSb nanowire heterostructure. Only a single InAs conduction subband (E_1) and a single GaSb valence subband (H_1) are shown. (a) Small radial quantum confinement leading to overlap (negative band gap (ΔE)) and hybridization of the subbands. (b) Hybridization of the E_1 and H_1, results in a new ground sates (GS), excited states (ES) and a hybridization gap of magnitude Δ. The dashed lines indicate the dispersion of edge states that might appear in the system. (c) Strong quantum confinement leading to a positive band gap (ΔE).

lattices of InAs/GaSb heterostructures [131], and the transition between the semimetallic and semiconducting phase has been both theoretically predicted and experimentally studied in two dimensional InAs/GaSb systems [134–136].

One major reason for the recent interest in the InAs/GaSb two-dimensional system is the predicted so-called topologically protected edge states [137]. These topological edge states, combined with induced superconductivity, can host exotic Majorana fermion modes which can be used for topological quantum computation [138], or the edge states can be employed to realize dissipationless transistors for quantum computers based on the quantum spin Hall effect. According to theory, these states appear at the edge of the InAs/GaSb interface in the "hybridization gap" that opens up in the energy dispersion of the hybridized states at a certain geometrical dimension of the wells and at the right tuning of the gate potential [139]. The topologically protected states are robust against perturbations like scattering. However, although claims of experimental evidence of topological insulating states and topological edge states have been reported [140–143], the most recent publications explain their findings by trivial (non-topological) phase edge transport [144, 145].

In quasi-one-dimensional core-shell InAs/GaSb nanowires, the bandstructure of core-shell nanowires has been modeled [146] and the effects of the band overlap and hybridization on the electronic structure of [001]-oriented [147] and [111]-oriented [148, 149] InAs/GaSb core-shell nanowires have been

theoretically studied. Also, the impact of the relative core radius and shell thickness has been theoretically investigated. Here, it should be noted that according to symmetry arguments the one-dimensional system is not predicted to host topologically protected states [150]. However, the possibility for topologically protected states in the quasi-one-dimensional core-shell nanowires is not fully explored [151].

InAs/GaSb nanowire heterostructures have been grown with both axial [152] and radial (GaSb/InAsSb) [153] (InAs/GaSb) [26, 154] material transitions. Also, the electronic properties, such as ambipolar transport, of core-shell InAs/GaSb [26] and GaSb/InAs [153, 155, 156] have been experimentally investigated. In a device perspective, the overlapping conduction band and valence band make the material system suitable for realizing tunnel field-effect transistors [157, 158].

Electron-hole interactions in quasi-zero-dimensional zinc blende GaSb/InAs core-shell systems have been studied [25]. Here, the quantum dots were formed between the tunnel barriers at the source and drain contacts. The electrical properties of the system were found to be highly dependent on the radial and axial geometry, and the tunnel coupling to the source and drain. Unfortunately, tuning the radius of GaSb nanowires, without losing the pure crystal phase, is challenging which limits the possibilities of tailoring the electrical properties. It is also challenging to control the tunnel coupling to the source and drain contacts. In Paper II, we utilized the selective shell growth demonstrated by Namazi *et al.* in Ref. [26] to form InAs/GaSb core-shell quantum dots during epitaxial growth. This method provided greater control of the electrical properties which could open the door to experimental studies of excitonic ground states theoretically predicted in quantum dot in similar material systems [159]. The development leading to the devices presented in Paper II are described in more detail in the following sections.

5.3 Electrical characterization of InAs/GaSb core-shell nanowires

As a step towards realizing InAs/GaSb core-shell quantum dots, we studied electron-hole transport in InAs/GaSb core-shell nanowires. The relative contribution to transport of the electrons in the core and the holes in the

shell was very sensitive to the nanowire diameter and the GaSb shell thickness. Hence, the geometrical properties had to be tuned with high precision to obtain the desired electrical characteristics. Figure 5.3(a) displays an SEM image of a typical device with a top-gate configuration. The results of the electrical characterization of three types of devices, at 295 K and 4.2 K, are shown in Figures 5.3(b) and (c), respectively. The green trace corresponds to a pure InAs device, which owing to surface donor states, had an n-type conduction profile [123], and thus became depleted at negative V_g, as expected. In contrast, the core-shell InAs/GaSb device (black trace) showed ambipolar transport characteristics. At 4.2 K, an up-turn in conductance was seen at negative V_g, attributed to an onset of hole transport in the GaSb shell. This is consistent with the typically p-type behavior of nominally undoped GaSb [160]. The decrease in conductance at positive V_g compared with the bare InAs nanowire could be due to surface states in the GaSb and lower carrier injection to the InAs core via the shell. In addition, Figures 5.3(b) and (c) show results from a third device consisting of an InAs core, GaSb shell and a second thin ($\sim$ 2 nm) InAs shell (blue trace). The quantum confinement was

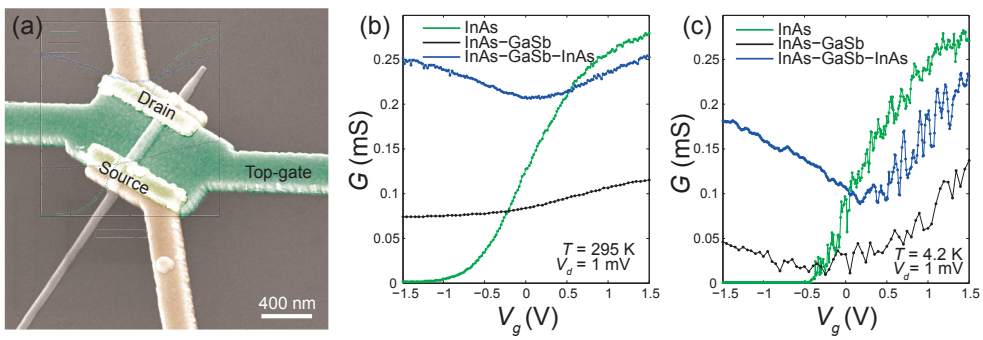

Figure 5.3: (a) SEM image (false color, 30° tilt) of a core-shell nanowire device with a top-gate (green) contact configuration and approximately 420 nm distance between the source and drain contacts (yellow). (b) and (c) Conductance (G) as a function of the gate voltage (V_g) at 295 K and 4.2 K, respectively, recorded for three different nanowire devices with the contact configuration shown in (a); pure InAs $D \approx 48$ nm (green), InAs core with GaSb shell $D \approx 58$ nm (black) and InAs/GaSb core-shell structure with a thin passivating InAs shell $D \approx 66$ nm (blue). Here, D denotes the total diameter of the nanowire. The GaSb shell thickness, extracted from TEM images of typical devices, was approximately 8-9 nm.

very strong in this outer InAs shell, leading to a depletion of electrons and thus no contribution to transport. However, the shell acted as a passivating layer, protecting the GaSb from surface oxidation and modulating the Fermi level pinning at the GaSb surface, which led to an improved hole mobility. In addition, the resulting accumulation of holes at the GaSb surface improved the carrier injection at the contacts [161] and increased the conductance at both negative and positive V_g. The observed passivation effect was consistent with previous findings for the GaSb/InAs system [153, 155].

5.4 InAs/GaSb core-shell quantum dots

Quantum dots formed by wurtzite segments in zinc blende InAs nanowires were used as a starting point to realize InAs/GaSb core-shell quantum dots during epitaxial growth. As demonstrated in Ref. [26], radial growth of GaSb on wurtzite InAs can be suppressed due to the lower surface energy of wurtzite compared to zinc blende. Thus, InAs nanowires can act as a template for selective overgrowth of GaSb to obtain coupled parallel quantum dots, with built-in leads, by self-assembly with high-precision design. Here, the wurtzite segments have two roles: first, as tunnel barriers to define the electron quantum dot in the InAs core; second, to suppress radial growth and thus define the shell hole quantum dot. Figure 5.4(a) shows a sketch of the quantum dot nanowire design. A simple version of the alignment of the InAs conduction band (E_{CB}) and GaSb valence band (E_{VB}) together with the Fermi level (E_F) is illustrated in Figure 5.4(b). Figure 5.4(c) shows an SEM image of one of the first-generation core-shell quantum dot devices studied, without a passivating InAs shell. The suppression of the GaSb shell growth on the wurtzite InAs segment is clearly visible in the TEM image of a nanowire hosting such a quantum dot, shown in Figure 5.4(d). The electrical characterization of these devices (not shown here) provides evidence of single electron transport; however, the hole transport was weak which was attributed to a poor GaSb surface.

5.4.1 Electrical characterization of core-shell quantum dots

For the second generation of devices, a thin ($\sim 1-3$ nm) passivating InAs shell was added to improve the hole transport. The next step was to fine-tune

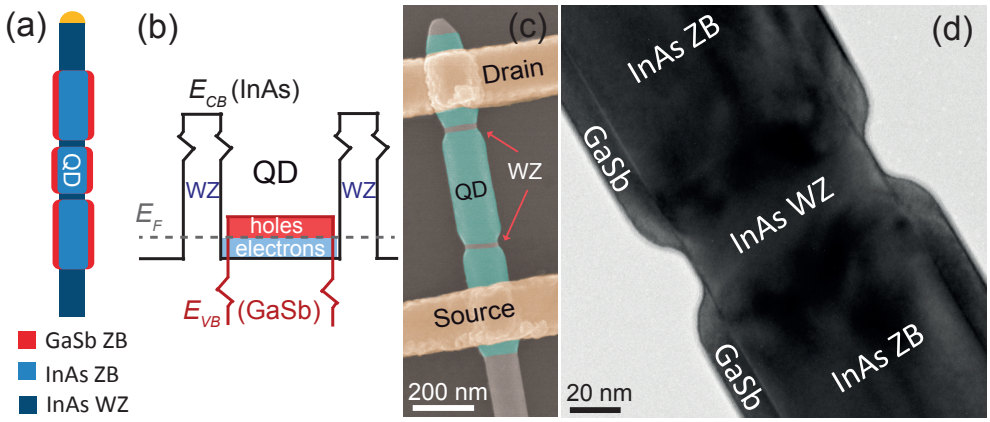

Figure 5.4: (a) Sketch of the core-shell quantum dot nanowire design, consisting of three zinc blende segments in an otherwise wurtzite nanowire. (b) Sketch of the InAs conduction band (E_{CB}), GaSb valence band (E_{VB}) and Fermi level (E_F) alignment in the core-shell quantum dots. (c) SEM image (false color) of a typical first-generation core-shell InAs/GaSb zinc blende quantum dot defined by wurtzite segments, connected to source and drain contacts (yellow). The zinc blende segments of the nanowire are highlighted in green. The quantum dot length and diameter were approximately 355 nm and 140 nm, respectively and the wurtzite barrier lengths were 15-20 nm. (d) Bright field TEM image of a wurtzite segment in an otherwise zinc blende core-shell nanowire (imaged along the [112] zone axis). TEM image by Sebastian Lehmann.

the geometrical dimension of the nanowire. Figure 5.5(a) shows the gate response for two devices with different relative dimensions of core diameter and shell thickness, and wurtzite section lengths. Both devices showed ambipolar transport characteristics. However, in the case of Device 2, the ambipolarity was not as pronounced, and the transition point between p-type and n-type conductance is shifted towards $V_g \approx 7$ V, indicating that hole transport dominated. By tuning the relative dimensions of the core diameter and the shell thickness, symmetric ambipolar transport was obtained, as can be seen for Device 3 (the device displayed in Figure 4 in Paper II). In addition, at the transition point between n-type and p-type conductance, a decrease in conductance on the order of two magnitudes was seen for Device 3 as compared to Device 2. This decrease can, in addition to the change in radial composition, be attributed to the longer wurtzite barriers. The comparably higher

Table 5.1: Diameters and lengths of the quantum dot (QD) segments, wurtzite (WZ) barrier lengths and shell thicknesses for three devices with passivating InAs shell. The parameters for Device 2 and the shell thicknesses stated for Devices 3 and 4 were extracted from TEM images of typical devices from the same growth batch.

Device	Diameter (nm)	QD length (nm)	WZ barrier length (nm)	GaSb/InAs shell thickness (nm)
2	∼90	∼140	10-20	unknown
3	90	37	36	∼3-5/1-3
4	76	73	29	∼3-5/1-3

conductance at larger positive V_g for Device 3 could be explained by stronger gate-coupling due to a thinner GaSb shell.

Figure 5.5(b) presents the gate capacitance (C_g) extracted from Coulomb blockade of electrons as a function of quantum dot length for the devices discussed here. The quantum dot device without an InAs passivating shell is denoted 1, whereas the devices discussed in the previous paragraph are denoted 2 and 3. The data point denoted 4 is from a device presented in Figure 5.6(b). A linear scaling of the C_g with the quantum dot length could be observed, in agreement with what we reported in Paper I and what is shown in Figure 3.4, again showing that the wurtzite segments effectively defined the quantum dot. It should be noted that factors beside the than quantum dot length, such as the thickness of the GaSb(InAs) shell, affected the gate capacitance. However, the linear trend in Figure 5.5(b) surely affirmed that the electron quantum dot was formed between the wurtzite barriers. Table 5.1 shows an overview of the geometry of the three devices with an InAs shell discussed in this chapter.

Figure 5.6(a) shows a charge stability diagram recorded for Device 2 [Figure 5.5(a)] in the gate voltage region where the p-branch and n-branch meet. In this region we expect electrons and holes to coexist in the two dots. A pattern of regular smaller diamonds attributed to the Coulomb blockade in the electron transport in the core, modulated by a larger pattern attributed to the Coulomb blockade in the hole transport in the shell, was observed. This is a typical sign of transport via parallel-coupled quantum dots with a pronounced

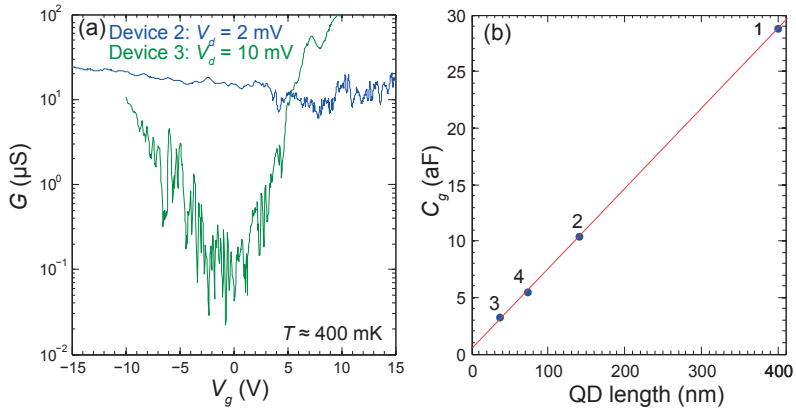

Figure 5.5: (a) Conductance (G) as a function of gate voltage (V_g) for quantum dot devices with passivating InAs shells from two different growth batches (different growth parameters and growth equipment). The length of the wurtzite segments and quantum dot differed in the two cases. Device 2 had shorter wurtzite (10-20 nm) and longer quantum dot (∼140 nm) segments. Device 3 had longer wurtzite (36 nm) and shorter quantum dot (37 nm) segments. The total diameter of the nanowires was approximately 90 nm. (b) Gate capacitance (C_g) as a function of the length of the quantum dot segment for the four core-shell quantum dot devices discussed here. The quantum dot lengths used for Devices 1 and 2 were averages extracted from TEM imaging of nanowires from the same growth batch, whereas the quantum dot lengths for Devices 3 and 4 were extracted from SEM images of the electrically characterized devices. The red line is a linear fit to the data points.

size difference. In the gate voltage range of 7.75 V - 8.85 V, a C_g of approximately 10 aF could be extracted from the smaller diamonds. This value was approximately a third of the C_g extracted for the first-generation quantum dot, which was consistent with the decrease in quantum dot length by a factor of three, see Figure 5.5(b). In order to see a more well-defined Coulomb blockade pattern, an increase in tunnel barrier resistance was needed. This resistance increase was obtained by increasing the wurtzite-segment lengths as was done for the nanowire devices presented in Paper III.

Figure 5.6(b) displays a charge stability diagram recorded in the region where the n- and p-branches meet for a device from the same growth batch as Device 3 in Figure 5.5(a). This device is referred to as Device 4 and was also discussed in Figure 3 of Paper III. A beating pattern of smaller diamonds (electron blockade) and larger diamonds (hole blockade) was clearly

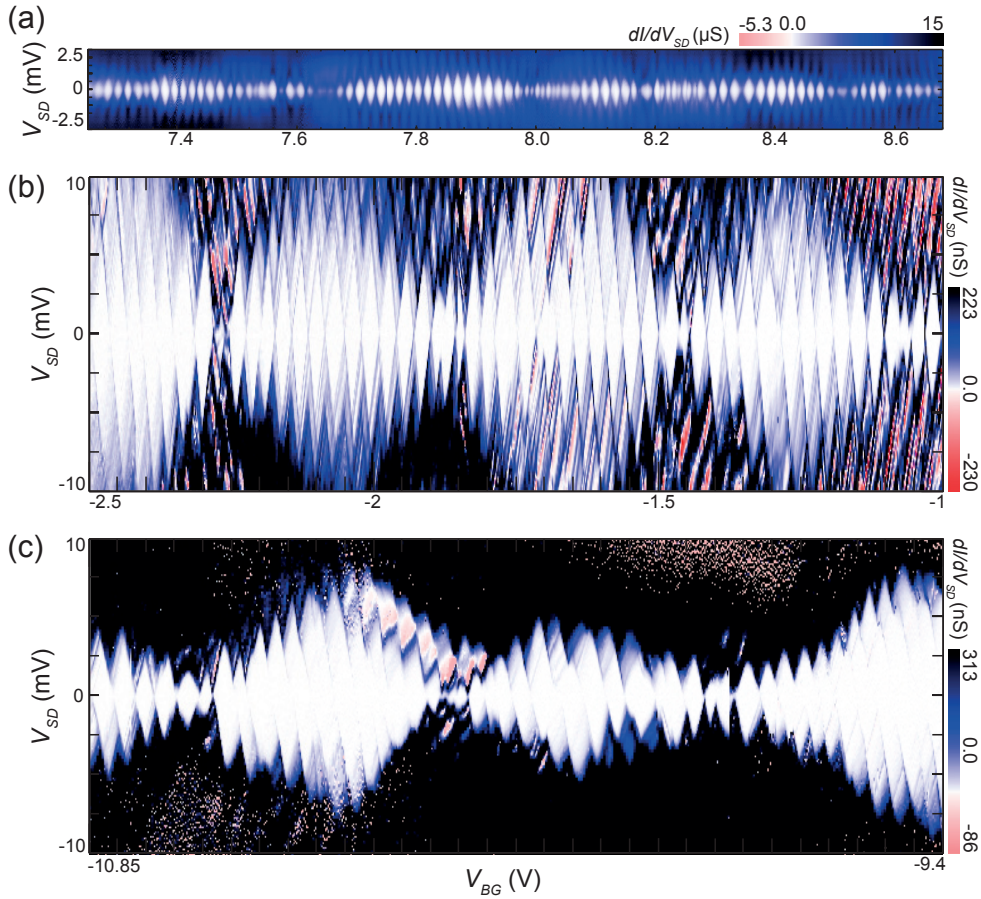

Figure 5.6: Charge stability diagram recorded for (a) Device 2 and (b) Device 4 at the transition point between the n-branch and p-branch at an electron temperature of approximately 400 mK. (c) Recording for Device 4 at more negative gate potentials.

visible. Here, we observed that a higher tunneling resistance led to a more well-defined Coulomb blockade pattern as opposed to in Figure 5.6(a). From electron diamonds at positive V_g, $C_g = 5.5$ aF was extracted, which again was consistent with the decrease in quantum dot length, see data point 4 in Figure 5.5(b). The beating pattern persisted even at more negative gate potential, as seen in Figure 5.6(c). Although reference devices comprising of bare InAs quantum dots with similar dimensions are difficult to fully deplete, the current levels typically reached very low values at V_g between -3 V and -7 V. Thus, from Figure 5.6(c), it is evident that the holes in the shell screened the gate, leading to a shift in the depletion point of the core quantum dot.

Figure 5.7(a) displays a charge stability diagram zoomed-in on a region where the Coulomb hole blockade was lifted, recorded for Device 3. The electron and hole population in the blockade regimes are indicated in black and red, respectively. Reading the image from the left to right, a shift in the hole conduction line, where the hole population alternated between $h+1$ and h (red dashed line), occurred when the electron population changed from $e-1$ to e. This shift was due to an attractive electrostatic interaction between spatially separated electrons and holes; the addition of an electron to the core quantum dot increased the change in chemical potential needed to remove a hole from the shell quantum dot. From the shift, we can extract an upper estimation of the electron-hole electrostatic interaction strength $\Delta_{e-h} \approx 4.5$ meV. Here, symmetric capacitive coupling to the source and drain was assumed. Figure 5.7(b) shows schematic illustrations of the electrochemical potential alignment for hole transport in the system at the two different electron populations in the core quantum dot. The red solid and dashed lines represent the hole transport channel at $e-1$ and e electrons on the core quantum dot, respectively.

By using the capacitance and resistance model of the parallel quantum dot system shown in Figure 5.7(d), key features of the transport behavior can be reproduced, see Figure 5.7(c). Here, the model consists of a metallic quantum dot interacting with a quantum dot that has only a single level. Although transport via excited states and effects such as the energy-dependent density of states in the leads (seen in the experimental results) are not captured in the simulation, the relatively simple model manages to reproduce features involving ground state transport in good agreement with the experimental results.

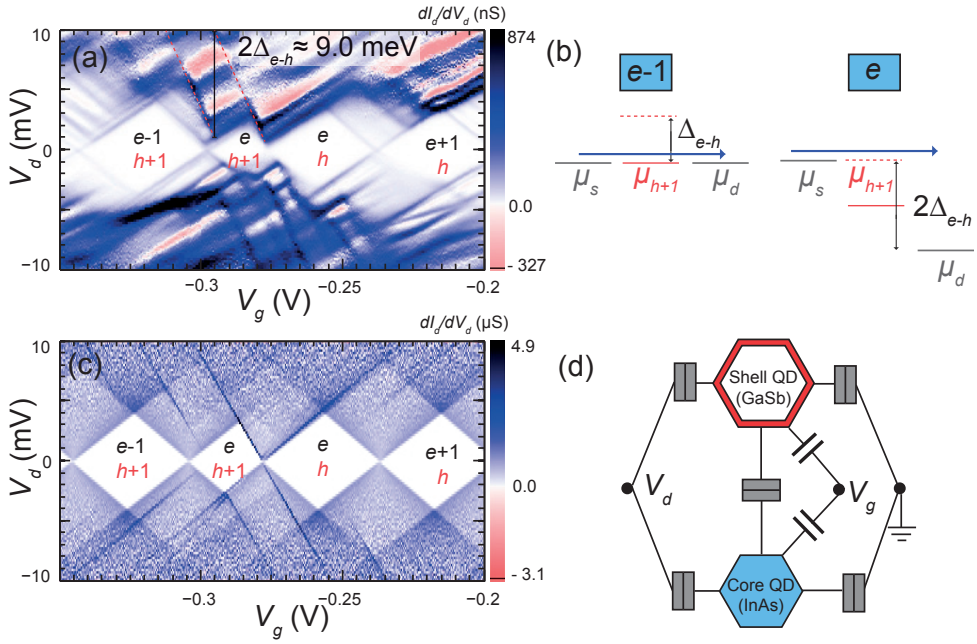

Figure 5.7: (a) Charge stability diagram experimentally recorded for Device 3 in a V_g interval where the hole blockade was lifted. The electron and hole population are marked in black and red, respectively. An upper bound of the electron-hole interaction strength $\Delta_{e-h} \approx 4.5$ meV was extracted. (b) Schematic illustration of the electrochemical potential alignment for hole transport at an electron population of $e-1$ and e on the core quantum dot, respectively. (c) Simulated charge stability diagram by means of a capacitance and resistance model of the system shown in (d).

Comparing the features in Figure 5.6(a) and (b), such as the smaller diamonds (weaker quantization effect) and the less defined hole transport in Figure 5.6(b), it is clear that the electrical properties are strongly dependent on the geometrical dimensions of the system. This calls for a precise tuning of dimensions during the growth. It should be noted that all types of core-shell nanowires presented in this thesis were grown using aerosol gold seed particles, limiting the control of the geometrical dimensions of individual nanowires. In order to improve the possibility for studies on electron-hole interactions of single orbitals, the *n*- and *p*-branches need to be further separated. This is achieved by increasing the quantum confinement and, possibly the length of the wurtzite segments. A concern here is whether the mechanism of the

shell growth will limit the possibility of quantum dot size reduction while maintaining a sufficient shell thickness, since the radial growth rate decreases when the InAs quantum dot size is reduced. However, preliminary growth results using EBL-defined arrays of seed particles show predominantly *p*-type electrical characteristics, indicating the possibility of obtaining sufficient shell thicknesses.

Chapter 6

Conclusions and outlook

This thesis has demonstrated the formation of robust electron quantum dots in zinc blende InAs nanowires by means of closely spaced wurtzite segments. A lower bound of the height of the tunnel barriers was estimated to 95 meV. Furthermore, the dimensions of the quantum dots and hence the electrical properties could be tuned during the nanowire growth process to obtain fully depletable quantum dots. By employing a set of three gates we could split the few-electron single quantum dots into two parallel-coupled quantum dots.

The combination of hard-wall potential barriers to the source and drain and the sets of gates together with the InAs surface properties and its strong spin-orbit interaction gave rise to a system with highly tunable charge and spin states.

We expect the surface properties of InAs to have a key role in the formation of the parallel-coupled quantum dots. Yet, the relative impact of the nanowire "bulk" properties and the surface characteristics on the electron transport in the single quantum dot is not completely clear. We saw signs of increased electron concentration in the electrical characteristics of devices where sulphur passivation of the nanowire surface was performed during the contact-fabrication process. To some extent, the increased electron concentration washed out the single-electron transport. We attributed this increase to the sulphur solution seeping in under the resist, affecting the surface of the nanowire away from the contact regions. A means to investigate the effect of surface states would be to perform in-situ studies of the transport properties before and after cleaning of the surface with atomic hydrogen. Although the

parallel-coupled double dot formation was repeatable and seen in several devices, the tuning range of the interdot tunnel coupling varied between devices and also between subsequent cooling cycles of the same device. Here, a treatment resulting in increased control of the surface properties would be highly desirable.

The thesis also presents initial magnetotransport studies on the single quantum dot. Here, an anisotropy in the SOI was reflected in the dependence of the $|g^*|$-factor on the magnetic-field direction. However, a microscopic model is needed to fully understand the influence of the different crystal phases and asymmetric confining potential on the SOI. In addition, aligning the nanowire quantum dot with a strong external magnetic field, could provide a system suitable for studies of the Paschen-Back effect.

Furthermore, the double dot system was studied in the region of transitions changing the electron population from (0,0) to (1,1). The next step is naturally to investigate asymmetric transitions such as (2,0) to (1,1), with particular relevance for spin-based qubits.

We believe that this system of parallel-coupled quantum dots is ideal for fundamental studies of many-body correlated transport, such as the spin-Kondo effect and Cooper-pair splitting. To probe Kondo physics, a strong tunnel coupling to the source and drain is necessary. Instead of modulating the tunnel coupling by tuning the length of the wurtzite segments during the nanowire growth, additional side-gates could be employed to obtain electrically tunable tunnel couplings.

Going back to the last part of the thesis, by using InAs electron quantum dots as a template, core-shell electron-hole quantum dots were realized utilizing suppression of GaSb radial growth on segments with a wurtzite crystal phase. In such parallel electron-hole quantum dots, a clear beating pattern of Coulomb blockade diamonds associated with electron and hole transport was demonstrated. We also saw signs of electrostatic interactions between electrons and holes, and extracted an upper limit of the electron-hole interaction strength of approximately 4.5 meV.

By increasing the quantum confinement of the core-shell electron-hole quantum dots, the energy separation between states will increase, which might allow for studies of hybridization of specific electron and hole energy levels. Preliminary results indicate that it is indeed possible to grow GaSb shells on the thin disc-shaped zinc blende segments needed to reach the few electron

regime in the bare InAs single quantum dot. The next step is to tune the InAs quantum dot length and relative shell thickness to reach the few electron/hole regime. Here, side-gates can be employed to increase the control of overlap of the electron and hole wave functions.

In addition, superconducting contacts on InAs/GaSb core-shell nanowire structures could allow studies of Cooper pairs coupling to hybrid electron and hole states. Also, normal contacts on designed core-shell nanowires could open up for studies of coupled excitonic ground states.

Finally, the level of control in the fabrication of the crystal-phase-based quantum dots and the quality of the electrical properties demonstrated in this thesis, in combination with a variety of ideas for future experiments, highlights the great potential of using atomically precise crystal-phase designs of nanowires to access and probe fundamental quantum physics.

Bibliography

[1] J. P. Dowling and G. J. Milburn, "Quantum technology: The second quantum revolution," *arXiv*, arXiv:quant–ph/0206091, 2002.

[2] M. H. Devoret, A. Wallraff, and J. M. Martinis, "Superconducting qubits: A short review," *arXiv*, arXiv:cond–mat/0411174, 2004.

[3] J. M. Gambetta, J. M. Chow, and M. Steffen, "Building logical qubits in a superconducting quantum computing system," *npj Quantum Information*, vol. 3, 1 2017.

[4] D. Loss and D. P. DiVincenzo, "Quantum computation with quantum dots," *Phys. Rev. A*, vol. 57, pp. 120–126, 1 1998.

[5] B. Trauzettel, D. V. Bulaev, D. Loss, and G. Burkard, "Spin qubits in graphene quantum dots," *Nature Physics*, vol. 3, p. 192, 2007.

[6] C. Kloeffel and D. Loss, "Prospects for spin-based quantum computing in quantum dots," *Annual Review of Condensed Matter Physics*, vol. 4, no. 1, p. 51, 2013.

[7] S. M. Frolov, S. R. Plissard, S. Nadj-Perge, L. P. Kouwenhoven, and E. P. Bakkers, "Quantum computing based on semiconductor nanowires," *MRS Bulletin*, vol. 38, no. 10, 809–815, 2013.

[8] M. Russ and G. Burkard, "Three-electron spin qubits," *Journal of Physics: Condensed Matter*, vol. 29, no. 39, p. 393 001, 2017.

[9] D. Aasen, M. Hell, R. V. Mishmash, A. Higginbotham, J. Danon, M. Leijnse, T. S. Jespersen, J. A. Folk, C. M. Marcus, K. Flensberg, and J. Alicea, "Milestones toward Majorana-based quantum computing," *Phys. Rev. X*, vol. 6, p. 031 016, 3 2016.

[10] M. A. Reed, "Quantum dots," *Scientific American*, vol. 268, p. 118, 1993.

[11] A. J. Shields, "Semiconductor quantum light sources," *Nature Photonics*, vol. 1, p. 215, 2007.

[12] T.-H. Kim, K.-S. Cho, E. K. Lee, S. Lee, J. Chae, J. W. Kim, D. H. Kim, J.-Y. Kwon, G. Amaratunga, S. Y. Lee, B. L. Choi, Y. Kuk, J. M. Kim, and K. Kim, "Full-colour quantum dot displays fabricated by transfer printing," *Nature Photonics*, vol. 5, p. 176, 2011.

[13] M. A. Kastner, "The single-electron transistor," *Rev. Mod. Phys.*, vol. 64, p. 849, 3 1992.

[14] U. Resch-Genger, M. Grabolle, S. Cavaliere-Jaricot, R. Nitschke, and T N, "Quantum dots versus organic dyes as fluorescent labels," *Nature Methods*, vol. 5, p. 763, 2008.

[15] K. C. Nowack, F. H. L. Koppens, Y. V. Nazarov, and L. M. K. Vandersypen, "Coherent control of a single electron spin with electric fields," *Science*, vol. 318, no. 5855, pp. 1430–1433, 2007.

[16] R. Hanson, L. P. Kouwenhoven, J. R. Petta, S. Tarucha, and L. M. K. Vandersypen, "Spins in few-electron quantum dots," *Rev. Mod. Phys.*, vol. 79, p. 1217, 4 2007.

[17] M. D. Shulman, O. E. Dial, S. P. Harvey, H. Bluhm, V. Umansky, and A. Yacoby, "Demonstration of entanglement of electrostatically coupled singlet-triplet qubits," *Science*, vol. 336, no. 6078, p. 202, 2012.

[18] J. Salfi, S. Roddaro, D. Ercolani, L. Sorba, I. Savelyev, M. Blumin, H. E. Ruda, and F. Beltram, "Electronic properties of quantum dot systems realized in semiconductor nanowires," *Semicond. Sci. Technol.*, vol. 25, p. 024 007, 2010.

[19] F. Glas, J.-C. Harmand, and G. Patriarche, "Why does wurtzite form in nanowires of III-V zinc blende semiconductors?" *Phys. Rev. Lett.*, vol. 99, p. 146 101, 14 2007.

[20] S. Lehmann, J. Wallentin, D. Jacobsson, K. Deppert, and K. A. Dick, "A general approach for sharp crystal phase switching in InAs, GaAs, InP, and GaP nanowires using only group V flow," *Nano Lett.*, vol. 13, p. 4099, 2013.

[21] K. D. Petersson, J. R. Petta, H. Lu, and A. C. Gossard, "Quantum coherence in a one-electron semiconductor charge qubit," *Phys. Rev. Lett.*, vol. 105, p. 246 804, 24 2010.

[22] D. Krychowski, "Spin-orbital and spin kondo effects in parallel coupled quantum dots," *Phys. Rev. B*, vol. 93, p. 075 416, 7 2016.

[23] R. S. Deacon, A. Oiwa, J. Sailer, S. Baba, Y. Kanai, K. Shibata, K. Hirakawa, and S. Tarucha, "Cooper pair splitting in parallel quantum dot Josephson junctions," *Nature Communications*, vol. 6, p. 7446, 2015.

[24] S. Baba, J. Sailer, R. S. Deacon, A. Oiwa, K. Shibata, K. Hirakawa, and S. Tarucha, "Superconducting transport in single and parallel double InAs quantum dot Josephson junctions with Nb-based superconducting electrodes," *Applied Physics Letters*, vol. 107, no. 22, p. 222 602, 2015.

[25] B. Ganjipour, M. Leijnse, L. Samuelson, H. Q. Xu, and C. Thelander, "Transport studies of electron-hole and spin-orbit interaction in GaSb/-InAsSb core-shell nanowire quantum dots," *Phys. Rev. B*, vol. 91, p. 161 301, 16 2015.

[26] L. Namazi, M. Nilsson, S. Lehmann, C. Thelander, and K. A. Dick, "Selective GaSb radial growth on crystal phase engineered InAs nanowires," *Nanoscale*, vol. 7, p. 10 472, 2015.

[27] M. Nilsson, L. Namazi, S. Lehmann, M. Leijnse, K. A. Dick, and C. Thelander, "Electron-hole interactions in coupled InAs-GaSb quantum dots based on nanowire crystal phase templates," *Phys. Rev. B*, vol. 94, p. 115 313, 11 2016.

[28] U. Meirav, M. A. Kastner, and S. J. Wind, "Single-electron charging and periodic conductance resonances in GaAs nanostructures," *Phys. Rev. Lett.*, vol. 65, pp. 771–774, 6 1990.

[29] L. P. Kouwenhoven, C. M. Marcus, P. L. Mceuen, S. Tarucha, R. M. Westervelt, and N. S. Wingreen, "Electron transport in quantum dots," *Kluwer Series*, vol. E345, no. Kluwer, 1997.

[30] D. M Zumbühl, "Coherence and spin in GaAs quantum dots," PhD thesis, Harvard University, 2004.

[31] C. Stampfer, J. Güttinger, F. Molitor, D. Graf, T. Ihn, and K. Ensslin, "Tunable coulomb blockade in nanostructured graphene," *Applied Physics Letters*, vol. 92, no. 1, p. 012 102, 2008.

[32] S. Tarucha, D. G. Austing, T. Honda, R. J. van der Hage, and L. P. Kouwenhoven, "Shell filling and spin effects in a few electron quantum dot," *Phys. Rev. Lett.*, vol. 77, pp. 3613–3616, 17 1996.

[33] J. R. Petta, D. G. Salinas, and D. C. Ralph, "Measurements of discrete electronic states in a gold nanoparticle using tunnel junctions formed from self-assembled monolayers," *Applied Physics Letters*, vol. 77, no. 26, pp. 4419–4421, 2000.

[34] M. Jung, T. Machida, K. Hirakawa, S. Komiyama, T. Nakaoka, S. Ishida, and Y. Arakawa, "Shell structures in self-assembled InAs quantum dots probed by lateral electron tunneling structures," *Applied Physics Letters*, vol. 87, no. 20, p. 203 109, 2005.

[35] S. Takahashi, R. S. Deacon, K. Yoshida, A. Oiwa, K. Shibata, K. Hirakawa, Y. Tokura, and S. Tarucha, "Large anisotropy of the spin-orbit interaction in a single inas self-assembled quantum dot," *Phys. Rev. Lett.*, vol. 104, p. 246 801, 24 2010.

[36] M. Fuechsle, J. A. Miwa, S. Mahapatra, H. Ryu, S. Lee, O. Warschkow, L. C. L. Hollenberg, G. Klimeck, and M. Y. Simmons, "A single-atom transistor," *Nature Nanotechnology*, vol. 7, 242–246, 2012.

[37] S. De Franceschi, J. A. van Dam, E. P.A. M. Bakkers, L. F. Feiner, L. Gurevich, and L. P. Kouwenhoven, "Single-electron tunneling in InP nanowires," *Appl. Phys. Lett.*, vol. 83, no. 2, p. 344, 2003.

[38] C. Thelander, T. Mårtensson, M. T. Björk, B. J. Ohlsson, M. W. Larsson, L. R. Wallenberg, and L. Samuelson, "Single-electron transistors in heterostructure nanowires," *Appl. Phys. Lett.*, vol. 83, no. 10, p. 2052, 2003.

[39] C. Fasth, A. Fuhrer, M. T. Björk, and L Samuelson, "Tunable double quantum dots in InAs nanowires defined by local gate electrodes," *Nano Lett.*, vol. 5, no. 7, p. 1487, 2005.

[40] Y. Cui, X. Duan, J. Hu, and C. M. Lieber, "Doping and electrical transport in silicon nanowires," *The Journal of Physical Chemistry B*, vol. 104, no. 22, pp. 5213–5216, 2000.

[41] F. A. Zwanenburg, C. E.W. M. van Rijmenam, Y. Fang, C. M. Lieber, and L. P. Kouwenhoven, "Spin states of the first four holes in a silicon nanowire quantum dot," *Nano Letters*, vol. 9, no. 3, pp. 1071–1079, 2009.

[42] F. Glas, "Critical dimensions for the plastic relaxation of strained axial heterostructures in free-standing nanowires," *Phys. Rev. B*, vol. 74, p. 121 302, 12 2006.

[43] J. Johansson and K. A. Dick, "Recent advances in semiconductor nanowire heterostructures," *CrystEngComm*, vol. 13, p. 7175, 24 2011.

[44] K. A. Dick, C. Thelander, L. Samuelson, and P. Caroff, "Crystal phase engineering in single InAs nanowires," *Nano Lett.*, vol. 10, no. 9, p. 3494, 2010.

[45] M. Nilsson, L. Namazi, S. Lehmann, M. Leijnse, K. A. Dick, and C. Thelander, "Single-electron transport in InAs nanowire quantum dots formed by crystal phase engineering," *Phys. Rev. B*, vol. 93, p. 195 422, 19 2016.

[46] M. Nilsson, I.-J. Chen, S. Lehmann, V. Maulerova, K. A. Dick, and C. Thelander, "Parallel-coupled quantum dots in InAs nanowires," *Nano Letters*, vol. 17, no. 12, pp. 7847–7852, 2017.

[47] P. Caroff, K. A. Dick, J. Johansson, M. E. Messing, K. Deppert, and L. Samuelson, "Controlled polytypic and twin-plane superlattices in III-V nanowires," *Nature Nanotechnology*, vol. 4, p. 50, 2009.

[48] C. Thelander, P. Caroff, S. Plissard, A. W. Dey, and K. A. Dick, "Effects of crystal phase mixing on the electrical properties of InAs nanowires," *Nano Lett.*, vol. 11, no. 6, p. 2424, 2011.

[49] A. R. Ullah, H. J. Joyce, A. M. Burke, J. Wong-Leung, H. H. Tan, C. Jagadish, and A. P. Micolich, "Electronic comparison of InAs wurtzite and zincblende phases using nanowire transistors," *physica status solidi (RRL) – Rapid Research Letters*, vol. 7, no. 10, pp. 911–914, 2013.

[50] K. A. Dick, P. Caroff, J. Bolinsson, M. E. Messing, J. Johansson, K. Deppert, L. R. Wallenberg, and L. Samuelson, "Control of III-V nanowire crystal structure by growth parameter tuning," *Semiconductor Science and Technology*, vol. 25, no. 2, p. 024 009, 2010.

[51] Z. Zanolli, F. Fuchs, J. Furthmüller, U. von Barth, and F. Bechstedt, "Model GW band structure of InAs and GaAs in the wurtzite phase," *Phys. Rev. B*, vol. 75, p. 245 121, 24 2007.

[52] A. Belabbes, C. Panse, J. Furthmüller, and F. Bechstedt, "Electronic bands of III-V semiconductor polytypes and their alignment," *Phys. Rev. B*, vol. 86, p. 075 208, 7 2012.

[53] D. C. Joy, D. E. Newbury, and D. L. Davidson, "Electron channeling patterns in the scanning electron microscope," *J. Appl. Phys.*, vol. 53, no. 8, R81, 1982.

[54] S. Zaefferer and N.-N. Elhami, "Theory and application of electron channelling contrast imaging under controlled diffraction conditions," *Acta Materialia*, vol. 75, p. 20, 2014.

[55] I.-J. Chen, S. Lehmann, M. Nilsson, P. Kivisaari, H. Linke, K. A. Dick, and C. Thelander, "Conduction band offset and polarization effects in InAs nanowire polytype junctions," *Nano Letters*, vol. 17, no. 2, pp. 902–908, 2017.

[56] M. Hjort, S. Lehmann, J. Knutsson, A. A. Zakharov, Y. A. Du, S. Sakong, R. Timm, G. Nylund, E. Lundgren, P. Kratzer, K. A. Dick, and A. Mikkelsen, "Electronic and structural differences between wurtzite and zinc blende InAs nanowire surfaces: Experiment and theory," *ACS Nano*, vol. 8, pp. 12 346–, 2014.

[57] J. V. Knutsson, S. Lehmann, M. Hjort, E. Lundgren, K. A. Dick, R. Timm, and A. Mikkelsen, "Electronic structure changes due to crystal phase switching at the atomic scale limit," *ACS Nano*, vol. 11, no. 10, pp. 10 519–10 528, 2017.

[58] K. A. Dick, "A review of nanowire growth promoted by alloys and non-alloying elements with emphasis on Au-assisted III-V nanowires," *Progress in Crystal Growth and Characterization of Materials*, vol. 54, p. 138, 2008.

[59] J. Johansson, K. A. Dick, P. Caroff, M. E. Messing, J. Bolinsson, K. Deppert, and L. Samuelson, "Diameter dependence of the wurtzite-zinc blende transition in InAs nanowires," *The Journal of Physical Chemistry C*, vol. 114, no. 9, pp. 3837–3842, 2010.

[60] M. D. Schroer and J. R. Petta, "Correlating the nanostructure and electronic properties of InAs nanowires," *Nano Lett.*, vol. 10, no. 5, p. 1618, 2010.

[61] P. Caroff, J. Bolinsson, and J. Johansson, "Crystal phases in III-V nanowires: From random toward engineered polytypism," *IEEE Journal of Selected Topics in Quantum Electronics*, vol. 17, no. 4, pp. 829–846, 2011.

[62] R. E. Algra, M. A. Verheijen, M. T. Borgström, L.-F. Feiner, G. Immink, W. J. P. van Enckevort, E. Vlieg, and E. P.A. M. Bakkers, "Twinning superlattices in indium phosphide nanowires," *Nature*, vol. 456, p. 369, 2008.

[63] K. Flöhr, M. Liebmann, K. Sladek, H. Y. Günel, R. Frielinghaus, F. Haas, C. Meyer, H. Hardtdegen, T. Schäpers, D. Grützmacher, and M. Morgenstern, "Manipulating InAs nanowires with submicrometer precision," *Review of Scientific Instruments*, vol. 82, no. 11, p. 113 705, 2011.

[64] C. Thelander, "Semi-atomatic electrods - LabVIEW program," 2018. [Online]. Available: `http://www.nano.lu.se/tibet/template/personal%2CIndex.vm?pageid=253068&siteid=1040`.

[65] T. S. Jespersen, M. L. Polianski, C. B. Sörensen, K. Flensberg, and J. Nygård, "Mesoscopic conductance fluctuations in InAs nanowire-based SNS junctions," *New Journal of Physics*, vol. 11, no. 11, p. 113 025, 2009.

[66] S. Abay, D. Persson, H. Nilsson, F. Wu, H. Q. Xu, M. Fogelström, V. Shumeiko, and P. Delsing, "Charge transport in InAs nanowire Josephson junctions," *Phys. Rev. B*, vol. 89, p. 214 508, 21 2014.

[67] K. Weis, S. Wirths, A. Winden, K. Sladek, H. Hardtdegen, H. Lüth, D. Grützmacher, and T. Schäpers, "Quantum dots in InAs nanowires induced by surface potential fluctuations," *Nanotechnology*, vol. 25, no. 13, p. 135 203, 2014.

[68] C. W. J. Beenakker, "Theory of Coulomb-blockade oscillations in the conductance of a quantum dot," *Phys. Rev. B*, vol. 44, pp. 1646–1656, 4 1991.

[69] A. Fuhrer, "Phase coherence , orbital and states in quantum rings spin," PhD thesis, Swiss federal institute of technology Zürich, 2003.

[70] D. R. Khanal and J. Wu, "Gate coupling and charge distribution in nanowire field effect transistors," *Nano Lett.*, vol. 7, no. 9, p. 2778, 2007.

[71] S. De Franceschi, S. Sasaki, J. M. Elzerman, W. G. van der Wiel, S. Tarucha, and L. P. Kouwenhoven, "Electron cotunneling in a semiconductor quantum dot," *Phys. Rev. Lett.*, vol. 86, pp. 878–881, 5 2001.

[72] D. M. Zumbühl, C. M. Marcus, M. P. Hanson, and A. C. Gossard, "Cotunneling spectroscopy in few-electron quantum dots," *Phys. Rev. Lett.*, vol. 93, p. 256 801, 25 2004.

[73] R. Schleser, T. Ihn, E. Ruh, K. Ensslin, M. Tews, D. Pfannkuche, D. C. Driscoll, and A. C. Gossard, "Cotunneling-mediated transport through excited states in the coulomb-blockade regime," *Phys. Rev. Lett.*, vol. 94, p. 206 805, 20 2005.

[74] J. Aghassi, M. H. Hettler, and G. Schön, "Cotunneling assisted sequential tunneling in multilevel quantum dots," *Applied Physics Letters*, vol. 92, no. 20, p. 202 101, 2008.

[75] T. Inoshita, "Kondo effect in quantum dots," *Science*, vol. 281, no. 5376, pp. 526–527, 1998.

[76] D. Goldhaber-Gordon, H. Shtrikman, D. Mahalu, D. Abusch-Magder, U. Meirav, and M. A. Kastner, "Kondo effect in a single-electron transistor," *Nature*, vol. 391, pages 156–159, 1998.

[77] M. Pustilnik and L. Glazman, "Kondo effect in quantum dots," *Journal of Physics: Condensed Matter*, vol. 16, no. 16, R513, 2004.

[78] T. S. Jespersen, M. Aagesen, C. Sørensen, P. E. Lindelof, and J. Nygård, "Kondo physics in tunable semiconductor nanowire quantum dots," *Phys. Rev. B*, vol. 74, p. 233 304, 23 2006.

[79] T. Fujisawa, G. Shinkai, and T. Hayashi, "Zeeman splitting in single-electron transport through a few-electron quantum dot," *Phys. Rev. B*, vol. 76, p. 041 302, 4 2007.

[80] H. Kosaka, A. A. Kiselev, F. A. Baron, K. W. Kim, and E. Yablonovitch, "Electron g factor engineering in IlI-V semiconductors for quantum communications," *Electronics Letters*, vol. 37, no. 7, pp. 464–465, 2001.

[81] M. Reine, R. L. Aggarwal, and B. Lax, "Stress-modulated magnetoreflectivity of gallium antimonide and gallium arsenide," *Phys. Rev. B*, vol. 5, pp. 3033–3049, 8 1972.

[82] L. M. Roth, B. Lax, and S. Zwerdling, "Theory of optical magneto-absorption effects in semiconductors," *Phys. Rev.*, vol. 114, pp. 90–104, 1 1959.

[83] A. Srinivasan, D. S. Miserev, K. L. Hudson, O. Klochan, K. Muraki, Y. Hirayama, D. Reuter, A. D. Wieck, O. P. Sushkov, and A. R. Hamilton, "Detection and control of spin-orbit interactions in a GaAs hole quantum point contact," *Phys. Rev. Lett.*, vol. 118, p. 146 801, 14 2017.

[84] T. S. Jespersen, P. Krogstrup, A. M. Lunde, R. Tanta, T. Kanne, E. Johnson, and J. Nygård, "Crystal orientation dependence of the spin-orbit coupling in InAs nanowires," *Phys. Rev. B*, vol. 97, p. 041 303, 4 2018.

[85] T. P. Smith III and F. F. Fang, "g factor of electrons in an InAs quantum well," *Phys. Rev. B*, vol. 35, pp. 7729–7731, 14 1987.

[86] A. A. Kiselev, E. L. Ivchenko, and U. Rössler, "Electron g factor in one- and zero-dimensional semiconductor nanostructures," *Phys. Rev. B*, vol. 58, pp. 16 353–16 359, 24 1998.

[87] J. R. Petta and D. C. Ralph, "Studies of spin-orbit scattering in noble-metal nanoparticles using energy-level tunneling spectroscopy," *Phys. Rev. Lett.*, vol. 87, p. 266 801, 26 2001.

[88] M. T. Björk, A. Fuhrer, A. E. Hansen, M. W. Larsson, L. E. Fröberg, and L. Samuelson, "Tunable effective g factor in InAs nanowire quantum dots," *Phys. Rev. B*, vol. 72, p. 201 307, 20 2005.

[89] C. E. Pryor and M. E. Flatté, "Landé g factors and orbital momentum quenching in semiconductor quantum dots," *Phys. Rev. Lett.*, vol. 96, p. 026 804, 2 2006.

[90] S. Csonka, L. Hofstetter, F. Freitag, S. Oberholzer, C. Schönenberger, T. S. Jespersen, M. Aagesen, and J. Nygård, "Giant fluctuations and gate control of the g-factor in InAs nanowire quantum dots," *Nano Letters*, vol. 8, no. 11, pp. 3932–3935, 2008.

[91] H. A. Nilsson, P. Caroff, C. Thelander, M. Larsson, J. B. Wagner, L.-E. Wernersson, L. Samuelson, and H. Q. Xu, "Giant, level-dependent g factors in InSb nanowire quantum dots," *Nano Letters*, vol. 9, no. 9, pp. 3151–3156, 2009.

[92] M. D. Schroer, K. D. Petersson, M. Jung, and J. R. Petta, "Field tuning the g factor in InAs nanowire double quantum dots," *Phys. Rev. Lett.*, vol. 107, p. 176 811, 17 2011.

[93] G. W. Winkler, D. Varjas, R. Skolasinski, A. A. Soluyanov, M. Troyer, and M. Wimmer, "Orbital contributions to the electron g factor in semiconductor nanowires," *Phys. Rev. Lett.*, vol. 119, p. 037 701, 3 2017.

[94] S. Takahashi, R. S. Deacon, A. Oiwa, K. Shibata, K. Hirakawa, and S. Tarucha, "Electrically tunable three-dimensional g-factor anisotropy in single InAs self-assembled quantum dots," *Phys. Rev. B*, vol. 87, p. 161 302, 16 2013.

[95] R. Winkler, *Spin–Orbit Coupling Effects in Two-Dimensional Electron and Hole Systems*. Springer Berlin Heidelberg, 2003.

[96] J. R. Petta and D. C. Ralph, "Measurements of strongly anisotropic g factors for spins in single quantum states," *Phys. Rev. Lett.*, vol. 89, p. 156 802, 15 2002.

[97] T. P. M. Alegre, F. G. G. Hernández, A. L. C. Pereira, and G. Medeiros-Ribeiro, "Landé g tensor in semiconductor nanostructures," *Phys. Rev. Lett.*, vol. 97, p. 236 402, 23 2006.

[98] Y. Kanai, R. S. Deacon, S. Takahashi, A. Oiwa, K. Yoshida, K. Shibata, K. Hirakawa, Y. Tokura, and S. Tarucha, "Electrically tuned spin-orbit interaction in an InAs self-assembled quantum dot," *Nature Nanotechnology*, vol. 6, pp. 511–516, 2011.

[99] S. Nadj-Perge, V. S. Pribiag, J. W. G. van den Berg, K. Zuo, S. R. Plissard, E. P.A. M. Bakkers, S. M. Frolov, and L. P. Kouwenhoven, "Spectroscopy of spin-orbit quantum bits in indium antimonide nanowires," *Phys. Rev. Lett.*, vol. 108, p. 166 801, 16 2012.

[100] P. W. Brouwer, X. Waintal, and B. I. Halperin, "Fluctuating spin g-tensor in small metal grains," *Phys. Rev. Lett.*, vol. 85, pp. 369–372, 2 2000.

[101] J. R. Petta, A. C. Johnson, J. M. Taylor, E. A. Laird, A. Yacoby, M. D. Lukin, C. M. Marcus, M. P. Hanson, and A. C. Gossard, "Coherent manipulation of coupled electron spins in semiconductor quantum dots," *Science*, vol. 309, no. 5744, p. 2180, 2005.

[102] K. Goß, S. Smerat, M. Leijnse, M. R. Wegewijs, C. M. Schneider, and C. Meyer, "Spin-dependent electronic hybridization in a rope of carbon nanotubes," *Phys. Rev. B*, vol. 83, p. 201 403, 20 2011.

[103] K. Goß, M. Leijnse, S. Smerat, M. R. Wegewijs, C. M. Schneider, and C. Meyer, "Parallel carbon nanotube quantum dots and their interactions," *Phys. Rev. B*, vol. 87, p. 035 424, 3 2013.

[104] M. Jung, J. Schindele, S. Nau, M. Weiss, A. Baumgartner, and C. Schönenberger, "Ultraclean single, double, and triple carbon nanotube quantum dots with recessed re bottom gates," *Nano Letters*, vol. 13, no. 9, pp. 4522–4526, 2013.

[105] G. Abulizi, A. Baumgartner, and C. Schönenberger, "Full characterization of a carbon nanotube parallel double quantum dot," *physica status solidi (b)*, vol. 253, no. 12, pp. 2428–2432, 2016.

[106] W. G. van der Wiel, S. De Franceschi, J. M. Elzerman, T. Fujisawa, S. Tarucha, and L. P. Kouwenhoven, "Electron transport through double quantum dots," *Rev. Mod. Phys.*, vol. 75, pp. 1–22, 1 2002.

[107] G. Fábián, P. Makk, M. H. Madsen, J. Nygård, C. Schönenberger, and A. Baumgartner, "Magnetoresistance engineering and singlet/triplet switching in InAs nanowire quantum dots with ferromagnetic sidegates," *Phys. Rev. B*, vol. 94, p. 195 415, 19 2016.

[108] T. Hatano, M. Stopa, and S. Tarucha, "Single-electron delocalization in hybrid vertical-lateral double quantum dots," *Science*, vol. 309, no. 5732, pp. 268–271, 2005.

[109] T. Hatano, S. Amaha, T. Kubo, Y. Tokura, Y. Nishi, Y. Hirayama, and S. Tarucha, "Manipulation of exchange coupling energy in a few-electron double quantum dot," *Phys. Rev. B*, vol. 77, p. 241 301, 24 2008.

[110] T. Hatano, T. Kubo, Y. Tokura, S. Amaha, S. Teraoka, and S. Tarucha, "Aharonov-Bohm oscillations changed by indirect interdot tunneling via electrodes in parallel-coupled vertical double quantum dots," *Phys. Rev. Lett.*, vol. 106, p. 076 801, 7 2011.

[111] T. Hatano, Y. Tokura, S. Amaha, T. Kubo, S. Teraoka, and S. Tarucha, "Excitation spectroscopy of few-electron states in artificial diatomic molecules," *Phys. Rev. B*, vol. 87, p. 241 414, 24 2013.

[112] S. Roddaro, A. Pescaglini, D. Ercolani, L. Sorba, and F. Beltram, "Manipulation of electron orbitals in hard-wall InAs/InP nanowire quantum dots," *Nano Letters*, vol. 11, no. 4, pp. 1695–1699, 2011.

[113] L. Romeo, S. Roddaro, A. Pitanti, D. Ercolani, L. Sorba, and F. Beltram, "Electrostatic spin control in InAs/InP nanowire quantum dots," *Nano Lett.*, vol. 12, no. 9, p. 4490, 2012.

[114] Y. Tokura, T. Obata, T. Hatano, and S. Tarucha, *Electron-Spin Manipulation in Quantum Dot Systems*, M. Fanciulli, Ed. Berlin, Heidelberg: Springer Berlin Heidelberg, 2009, pp. 15–34.

[115] S. Tarucha, D. G. Austing, Y. Tokura, W. G. van der Wiel, and L. P. Kouwenhoven, "Direct Coulomb and exchange interaction in artificial atoms," *Phys. Rev. Lett.*, vol. 84, pp. 2485–2488, 11 2000.

[116] D. Stepanenko, M. Rudner, B. I. Halperin, and D. Loss, "Singlet-triplet splitting in double quantum dots due to spin-orbit and hyperfine interactions," *Phys. Rev. B*, vol. 85, p. 075 416, 7 2012.

[117] M. Noguchi, K. Hirakawa, and T. Ikoma, "Intrinsic electron accumulation layers on reconstructed clean InAs(100) surfaces," *Phys. Rev. Lett.*, vol. 66, pp. 2243–2246, 17 1991.

[118] J. R. Weber, A. Janotti, and C. G. V. de Walle, "Intrinsic and extrinsic causes of electron accumulation layers on InAs surfaces," *Applied Physics Letters*, vol. 97, no. 19, p. 192 106, 2010.

[119] D. C. Tsui, "Observation of surface bound state and two-dimensional energy band by electron tunneling," *Phys. Rev. Lett.*, vol. 24, p. 303, 7 1970.

[120] H. U. Baier, L Koenders, and W Mönch, "Oxidation of cleaved InAs (110) surfaces at room temperature: surface band-bending and ionization energy," *Solide State Commun.*, vol. 58, no. 5, p. 327, 1986.

[121] Y. Chen, J. C. Hermanson, and G. J. Lapeyre, "Coupled plasmon and phonon in the accumulation layer of InAs(110) cleaved surfaces," *Phys. Rev. B*, vol. 39, pp. 12 682–12 687, 17 1989.

[122] L. F. J. Piper, T. D. Veal, M. J. Lowe, and C. F. McConville, "Electron depletion at inas free surfaces: Doping-induced acceptorlike gap states," *Phys. Rev. B*, vol. 73, p. 195 321, 19 2006.

[123] E. Halpern, G. Elias, A. V. Kretinin, H. Shtrikman, and Y. Rosenwaks, "Direct measurement of surface states density and energy distribution in individual InAs nanowires," *Appl. Phys. Lett.*, vol. 100, no. 26, 2012.

[124] A. C. Ford, J. C. Ho, Y.-L. Chueh, Y.-C. Tseng, Z. Fan, J. Guo, J. Bokor, and A. Javey, "Diameter-dependent electron mobility of InAs nanowires," *Nano Letters*, vol. 9, no. 1, pp. 360–365, 2009.

[125] D. Lynall, S. V. Nair, D. Gutstein, A. Shik, I. G. Savelyev, M. Blumin, and H. E. Ruda, "Surface state dynamics dictating transport in InAs nanowires," *Nano Letters*, vol. 18, no. 2, pp. 1387–1395, 2018.

[126] A. V. Khaetskii and Y. V. Nazarov, "Spin relaxation in semiconductor quantum dots," *Phys. Rev. B*, vol. 61, pp. 12 639–12 642, 19 2000.

[127] A. V. Khaetskii and Y. V. Nazarov, "Spin-flip transitions between zeeman sublevels in semiconductor quantum dots," *Phys. Rev. B*, vol. 64, p. 125 316, 12 2001.

[128] F. H. L. Koppens, J. A. Folk, J. M. Elzerman, R. Hanson, L. H. W. van Beveren, I. T. Vink, H. P. Tranitz, W. Wegscheider, L. P. Kouwenhoven, and L. M. K. Vandersypen, "Control and detection of singlet-triplet mixing in a random nuclear field," *Science*, vol. 309, no. 5739, pp. 1346–1350, 2005.

[129] J. Danon and Y. V. Nazarov, "Pauli spin blockade in the presence of strong spin-orbit coupling," *Phys. Rev. B*, vol. 80, p. 041 301, 4 2009.

[130] S. Nadj-Perge, S. M. Frolov, E. P.A. M. Bakkers, and L. P. Kouwenhoven, "Spin–orbit qubit in a semiconductor nanowire," *Nature*, vol. 468, p. 1084, 2010.

[131] L. L. Chang and L. Esaki, "Electronic properties of InAs-GaSb superlattices," *Surface Science*, vol. 98, p. 70, 1980.

[132] H. Kromer, "The 6.1 Å family (InAs, GaSb, AlSb) and its heterostructures: a selective review," *Physica E*, vol. 20, 2004.

[133] T. O. Stadelmann, "Antidot superlattices in InAs–GaSb double heterostructures: Transport studies," PhD thesis, University College, Oxford, 2006.

[134] M. Altarelli, "Electronic structure and semiconductor-semimetal transition in InAs-GaSb superlattices," *Phys. Rev. B*, vol. 28, p. 842, 2 1983.

[135] M. J. Yang, C. H. Yang, B. R. Bennett, and B. V. Shanabrook, "Evidence of a hybridization gap in "semimetallic" InAs/GaSb systems," *Phys. Rev. Lett.*, vol. 78, p. 4613, 24 1997.

[136] L. J. Cooper, N. K. Patel, V. Drouot, E. H. Linfield, D. A. Ritchie, and M. Pepper, "Resistance resonance induced by electron-hole hybridization in a strongly coupled InAs/GaSb/AlSb heterostructure," *Phys. Rev. B*, vol. 57, p. 11 915, 19 1998.

[137] I. Knez and R.-R. Du, "Quantum spin hall effect in inverted InAs/GaSb quantum wells," *Frontiers of Physics*, vol. 7, no. 2, p. 200, 2011.

[138] V. S. Pribiag, A. J. A. Beukman, F. Qu, M. C. Cassidy, C. Charpentier, W. Wegscheider, and L. P. Kouwenhoven, "Edge-mode superconductivity in a two-dimensional topological insulator," *Nature Nanotechnology*, vol. 10, 593—597, 2015.

[139] C. Liu, T. L. Hughes, X.-L. Qi, K. Wang, and S.-C. Zhang, "Quantum spin hall effect in inverted type-II semiconductors," *Phys. Rev. Lett.*, vol. 100, p. 236 601, 23 2008.

[140] I. Knez, R.-R. Du, and G. Sullivan, "Evidence for helical edge modes in inverted InAs/GaSb quantum wells," *Phys. Rev. Lett.*, vol. 107, p. 136 603, 13 2011.

[141] F. Qu, A. J. A. Beukman, S. Nadj-Perge, M. Wimmer, B.-M. Nguyen, W. Yi, J. Thorp, M. Sokolich, A. A. Kiselev, M. J. Manfra, C. M. Marcus, and L. P. Kouwenhoven, "Electric and magnetic tuning between the trivial and topological phases in InAs/GaSb double quantum wells," *Phys. Rev. Lett.*, vol. 115, p. 036 803, 3 2015.

[142] K. Suzuki, Y. Harada, K. Onomitsu, and K. Muraki, "Gate-controlled semimetal-topological insulator transition in an InAs/GaSb heterostructure," *Phys. Rev. B*, vol. 91, p. 245 309, 24 2015.

[143] S. Mueller, A. N. Pal, M. Karalic, T. Tschirky, C. Charpentier, W. Wegscheider, K. Ensslin, and T. Ihn, "Nonlocal transport via edge states in InAs/GaSb coupled quantum wells," *Phys. Rev. B*, vol. 92, p. 081 303, 8 2015.

[144] F. Nichele, H. J. Suominen, M. Kjaergaard, C. M. Marcus, E. Sajadi, J. A. Folk, F. Qu, A. J. A. Beukman, F. K. de Vries, J. van Veen, S. Nadj-Perge, L. P. Kouwenhoven, B.-M. Nguyen, A. A. Kiselev, W. Yi, M. Sokolich, M. J. Manfra, E. M. Spanton, and K. A. Moler, "Edge transport in the trivial phase of InAs/GaSb," *New Journal of Physics*, vol. 18, no. 8, p. 083 005, 2016.

[145] S. Mueller, C. Mittag, T. Tschirky, C. Charpentier, W. Wegscheider, K. Ensslin, and T. Ihn, "Edge transport in InAs and InAs/GaSb quantum wells," *Phys. Rev. B*, vol. 96, p. 075 406, 7 2017.

[146] M.-E. Pistol and C. E. Pryor, "Band structure of core-shell semiconductor nanowires," *Phys. Rev. B*, vol. 78, p. 115 319, 11 2008.

[147] V. V. R. Kishore, B. Partoens, and F. M. Peeters, "Electronic structure of InAs/GaSb core-shell nanowires," *Phys. Rev. B*, vol. 86, p. 165 439, 16 2012.

[148] N. Luo, G.-Y. Huang, G. Liao, L.-H. Ye, and H. Q. Xu, "Band-inverted gaps in InAs/GaSb and GaSb/InAs core-shell nanowires," *Scientific Reports*, vol. 6, p. 38 698, 2016.

[149] F. Viñas, H. Q. Xu, and M. Leijnse, "Extracting band structure characteristics of GaSb/InAs core-shell nanowires from thermoelectric properties," *Phys. Rev. B*, vol. 95, p. 115 420, 11 2017.

[150] M. Z. Hasan and C. L. Kane, "Colloquium: Topological insulators," *Rev. Mod. Phys.*, vol. 82, pp. 3045–3067, 4 2010.

[151] F. Viñas, "Electronic structure, transport properties and topological features of GaSb/InAs core-shell nanowires," Licentiate thesis, Lund University, 2017.

[152] M. Borg, "Antimonide heterostructure nanowires - growth, physics and devices," PhD thesis, Lund University, 2012.

[153] B. Ganjipour, M. Ek, B. M. Borg, K. A. Dick, M.-E. Pistol, L.-E. Wernersson, and C. Thelander, "Carrier control and transport modulation in GaSb/InAsSb core/shell nanowires," *Appl. Phys. Lett.*, vol. 101, p. 103 501, 2012.

[154] T. Rieger, D. Grützmacher, and M. I. Lepsa, "InAs nanowires with $Al_xGa_{1-x}Sb$ shells for band alignment engineering," *Journal of Crystal Growth*, vol. 425, p. 80, 2015.

[155] B. Ganjipour, S. Sepehri, A. W. Dey, O. Tizno, M. B. Borg, K. A. Dick, L. Samuelson, L.-E. Wernersson, and C. Thelander, "Electrical properties of GaSb/InAsSb core/shell nanowires," *Nanotechnology*, vol. 25, no. 42, p. 425 201, 2014.

[156] J. G. Gluschke, M. Leijnse, B. Ganjipour, K. A. Dick, H. Linke, and C. Thelander, "Characterization of ambipolar GaSb/InAs core-shell nanowires by thermovoltage measurements," *ACS Nano*, vol. 9, no. 7, pp. 7033–7040, 2015.

[157] A. W. Dey, B. M. Borg, B. Ganjipour, M. Ek, K. A. Dick, E. Lind, C. Thelander, and L. E. Wernersson, "High-current GaSb/InAs(Sb) nanowire tunnel field-effect transistors," *IEEE Electron Device Letters*, vol. 34, no. 2, pp. 211–213, 2013.

[158] M. Rocci, F. Rossella, U. P. Gomes, V. Zannier, F. Rossi, D. Ercolani, L. Sorba, F. Beltram, and S. Roddaro, "Tunable esaki effect in catalyst-free InAs/GaSb core-shell nanowires," *Nano Letters*, vol. 16, no. 12, pp. 7950–7955, 2016.

[159] L. He, G. Bester, and A. Zunger, "Prediction of an excitonic ground state in InAs/InSb quantum dots," *Phys. Rev. Lett.*, vol. 94, p. 016 801, 1 2005.

[160] P. S. Dutta, H. L. Bhat, and V. Kumar, "The physics and technology of gallium antimonide: An emerging optoelectronic material," *Journal of Applied Physics*, vol. 81, no. 9, pp. 5821–5870, 1997.

[161] K. Takei, M. Madsen, H. Fang, R. Kapadia, S. Chuang, H. S. Kim, C.-H. Liu, E. Plis, J. Nah, S. Krishna, Y.-L. Chueh, J. Guo, and A. Javey, "Nanoscale InGaSb heterostructure membranes on Si substrates for high hole mobility transistors," *Nano Letters*, vol. 12, no. 4, pp. 2060–2066, 2012.

Acknowledgments

The completion of this thesis would not have been possible without a large number of people that have contributed with valuable assistance and support during the past 5 years. I would now like to take the opportunity to show my immense gratitude.

First, I want thank my main supervisor Claes Thelander for being a versatile, hands-on experimentalist full of new ideas. I would like to thank you for your support, and for teaching me many valuable fabrication techniques and for the neverending development of the LabView programs for designing contacts and controlling measurement setups in the labs. Thank you for giving me the opportunity to pursue this PhD, a journey lined with a number of challenges but also moments of success. To Martin Leijnse, my co-supervisor, thank you for fruitful collaborations and discussions helping my expand my theoretical understanding, and for helpful comments and encouragement in general. To Heiner Linke, my co-supervisor and course coordinator for the quantum mechanics course I had the pleasure to teach, thank you for general guidance and for providing a highly appreciated and fun course to teach.

My deepest gratitude to Kimberly Dick Thelander and her impressively skilled nanowire-growth team, without whom none of this work would have been possible. I would especially like to thank Luna Namazi for growing such fantastic nanowires, and for being an awesome conference/travel companion and friend. My gratitude also goes to Sebastian Lehmann for providing *in principle* on-demand nanowire designs, for being an endless source of knowledge when it comes to nanowire growth, crystal phase theory and imaging-related matters, and for always being keen on interesting discussions and answering my questions. Thank you for your encouragement and for a seamless collaboration.

Thank you Adam Burke for teaching me the dilution fridge system and for all the support with fridge-related matters as well as general encouragement over the years. And perhaps most importantly, for always contributing to an open and positive atmosphere; I cannot thank you enough for that. I am very grateful to Michael Hell, for all the interesting and educative discussions and to Heidi Potts for all the valuable comments on the thesis.

I would like to thank Florinda Viñas Boström and I-Ju Chen for great collaborations and exciting discussions.

My gratitude goes out to all the administrative and technical support staff for keeping FTF running smoothy; Dan Hessman, Heiner Linke, Anneli Lövgren, Anders Gustavsson, Line Lundfald, Abdul-Rehman Hakim, Bengt Meuller and many more. In addition, thank you to the NanoLab staff members for keeping the lab in mint condition: Maria Huffman, Ivan Maximov, Mariusz Graczyk, Sara Ataran, George Rydnemalm, Håkan Lapovski, Dmitry Suyatin, Peter Blomqvist and David Fitzgerald. And especially, thanks to Anders Kvennefors for the endless support, particularly in the EBL-defined array project. Thank you Leif Magnusson for all the friendly chats at Kryolab and managing swift He refills, often with short notice!

Thanks to my office mates, Robert and David, for contributing to a friendly atmosphere and thanks for all off-topic physics discussions.

I am very grateful for being a part of NanoLund for the past few years. Aside from the excellent scientific environment, NanoLund provide a unique platform enabling interaction with people from many different backgrounds. I would like to say thank you to the senior staff members who crossed my path the last 5 years: Maria Messing, Carina Fasth, Mats-Erik Pistol, Christelle Prinz, Ville Maisi. I am extremely thankful for all my PhD-colleagues and friends at FTF, who have brightened my workdays: Regina, Kushagr, Neimantas, Gaute, Laura, Chunlin, Enrique, Anders, Mercy, Steven, Olof, Rong, Zhen, Frida, Damiano, Oskar, Artis, Martin, Sara, Calle, Marcus, Irene, Vilgaile... the list goes on! I also extend my thanks to the friends I made in the cleanroom for all the friendly chats: Cezar, Anil, Johannes, Elvedin.

Thanks to all my former colleagues and friends at FTF, you are not forgotten: Henrik, Cassandra, Sofia, Vishal, David, Bahram, Magnus, Pyry among many. I specially want to thank Gustav for *always* lending a helping hand, and guiding me through the beginning of PhD-life.

I also highly appreciated the number of conferences I have had the op-

portunity to attend during the past 5 years; thanks to all my fantastic travel companions and new-made friends.

Finally, I would like to show my love to all my non-physicist friends and my family, for challenge me to explain what my work is actually about, for the never ending encouragement, and for helping me keeping one foot in the real world.

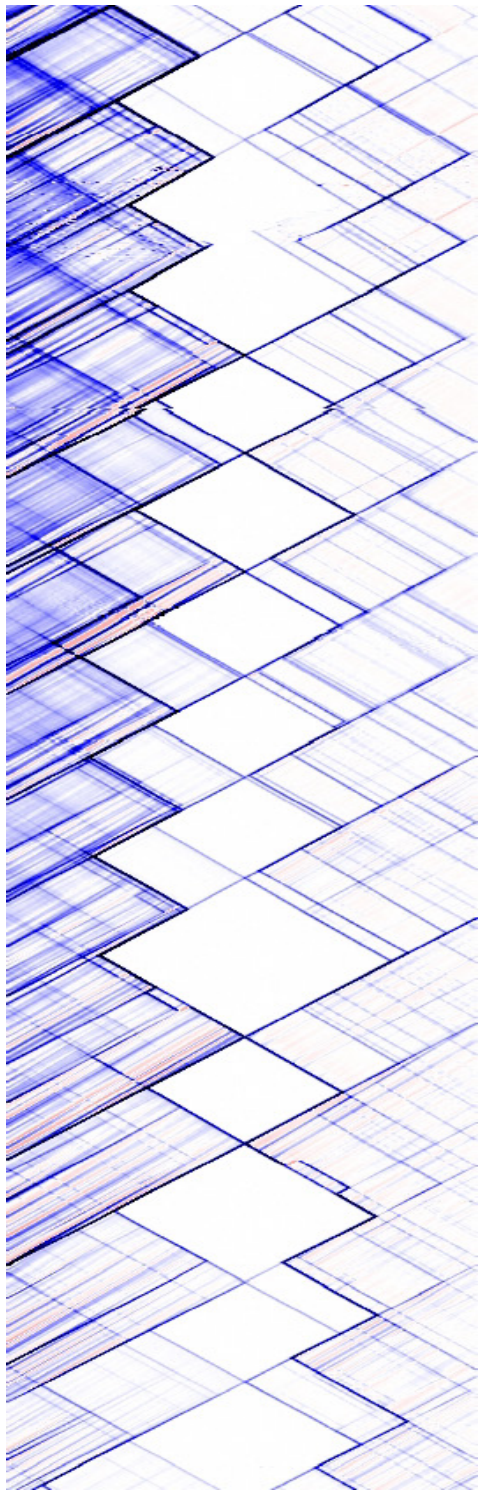

Printed by Media-Tryck, Lund 2018 NORDIC SWAN ECOLABEL 3041 0903

LUND UNIVERSITY
Division of Solid State Physics
Department of Physics
Faculty of Engineering

ISBN 978-91-7753-701-4